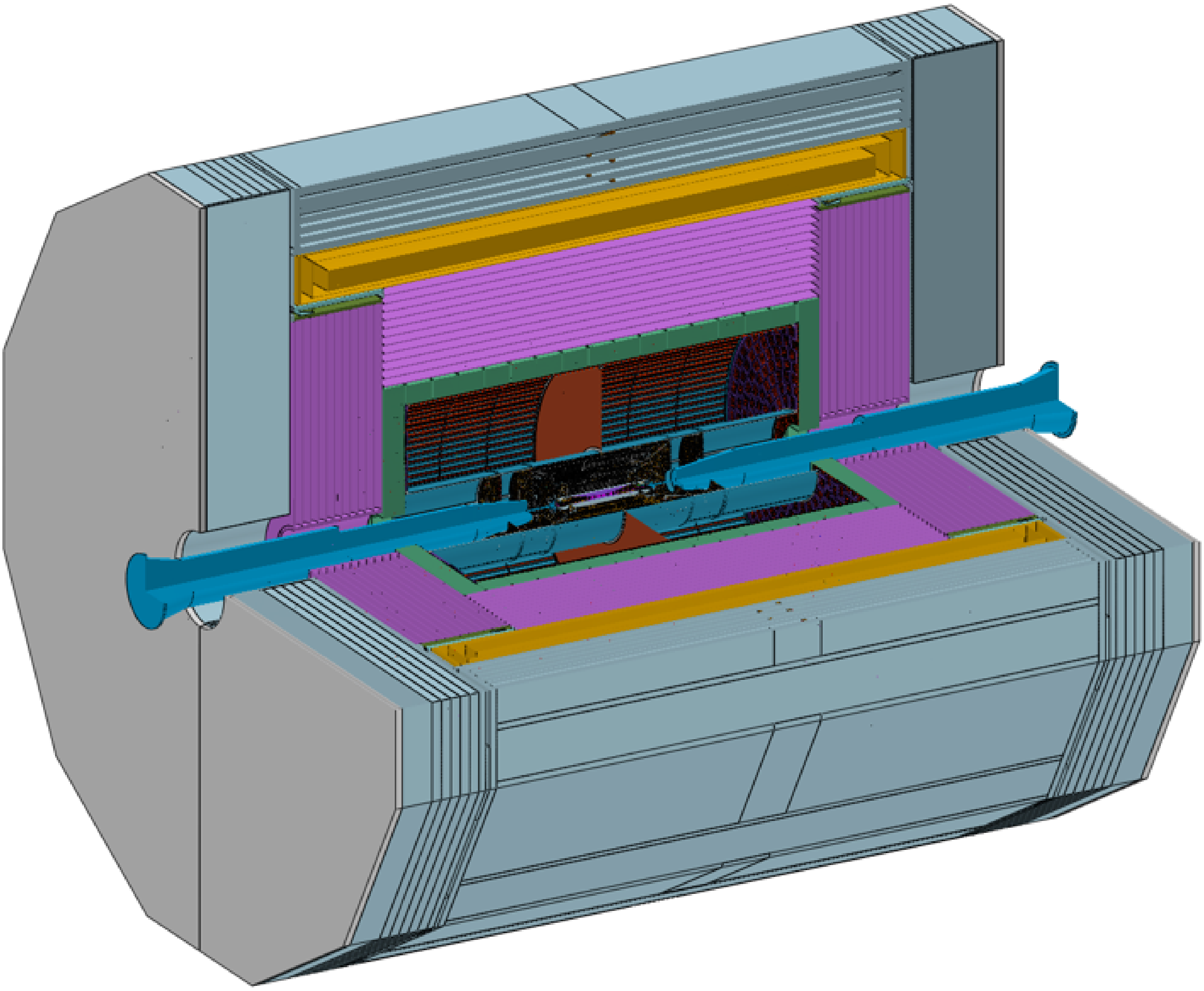

Technical Design Report of the CEPC Reference Detector

Technical Design Report of the CEPC Reference Detector

Author: the CEPC study group

Institute:

Date: June 9, 2025

Version: 0.1 build: 2025-05-12 22:05:13+08:00

Bio: Information

Contents

Chapter 1 Hadron calorimeter **1**

1.1 Physics Requirements of HCAL . . . 1

1.2 Technical Survey of HCAL . . . 2

1.2.1 Semi-Digital HCAL Based on RPC (SDHCAL) . . . 3

1.2.2 Analogue HCAL based on plastic scintillator (PS-HCAL) . . . 6

1.2.3 Glass scintillator based calorimeter . . . 10

1.3 Design of the GS-HCAL . . . 11

1.3.1 Key parameters of the glass scintillator . . . 11

1.3.1.1 Glass density . . . 11

1.3.1.2 Light yield and threshold . . . 11

1.3.1.3 Light attenuation . . . 13

1.3.1.4 Quenching effects . . . 13

1.3.1.5 Decay time . . . 14

1.3.2 Design optimization of HCAL . . . 14

1.3.2.1 Thickness of a glass cell . . . 14

1.3.2.2 Transverse size . . . 15

1.3.2.3 Thickness and total interaction length . . . 16

1.3.2.4 Dynamic range . . . 16

1.3.3 Overall design . . . 17

1.4 Glass Scintillator . . . 20

1.4.1 Scintillator materials (GS) . . . 20

1.4.2 Performance of $5\times5\times5$ mm^3 sample . . . 21

1.4.3 Performance of 40mm$\times$40mm$\times$10mm sample . . . 23

1.4.4 Characteristic study for GFO glass scintillator . . . 23

1.4.4.1 Light attenuation length . . . 23

1.4.4.2 Radiation Resistance . . . 25

1.4.4.3 MIP response of the GFO . . . 28

1.5 SiPMs for HCAL . . . 30

1.5.1 SiPM selection . . . 30

1.5.2 Dark counting rate and threshold . . . 30

1.5.3 Study of GS-HCAL Cell . . . 32

1.5.3.1 Optical simulation for GS cell . . . 32

1.5.3.2 Front-end electronics for SiPM test . . . 34

1.5.3.3 GS cell test . . . 36

1.6 Electronics & DAQ . . . 37

1.6.1 Electronics for SiPM . . . 37

1.6.2 Readout Electronics . . . 37

1.7 Mechanics . . . 39

1.7.1 Barrel part . . . 39

1.7.1.1 Overview and requirements of barrel HCAL . . . 39

1.7.1.2 Structure design . . . 40

1.7.1.3 Finite element analysis result . . . 42

1.7.1.4 Cables routing scheme . . . 46

1.7.2 Mechanics of the endcaps . . . 47

1.7.2.1 Overall structure . . . 48

1.7.2.2 Active layer structure . . . 48
1.7.3 Cooling system . . . 49
1.7.3.1 Cooling scheme . . . 49
1.7.3.2 FEA simulation . . . 51
1.7.3.3 Cooling structure of Barrel . . . 53
1.7.3.4 Cooling structure of endcap . . . 53
1.8 Calibration . . . 53
1.8.1 Calibration using physics processes . . . 53
1.8.2 Hardware calibration . . . 54
1.8.2.1 System design . . . 54
1.8.2.2 Electronics and control . . . 55
1.9 Performance . . . 55
1.9.1 GS-AHCAL layout and performance goals . . . 55
1.9.2 Global performance . . . 56
1.9.2.1 Energy linearity and resolution . . . 56
1.9.2.2 BMR result of HCAL . . . 60
1.9.3 Beam background simulation . . . 60
1.10 Cost . . . 61
1.11 Outlook . . . 62
1.11.1 Glass Scintillator . . . 62
1.11.1.1 Light yield and intrinsic light yield . . . 62
1.11.1.2 Birks constant . . . 62
1.11.1.3 Scintillation performance changes under magnetic field . . . 63
1.11.1.4 MIP response of GFO glass scintillator . . . 63
1.11.2 Prototype . . . 64
1.11.2.1 Simulation of GS-HCAL prototype . . . 64
1.11.2.2 Design and construction plan of GS-HCAL-Prototype . . . 65
1.11.3 Beam Test consideration . . . 66
References . . . 67

Chapter 1 Hadron calorimeter

1.1 Physics Requirements of HCAL

Hadron calorimeter (HCAL) is employed in the CEPC detector system to provide an energy measurement of hadronic jets with excellent resolution and hermetic coverage. To fully exploit the potential of physics program for Higgs and electroweak physics, all possible final states from decays of intermediate vector bosons, Z, W and the Higgs boson need to be reconstructed and well identified with high sensitivity. In particular, to clearly identify hadronic final states of $H \to ZZ^* \to 4j$ and $H \to WW^* \to 4j$, the energy resolution of the calorimetry for hadronic jets needs to be pushed beyond the today's limit. In order to distinguish the hadronic decays of W and Z bosons, a 3-4% invariant mass resolution for two-jet system is required. Such a performance needs a jet energy resolution of $30\%/\sqrt{E}$ at energies below 100 GeV as shown in Figure 1.1. This would be about a factor of two better than that of the LEP detectors and the currently operating LHC detectors, which is a very challenging performance to achieve.

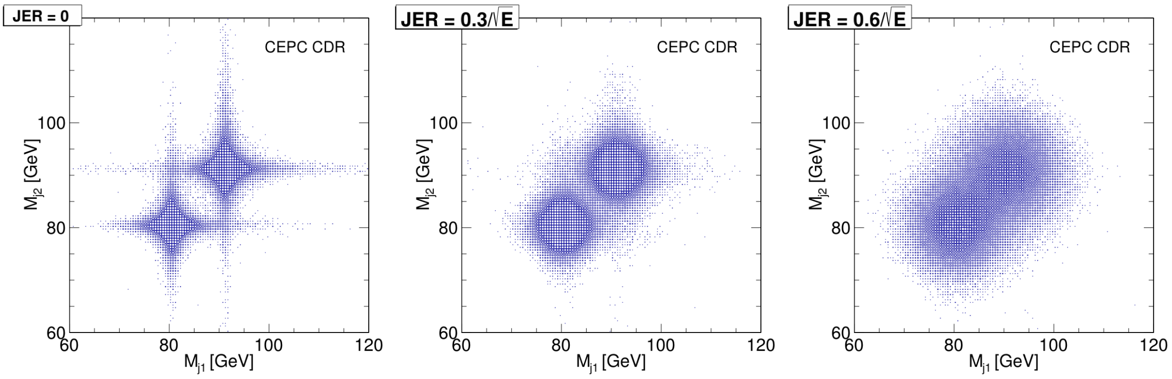

Figure 1.1: Separation of W and Z bosons in their hadronic decays with different jet energy resolutions: $0\%/\sqrt{E}$ (left plot), $30\%/\sqrt{E}$ (middle plot), $60\%/\sqrt{E}$ (right plot). A jet energy resolution of $30\%/\sqrt{E}$ is required to well separate the hadronic decays of W and Z bosons.

Two different technology approaches are pursued for the calorimetry system, the first one aiming to measure individual particles in a jet with very high granularity based on the Particle Flow Algorithm (PFA), while the second aiming at a homogeneous and integrated solution based on the dual-readout concept. PFA is the current baseline which is fully integrated in the full CEPC detector simulation.

The basic idea of PFA [1–3] is to make full use of detector subsystems to determine the energy/momentum of each particle in a jet. In a typical jet, about 65% of its energy is carried by charged particles, about 25% by photons, and about 10% by neutral hadrons. The charged particles with relative low momentum in a jet can be precisely measured by a Silicon and TPC tracker, and their tracks can be matched to their energy deposits in a PFA calorimetry with high granularity. Energy of photons can be well measured by crystal ECAL detector ($\sim 3\%/\sqrt{E}$). Only remaining 10% of neutral hadrons have to be measured by hadron calorimeter with significantly worsen energy resolution, typically $\sim 60\%/\sqrt{E}$ in the past. An essential prerequisite for realization of this idea is to distinguish among energy deposits of individual particles from a jet in the calorimetry and to minimize the energy confusion among particles. To this end, high spatial granularity is required. Therefore, PFA calorimeters feature finely segmented, three-dimensional granularity and compact, spatially separated particles showers to facilitate the reconstruction and identification of every single particle shower in a jet. This distinctive feature results in PFA calorimeters being known as imaging calorimeters.

In order to achieve the excellent jet energy resolution, extensive studies have been carried out within the CALICE collaboration [4] and within the world-wide detector R&D efforts for future colliders.

For hadronic calorimetry (HCAL) R&D with high granularity, two technological prototypes have been built, semi-digital hadronic calorimeter (SDHCAL) based on glass RPC [5, 6] and the analog hadronic calorimeter based on plastic scintillator tiles [7]. Based on test beam data collected at CERN, the typical energy resolution for single hadron is about

$\sim 60\%/\sqrt{E}$. Details about both prototypes will be described in this chapter.

Another aspect of studies is focused on the particle flow reconstruction. By combining the information from several sub-detectors and introducing the dedicated reconstruction algorithms, the jet energy resolution can be also decoupled into different parts: (1)intrinsic track momentum resolution from tracker, (2) intrinsic cluster energy resolution from ECAL and HCAL, (3)detector acceptance and (4) confusions in the PFA reconstruction algorithm. With a fast simulation based modelling [8] the contribution from these aspects are quantified as in Figure 1.2. The HCAL resolution is one of the main limiting factors, contributing 20% in the Higgs boson mass resolution. This motivated us to make tremendous efforts to improve the energy resolution. We are developing several types of novel glass scintillators with high density ($\sim 6g/cm^3$), descent light yield ($1000 \sim 2000\ ph/MeV$) and short decay time (< 1000 ns) as active material. By using high density and thicker glass scintillator, the energy sampling ratio of glass scintillator HCAL (GS-HCAL) can be dramatically increased from about 2% for PS-HCAL prototype to about 30%. Monte Carlo simulation shows that single hadron energy resolution of GS-HCAL can reach $\sim 30\%/\sqrt{E}$. Novel active material, optimal PFA calorimetry design can maximize the overall performance of the jet energy measurement, hence to achieve required jet energy resolution and to fulfill the CEPC physics requirement. The PFA-based GS-HCAL is adopted as baseline hadronic calorimeter which will result in superior performance. Detail design and performance study of GS-HCAL will be described in this chapter.

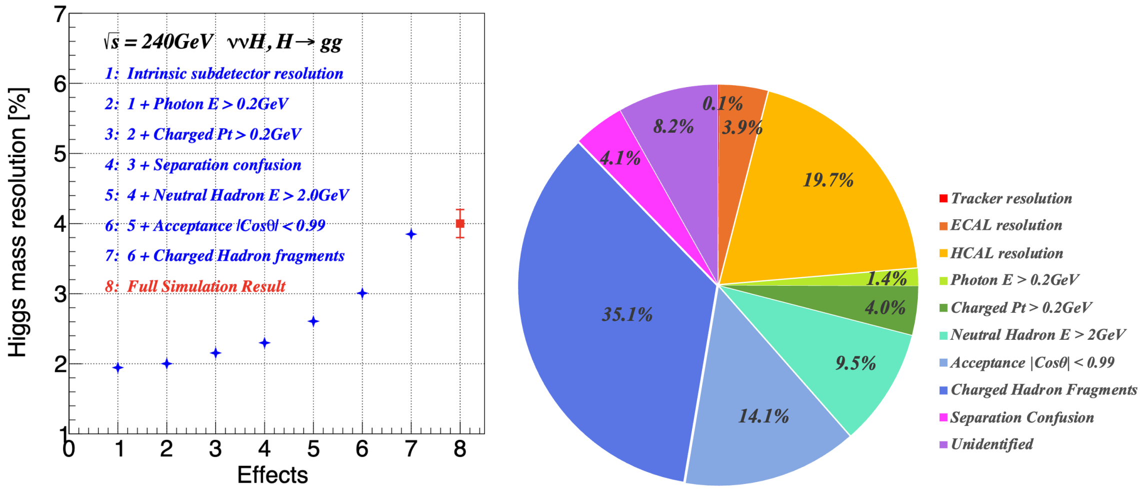

Figure 1.2: The decoupled Higgs boson mass resolution with an Arbor-based fast simulation. The HCAL intrinsic energy resolution is the leading term in the detector design aspect.

Another alternative approach for high-performance hadronic calorimeter exploits the dual-readout (DR) technique. Indeed the main limiting factor to the energy resolution in hadron calorimetry arises from the fluctuations of the electromagnetic component (f_{em}) that each hadronic shower develops as consequence of π^0 and η production. Since typically the detector response to the hadronic and em components is very different ($h/e \neq 1$), the reconstructed signal heavily depends on the actual value of f_{em}. By using two independent processes (namely, scintillation and Čerenkov light production) that have a very different sensitivity to the hadronic and em components, it is possible to reconstruct f_{em}, event by event, and minimize the effects of its fluctuations. Among the possible DR implementations, a fiber-sampling DR calorimeter, based on either copper or lead as absorber material, looks the most suitable to provide the required performance. Preliminary results of GEANT4 simulations point to possible resolutions around 30–40%/$\sqrt{E}$ for hadronic showers. However, this technology was not chosen in CEPC for cost reason.

1.2 Technical Survey of HCAL

To fulfill the stringent physics requirements outlined in Section 1.1, extensive R&D efforts have been dedicated to exploring various HCAL technologies. The baseline design adopts glass scintillator-based HCAL (GS-HCAL) due to its superior energy resolution and material budget optimization. As backup solutions, two alternative approaches have been systematically studied: the semi-digital HCAL (SDHCAL) using resistive plate chambers (RPC) and the analog HCAL with plastic scintillator tiles. These technical routes represent distinct philosophies in balancing spatial granularity, energy response linearity, and integration complexity.

The following subsections present a comparative analysis of these candidate technologies based on prototype development and beam test results. Particular emphasis will be given to the SDHCAL approach which demonstrated remarkable progress in high-granularity hadronic shower imaging. However, the GS-HCAL solution ultimately provides better compatibility with the CEPC detector's overall performance targets through its optimized balance of sampling fraction, radiation length, and intrinsic energy resolution.

1.2.1 Semi-Digital HCAL Based on RPC (SDHCAL)

SDHCAL Concept Motivated by the excellent efficiency, high homogeneity and fine lateral segmentation that gaseous detectors can provide, the concept of semi-digital HCAL (SDHCAL) is proposed for CEPC. In contrast to glass or plastic scintillator tiles, the lateral segmentation of gaseous devices is determined by the readout electronics, rather than the detector segmentation itself. In addition, the minimum thickness of active layers is also a key issue to be addressed, since the HCAL is to be placed inside the solenoid. Highly efficient gaseous detectors can indeed be built with a thickness of less than 3 mm. Whereas other detectors could achieve such performance, gaseous detectors have the advantage of being cost-effective and discharge-free. They also have fast timing performance, making them able to be be used to perform 4D reconstruction of hadronic showers, i.e. 3D spatial and 1D temporal. Such reconstruction can resolve hadronic showers from different particles and identify delayed neutrons with higher efficiency, which ultimately improves the performance of energy response.

To achieve excellent resolution in the energy measurement of hadronic showers, a binary readout of the gaseous detector is the simplest and most effective approach. However, a lateral segmentation of a few millimetres is needed to ensure good linearity and to resolve energy deposition. Such a lateral segmentation leads to a huge number of electronic channels resulting in a complicated read-out system design and excessive power consumption. A cell size of 1×1 cm^2 is found to be a good compromise that still provides a good resolution at moderate energy. However, simulation studies show that saturation effects are expected to show up at higher energy ($>$40 GeV). This happens when many particles cross a single cell at the centre of a hadronic shower. To reduce these effects, multi-threshold electronics (semi-digital) readout is chosen to improve the energy resolution by utilising the particle density information. These elements were behind the development of an SDHCAL.

Even with a 1×1 cm^2 lateral granularity of the read-out system, the number of electronic channels is still large. This has two important consequences: for one thing, the high power consumption and results in increasing temperature, which affects the performance of the active layers; for the other, the number of service cables needed to power and read out these channels also increases. These two aspects can degrade the performance of the HCAL and destroy the principle of PFA if they are not addressed properly.[9]

The SDHCAL is a sampling calorimeter which uses stainless steel as the absorber and glass resistive plate chambers (GRPC) as the sensitive medium, and is designed to be as compact as possible with its mechanical structure being part of the absorber. The GRPC and the read-out electronics are conceived to achieve minimal dead regions [5]. This design renders the SDHCAL optimal for the application of the PFA techniques [1, 2, 10]. To have more detailed studies of the performance of SDHCAL, a prototype was designed and commissioned, and beam test experiments were carried out at the PS and SPS facilities of CERN.

SDHCAL Prototype The SDHCAL prototype is comprised of 48 active layers. Each layer is equipped with a 1×1 m^2 GRPC and an active sensor unit (ASU) of the same size hosting on the one side in contact with the GRPC, pick-up pads of 1×1 cm^2 size each and 144 HARDROC2 ASICs [11] on the other side, as shown in Figs. 1.3 and 1.4. The GRPC and the ASU are assembled within a cassette made of two stainless steel plates, both of which have a thickness of 2.5 mm. The 48 cassettes are inserted into a self-supporting mechanical structure made of 49 plates, each 15 mm thick, of the same material as the cassettes, bringing the total absorber thickness to 20 mm/layer. The gap between two consecutive plates is 13 mm, which allows the insertion of one cassette with a thickness of 11 mm. In total, the SDHCAL represents approximately 6 interaction lengths (λ_I). The HARDROC2 ASIC has 64 channels to read out 64 pick-up pads. Each channel has three parallel digital circuits whose parameters can be configured to provide 2-bit encoded information per channel. This indicates whether the charge seen by each pad has passed any of the three different thresholds associated with each digital circuit. This multi-threshold readout is used to improve the energy reconstruction of hadronic showers at high energies (> 30 GeV), compared to the simple binary readout mode as explained in Reference [12].

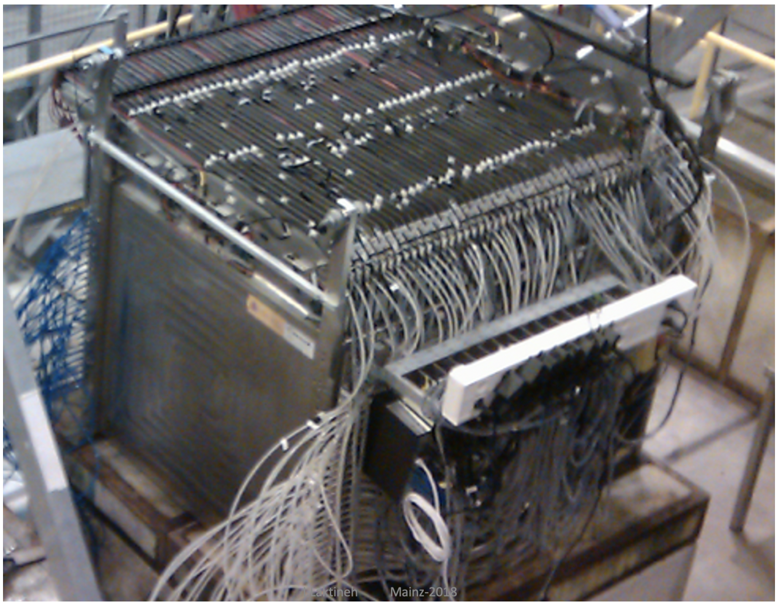

Figure 1.3: A photo of the SDHCAL prototype during the beam test experiment at CERN

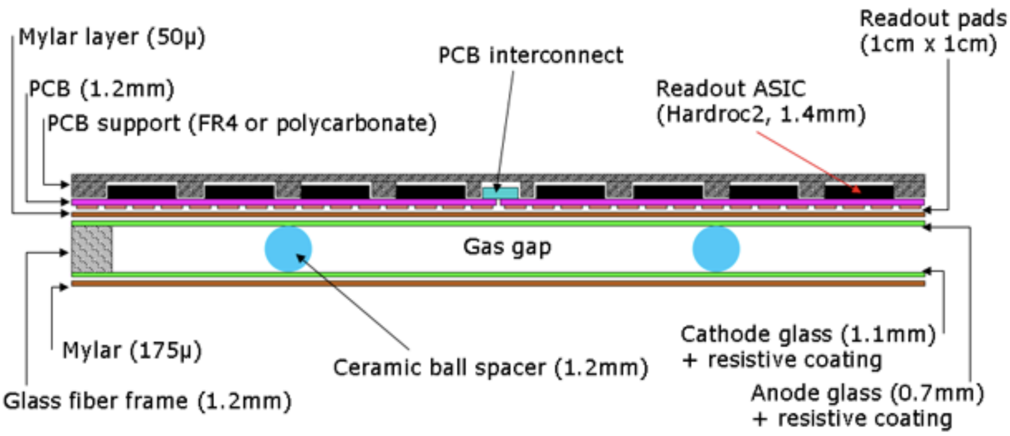

Figure 1.4: Cross-sectional view of an active layer with GRPC and readout layer. The GRPC gas gap is 1.2 mm, with two glass plates of 1.1 mm (cathode plate) and 0.7 mm (anode plate) thickness. The thickness of PCB is 1.2 mm and that of readout ASIC is 1.4 mm. (Note: Figure taken from [13].)

Test Beam of SDHCAL Prototype In 2012, using the beams provided by the SPS facility at CERN, the performance of the SDHCAL prototype was studied in the energy range above 10 GeV [12]. To study its performance under different beam conditions and at lower energy points, the SDHCAL prototype was exposed to hadrons at both the SPS and the PS facilities in 2015. It was first exposed to π^- beams of (3, 4, 5, . . . , 11) GeV at the PS facility and then to positively charged hadrons of (10, 20, 30, . . . , 80) GeV at the SPS facility. At both beamlines, about 10, 000 events were collected at each energy point. The event display of 50 GeV π^-, 50 GeV e^- as well as 110 GeV μ^- are shown in Figure 1.5.

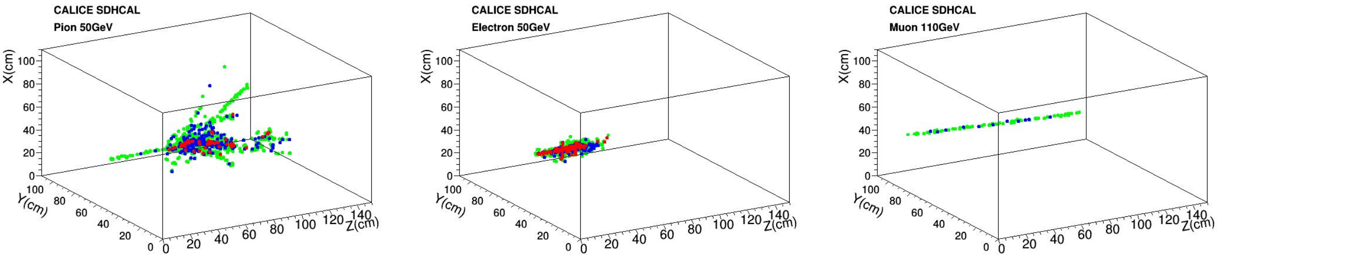

Figure 1.5: Display of SDHCAL prototype events: 50 GeV π^- (left), 50 GeV e^- (middle) and 110 GeV μ^- (right)

Energy Reconstruction Based on the information of the number of hits belonging to first threshold (NHit1), second threshold (NHit2) and third threshold (NHit3), the total energy of the hadronic shower can be reconstructed by

$$E_{\mathrm{rec}} = \alpha \cdot \mathrm{NHit1} + \beta \cdot \mathrm{NHit2} + \gamma \cdot \mathrm{NHit3}, \tag{1.1}$$

as described in Reference [12], where α, β and γ are the weight factors parametrised as the second order polynomials of the total number of hits, $\mathrm{NHit} = \mathrm{NHit1} + \mathrm{NHit2} + \mathrm{NHit3}$:

$$\alpha = \alpha_1 + \alpha_2 \cdot \mathrm{NHit} + \alpha_3 \cdot \mathrm{NHit}^2, \tag{1.2}$$

$$\beta = \beta_1 + \beta_2 \cdot \mathrm{NHit} + \beta_3 \cdot \mathrm{NHit}^2, \tag{1.3}$$

$$\gamma = \gamma_1 + \gamma_2 \cdot \mathrm{NHit} + \gamma_3 \cdot \mathrm{NHit}^2. \tag{1.4}$$

The nine parameters $\alpha_{1,2,3}$, $\beta_{1,2,3}$ and $\gamma_{1,2,3}$ are obtained from a part of the data samples of a few energy points by minimising

$$\chi^2 = \sum_{i=1}^{N} \frac{(E^i_{\mathrm{beam}} - E^i_{\mathrm{rec}})^2}{\sigma_i^2}, \tag{1.5}$$

as described in Reference [12], where E^i_{beam} denotes the beam energy and E^i_{reco} is the reconstructed energy; N is the total number of events and $\sigma_i = \sqrt{E^i_{\mathrm{beam}}}$, where the choice of $\sigma = \sqrt{E^i_{\mathrm{beam}}}$ is motivated by the fact that the expected energy resolution is approximately given by the stochastic term $\sigma / E_{\mathrm{beam}} = \alpha / \sqrt{E_{\mathrm{beam}}}$.

The reconstructed energy of 3, 7 and 11 GeV pion data samples collected at CERN PS (top row) and the reconstructed energy of 20, 40 and 60 GeV pion data samples collected at SPS (bottom row) are shown in Figure 1.6.

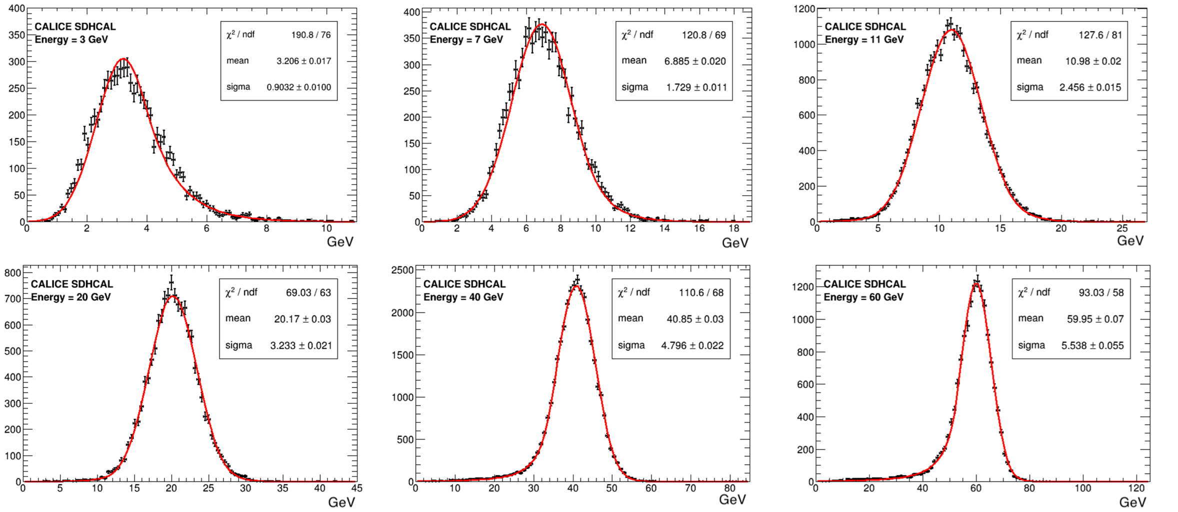

Figure 1.6: The reconstructed Energy of 3 (top left), 7(top middle) and 11(top right) GeV using pion data samples collected at CERN PS. The reconstructed Energy of 20 (bottom left), 40(bottom middle) and 60(bottom right) GeV using pion data samples collected at CERN SPS.

Energy Linearity and Energy Resolution Based on pion test beam data collected at SPS and PS with energy ranging from 3 to 80 GeV, the energy linearity and resolution of the prototype has been obtained, as shown in Figure 1.7. Apparently, the energy linearity is within about 4%, and the energy resolution for pion beam is $65\%/\sqrt{E} \oplus 2.5\%$.[6]

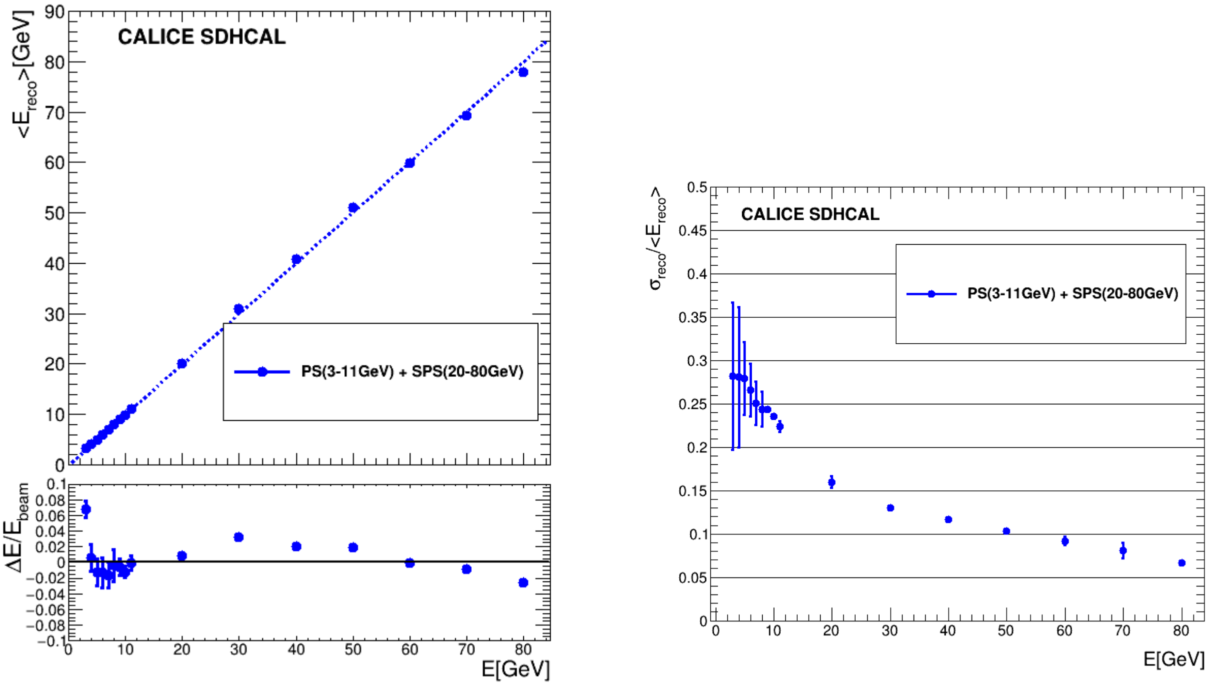

Figure 1.7: Energy linearity (left plot) and energy resolution (right plot) using all the test beam data collected at CERN with PS and SPS [6].

1.2.2 Analogue HCAL based on plastic scintillator (PS-HCAL)

Considering the performance, maturity, and price of plastic scintillators, a guaranteed and feasible solution is to develop an AHCAL based on plastic scintillators. As the baseline HCAL design in CEPC CDR, huge amount of simulation studies were performed to address the optimal design as absorber and scintillator thickness, sampling layer and cell size with respect to the physics performance [7, 14]. A prototype with $72 \times 72 \times 120\ cm^3$ scale in 12960 channels is constructed by CEPC team (USTC, SJTU and IHEP) within the CALICE collaboration to validate the key technologies in system level.

Sensitive Unit An AHCAL sensitive unit is composed of a scintillator tile and a SiPM. The 40 × 40 × 3 mm^3 scintillator tile is designed with a 5.5 × 5.5 × 1.1 mm^3 groove at the bottom to accommodate the SiPM, as depicted in Figure 1.8a. Moreover, an LED is also positioned in the groove adjacent to the SiPM for calibration. The scintillator tiles were produced using a cost-effective injection molding technique. Subsequently, the scintillator tile was wrapped with ESR, as shown in Figure 1.8b. The SiPM (HAMAMATSU S14160-1315) was placed in the groove to collect the fluorescence. A typical response of the sensitive unit to minimum ionization particles is shown as Figure 1.8c. The light yield of this unit was approximately 17 photoelectrons. The non-uniformity was approximately 6.7%.

Readout electronics system The electronics chip we used is SPIROC2E, each contains 36 channels, corresponding to 36 sensitive units. Each channel employs two preamplifiers with different gains to enhance the dynamic range, as depicted in Figure 1.9. Following the high gain preamplifier, a fast shaper and a discriminator are used to provide self-trigger. Once triggered, the signals from the high gain preamplifier and the low gain preamplifier are recorded in the analog memory after the slow shaping. Subsequently, the signals stored in the analog memory are converted into digital signals by a 12-bit ADC.

(a) (b) (c)

Figure 1.8: (a) The schematic layout of the AHCAL scintillator tile, with a groove at the bottom to accommodate the SiPM and LED. (b) A scintillator tile wrapped with the ESR film. (c) The light yield of the sensitive unit.

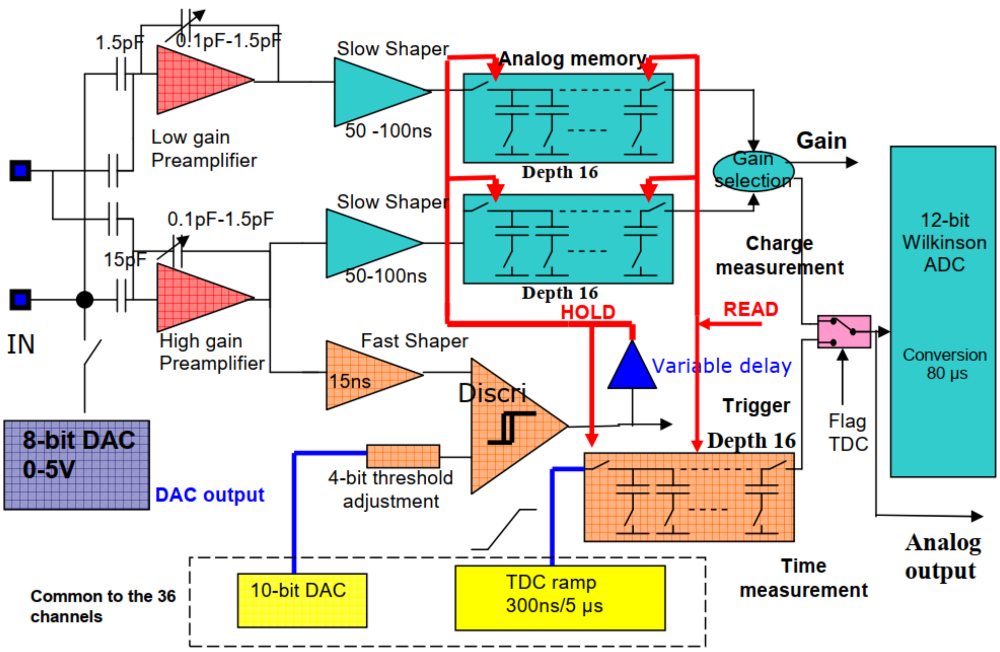

Figure 1.9: The analog circuit of SPIROC2E chip

Calibration system Two calibration systems were designed to monitor the status of electronics and SiPMs. The charge signal could be injected into the SPIROC chip to probe the response of all channels. By varying the amount of injection charge, the gain ratio between high gain and low gain could be calibrated, as show in Figure 1.10a. The other one is LED, placed adjacent to the SiPM to calibrate and monitor the SiPM. The SiPM response to the LED exhibits good single photon separation as illustrated in Figure 1.10b. The intervals between photon peaks are approximately 20 ADC, representing the gain of the SiPM.

Prototype The HCAL Base Unit (HBU) board is responsible for carrying the sensitive units and converting analog signals into digital ones. The plastic scintillators were glued on one side of HBU, as shown in Figure 1.11(a). A steel cassette was designed to support the sensitive layer, as illustrated in Figure 1.11(b). The top and bottom steel sheets of the cassettes are both 2 mm thick. This thickness ensures the stiffness of the cassette while maintaining portability. The scintillator tile, wrapped with ESR, has a thickness of 3.5 mm, while the PCB has a thickness of 2.5 mm. Additionally, a 4 mm space is designed for the electronic parts, providing a tolerance of 1 mm. The total thickness of the cassette is 14 mm. As shown in Figure 1.11(c), the scintillator tiles which glued on HBUs were placed in the steel cassette. After assembling the 40 cassettes into the structure, the whole AHCAL prototype was shown in Figure 1.12.

Prototype Test

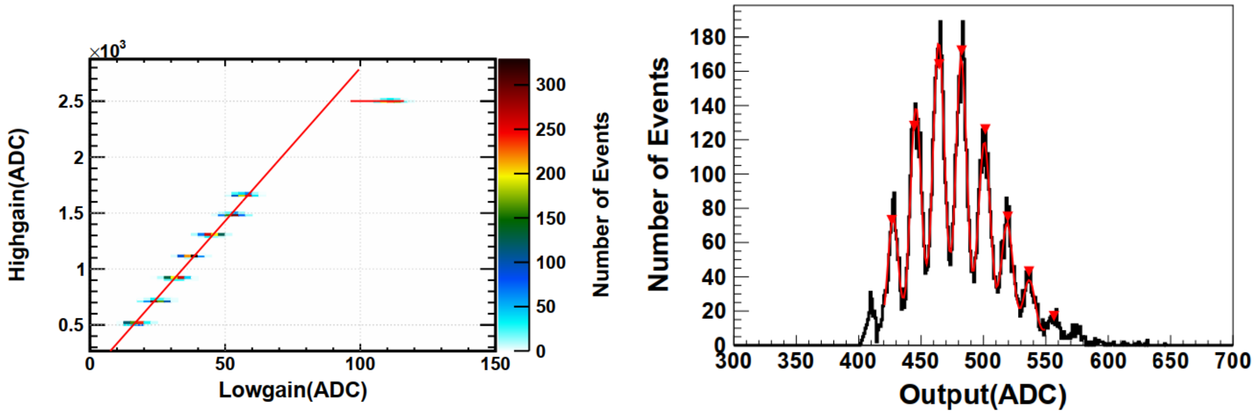

(a) (b)

Figure 1.10: (a) Low and high gain calibration for a single channel. (b) LED spectrum of a single channel

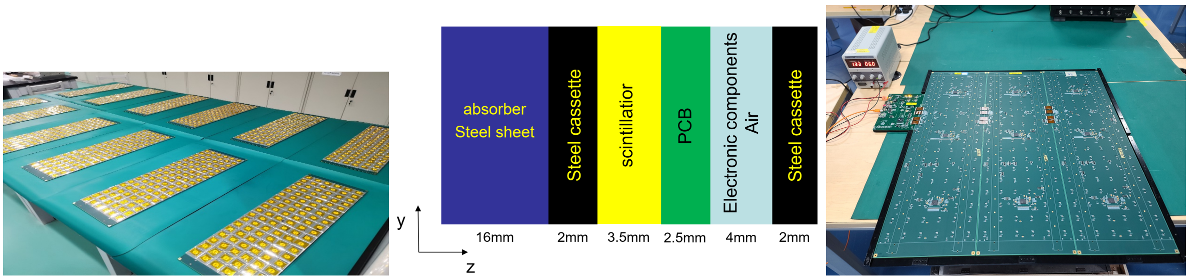

Figure 1.11: The plastic scintillators glued on HBU (left). A schematic cross-section of the AHCAL prototype (middle). The steel cassette assembled with three HBUs and the DIF board (right)

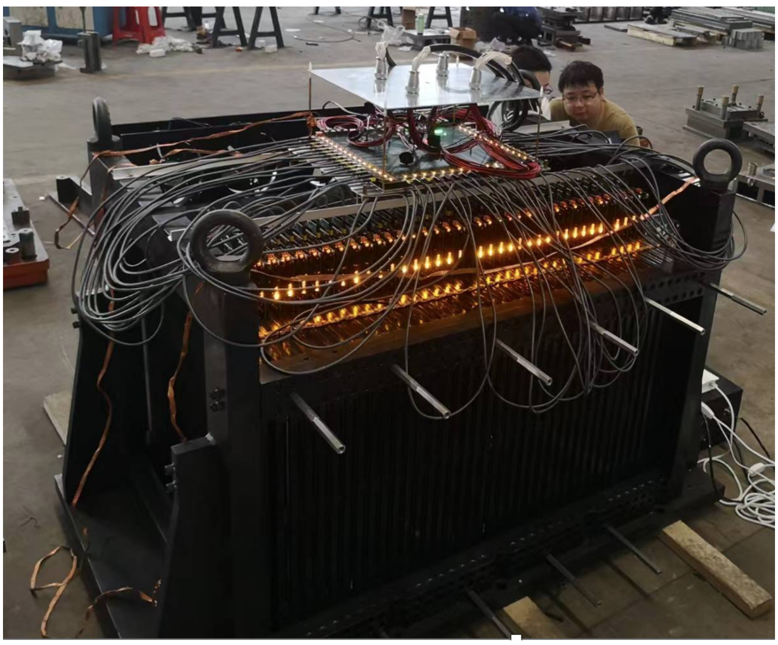

Figure 1.12: The real AHCAL prototype.

(1)Cosmic Ray Test A cosmic ray test was performed on a dedicated test platform with 40 sensitive layers. The noise, low-high gain ratio, and the MIPs spectrum were all studied. Figure 1.13a shows a typical cosmic ray event which have a clear tracker in prototype. The MIP spectrum is shown in Figure 1.13b .

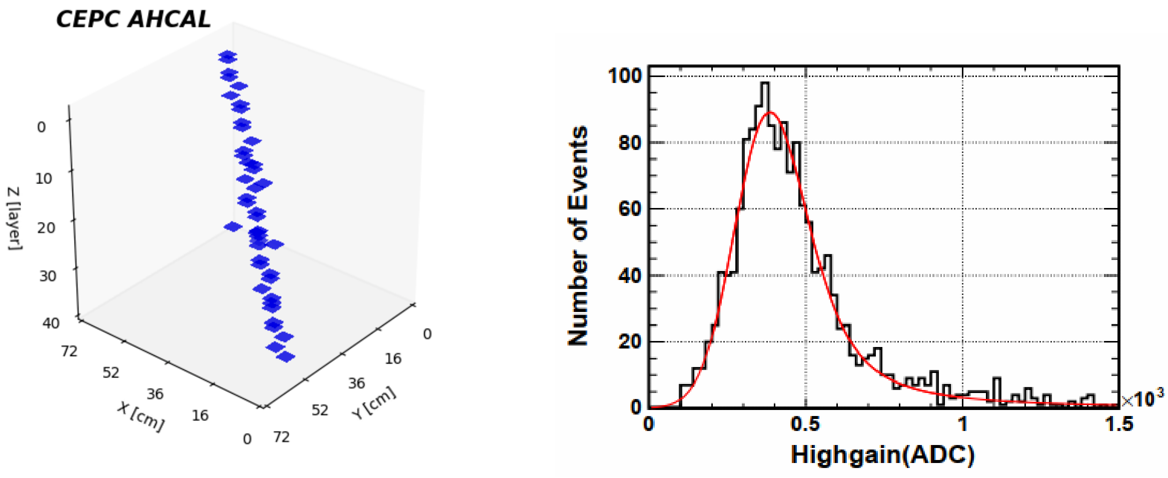

(a) (b)

Figure 1.13: (a) Display of a single cosmic ray event in the AHCAL prototype. (b) Cosmic ray spectra for a chip

(2)Beam Test The prototype carried on three beam tests at CERN to study its response to high-energy particles. We mainly studied the energy response linearity and resolution to high-energy pions in Figure 1.14a shows the energy linearity, and in Figure 1.14b is the energy resolution. The linearity is better than 1.5%, and the energy resolution is about $56.24\%/\sqrt{E} \pm 2.51\%$ [14].

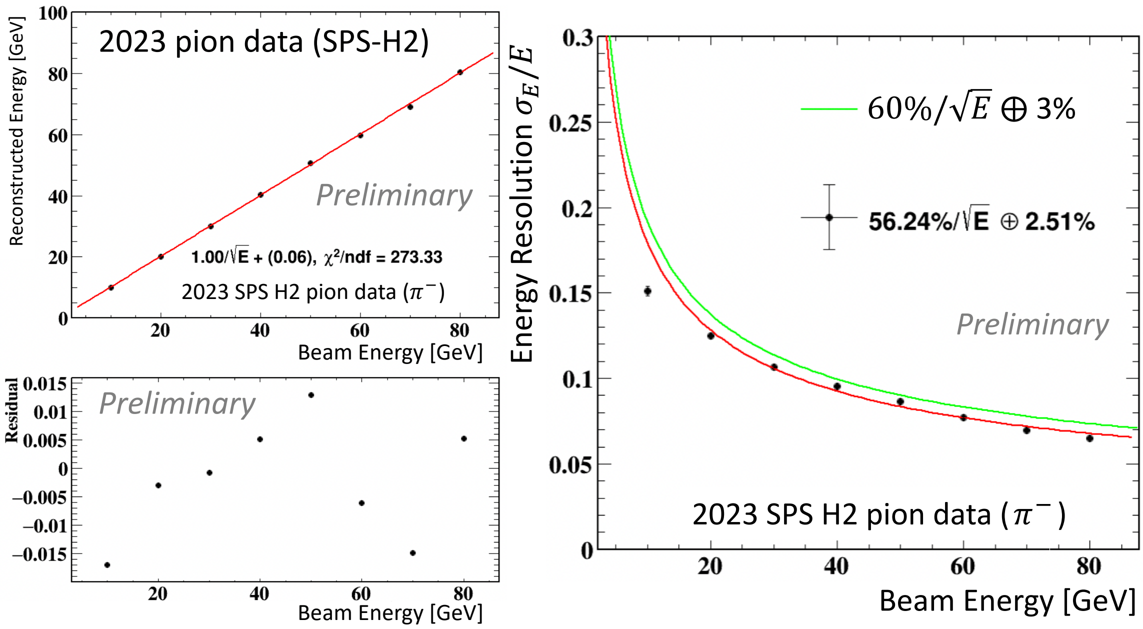

(a) (b)

Figure 1.14: (a) energy linearity and (b) energy response to high energy pions [14]

1.2.3 Glass scintillator based calorimeter

As discussed previously, gas, plastic scintillators, and crystals are frequently used as sensitive materials in calorimeter designs for high-energy physics. Gas and plastic scintillators are relatively low-cost options; however, their low density results in a reduced energy sampling fraction, which limits enhancements in energy resolution. On the other hand, crystals offer the benefit of high density and can greatly enhance energy resolution, but their high cost and limited production capacity significantly affect cost-effectiveness and restrict their extensive application in the HCAL. In comparison, glass scintillators present a promising alternative with the potensial to achieve high density, low cost, and moderate scintillation performance simultaneously, thereby offering a cost-effective means to significantly improve hadronic energy resolution.

The evolution of glass scintillator research and development comprises several distinct phases (Fig 1.15). The application of glass scintillator in calorimeters can date back to the establishment of the Crystal Clear Collaboration at CERN, which stimulated exploration of high-Z (effective atomic number) glass matrices. In 1988, TU Dortmund University proposed a design of glass scintillator (HED-1) electromagnetic calorimeter, consisting of 3×3 moduls of $8\times8\times66$ cm^3 each [15]. Compared to other crystal based homogeneous shower detectors, HED-1 glass has the disadvantage of larger radiation length and less light output. However, this can be compensated by replacing the photodiodes used for the readout by a photomultiplier. Besides, an additional advantage is the high radiation resistance of the glass and its short decay constant. This fact is of special advantage for multibunch machines as foreseen in B-factories. Then, CERN has investigated potential applications of cerium doped heavy metal fluoride glass (HFG:Ce) electromagnetic calorimeters [16]. Large size ($15\times3\times3$ cm^3) HFG:Ce glass have a good optical quality. However, the relatively poor radiation hardness of HFG:Ce still remains the main impediment in using it as a scintillator in HEP experiments where high radiation doses are expected.

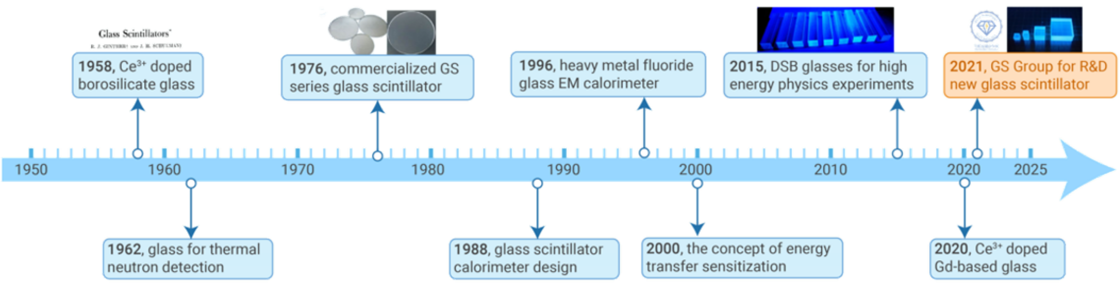

Figure 1.15: History of glass scintillator development

Besides, numerous scintillating glass-based calorimeter designs have been proposed but ultimately failed to materialize due to the excessive self-absorption, which prevented effective light transmission in traditional long-bar configurations. However, the recent advent of SiPMs and their mass production has dramatically reduced costs, enabling the practical implementation of granular scintillating glass blocks. Crucially, the development of PFA has revolutionized absorber calorimeter designs by eliminating the need for elongated scintillator geometries, making granular configurations the technically superior solution. These advancements now make glass scintillator calorimeters feasible provided they achieve: (1) a light yield exceeding 1000 ph/MeV (even with inherent self-absorption), and (2) coupling with SiPMs demonstrating $\geq$40% detection efficiency - parameters that collectively satisfy modern energy resolution requirements for calorimeter systems. The current phase (post-2020) focuses on optimizing this density-efficiency balance, targeting scintillator with high-density, considerable LY and fast decay. Concurrently, Institute of High Energy Physics (IHEP, CAS) proposed the Glass Scintillator Hadron Calorimeter (GSHCAL) concept in 2021, aimed for the deployment in next-generation colliders like the Circular Electron Positron Collider (CEPC).

1.3 Design of the GS-HCAL

The design of GS-HCAL (Glass Scintillator Hadronic Calorimeter) is a variation of the plastic scintillator (PS) AHCAL, which is widely studied within CALICE collaboration in the past two decades. The main change is on the active material, from PS to GS. Steel is kept as the absorber but the thickness is re-considered. The sampling fraction is correspondingly improved by a factor of 20 due the the high density of the glass scintillator. In such a sampling calorimeter it is the dominant contribution to the stochastic term of energy resolution, which scales approximately with $1/\sqrt{f_{sampling}}$ [17]. Meanwhile this change must bring many challenges we need to face, e.g. the density and light scintillation uniformity of GS cell, the readout system, and the heavier strucutre need to be supported. This section is organized as the parameter choices of this design based on performance requirement, and followed by an global overview of the design.

1.3.1 Key parameters of the glass scintillator

As a new material, properties of the glass scintillator play a key role in designing the GS-HCAL. We firstly arise the requirements to GS from performance aspect. These involve the glass density, the light yield, the light attenuation length, the quenching effects and the decay time. A nominal design is firstly set and the parameters are listed in Table 1.1, as the beginning of this optimization. The BMR is evaluated using the CEPCSoft with CEPC CDR detector design. The nominal structure of the barrel and endcap part of the GS-HCAL is the same as the those of PS-HCAL in CDR design.

Table 1.1: The nominal parameter setup used in the PFA performance simulation for the GS-HCAL.

Parameters	GS-HCAL
Layer Thickness	$0.125\,\lambda$, 10 mm GS + 13.9 mm Steel
Number of Layers	40
Total Thickness	$5\,\lambda$
Transverse Cell Size	$4 \times 4\,\mathrm{cm}^2$
Scintillator Density	$6\,\mathrm{g/cm}^3$
Readout Threshold	0.1 MIP

1.3.1.1 Glass density

The glass density has an impact on the BMR and compactness of the GS-HCAL. In this study, the nuclear interaction length (NIL) of each sampling layer is fixed (i.e. $0.125\,\lambda$). There are two scenarios in which the glass density can be tuned, as shown in Figure 1.16a. One scenario is that the layout of the sampling layer was fixed to $0.042\,\lambda\,\mathrm{GS} + 0.083\,\lambda\,\mathrm{Steel}$ (consistent with the nominal setup in Table 1.1). Then the steel thickness and the sampling fraction are fixed while glass density is changing. The other scenario is that the glass thickness is fixed. Then the steel thickness will decrease and sampling fraction will increase with increasing glass density. In both scenarios, the GS-HCAL will be more compact and the longitudinal granularity will be improved if the glass density is getting higher, thus improving the reconstruction accuracy and efficiency of final-state particles and the BMR, as shown in Figure 1.16b. A stronger dependence of the BMR on the glass density is observed in the second scenario, since both the sampling fraction and longitudinal granularity will increase. Nevertheless, relative degradation of scintillation and optical performance at higher density is observed during the R&D of glass scintllators, which will affect the BMR. Therefore, a trade-off is needed to achieved optimized BMR performance. According to these results, a glass density of $6\,\mathrm{g/cm}^3$ is preferred.

1.3.1.2 Light yield and threshold

A sufficiently low energy threshold is always desirable to improve the linearity and resolution. Figure 1.17 shows this impact in an ideal simulation case, where only the threshold effect is considered. An energy threshold at 0.1 MIP for each channel is preferred for an optimal energy resolution and is set to the baseline for HCAL design. Correspondingly, this threshold is constrained by the signal and noise level in the detector, including the detected scintillating light from the

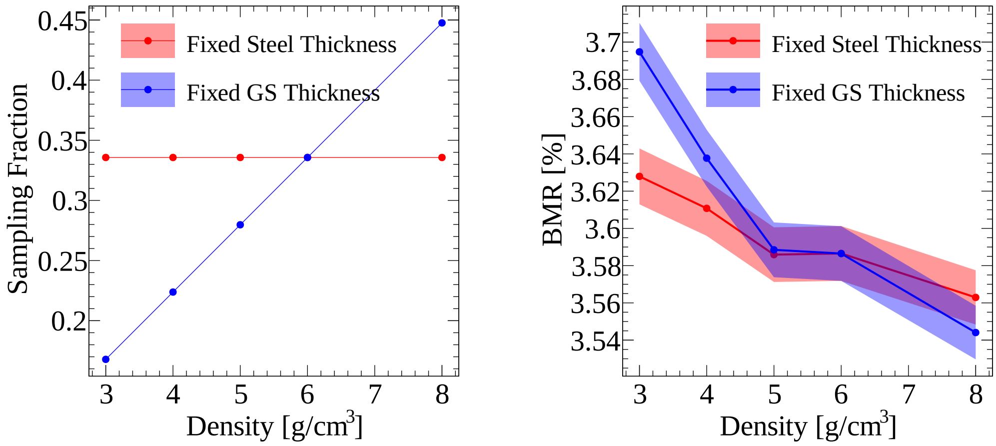

(a) (b)

Figure 1.16: The impact of the glass density on: (a) the sampling fraction; (b) BMR. [18]

glass scintillator, as well as the SiPM dark noise, electronic system noise, the beam backgrounds. Details about the noise control will be discussed in Sec. 1.5 and Sec. 1.6. From a rough estimation a minimum threshold of 5 p.e. is required, and a detected effective light output of larger than 50 p.e./MIP is necessary. More detected scintillating light can contribute to the photo-statistics, and thus improve the stochastic term of energy resolution. Figure 1.18 shows the combined effects of the detected light yield and threshold on the energy linearity and resolution.

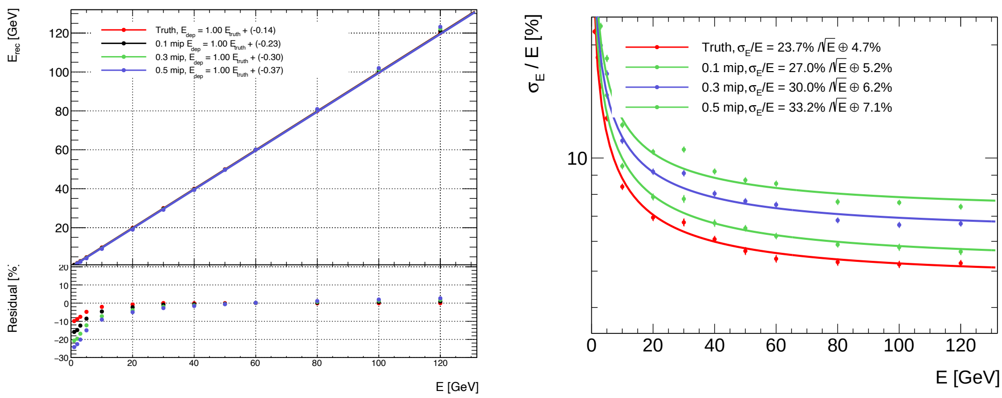

Figure 1.17: Threshold impact to the energy linearity and resolution.

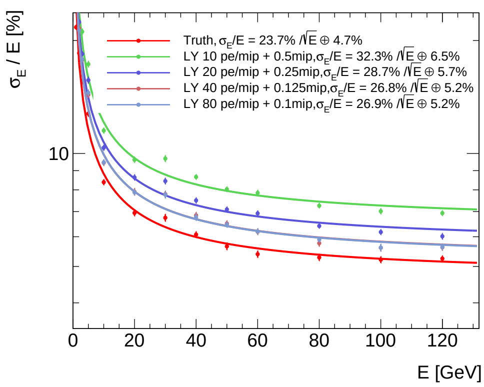

Figure 1.18: The simulated energy resolution with varies of light yield and energy threshold. The threshold is set to the maximum value between 5 p.e. and 0.1 MIP, supposing a 5 p.e. threshold is necessary to suppress the noise.

1.3.1.3 Light attenuation

With glass tile size $4 \times 4 \times 1\ cm^3$, the light attenuation effect in the glass scintillator can have significant impact on the light collection efficiency and uniformity. The attenuation length is measured with the thickness dependent light yield described in Sec. 1.4.4.1. This property, together with the intrinsic light yield and other optical parameters, are applied in the optical simulation of glass tile response to obtain the effective light collection in Sec. 1.5.3. The response map in Figure **??** is used as parameterized input for the energy response simulation, to avoid the huge amount of computing resource demands of optical simulation for every glass tile. In this simulation all Geant4 steps in each glass tile are recorded. The energy from each step is scaled with the response map $f(x, y)$:

$$E_{tile} = \sum_{steps} E_{step\ i} \times f(x, y)$$

where $E_{step\ i}$ is the energy deposition in each step from Geant-4 simulation, and the E_tile is the readout energy in one glass tile. As comparison, a simpler model only considering the exponential attenuation for 1-SiPM at central is developed. The energy readout from one tile

$$E_{tile} = \sum_{steps} E_{step\ i} \times e^{R_i/L_{att}}$$

where R is the distance between the step and tile center, and L_{att} is the effective attenuation length. The energy response of GS-HCAL is shown in Figure 1.19. The 4-SiPM scheme improves the energy resolution, and larger attenuation have benefits to the resolution.

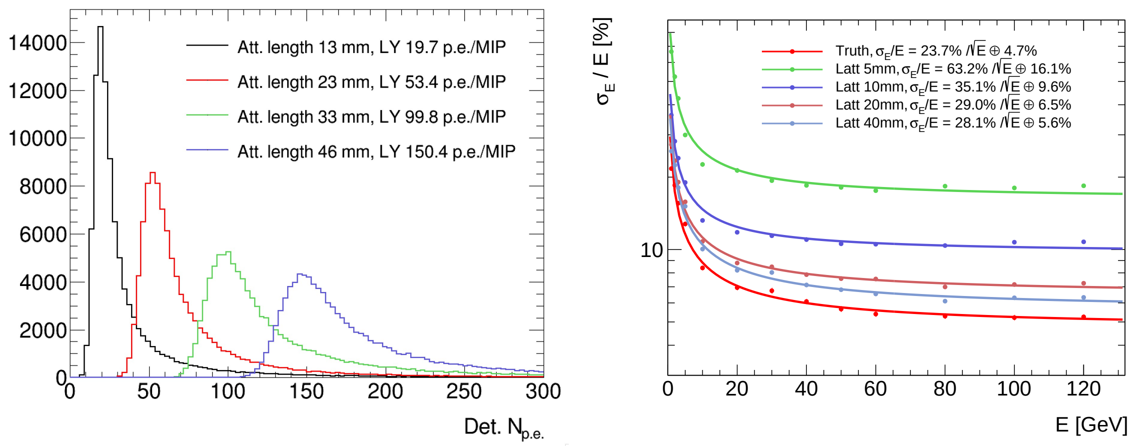

Figure 1.19: The effective MIP light output (left) and energy resolution (right) with different glass scintillator attenuation length. The intrinsic light yield and other optical parameters are fixed in the optical simulation.

1.3.1.4 Quenching effects

In the hadronic shower many particles produced by the absorption of high-energy hadrons are non-relativistic. These nucleons have energies ranging from a few MeV to several hundred MeV, and will also have much larger dE/dx (up to two or three order of magnitude) than MIPs since they are densely ionized. The contribution of these densely ionizing particles to the calorimeter signals depends crucially on saturation effects. In scintillators, saturation effects are attributed to quenching of the primary excitation by the high density of ionized and excited molecules [19]. They are usually described by Birks' law:

$$\frac{dL}{dx} = S\frac{dE/dx}{1 + k_B \cdot dE/dx} \tag{1.6}$$

where L is the amount of light produced by a particle of energy E, S is a proportionality constant and k_B is a material property known as Birks constant. The commonly used scintillators, e.g. plastic scintillator, BGO, BSO have mature studies about their quenching effects from simulations and experimental tests. For the new developed glass scintillator, this value will be measured in heavy ion beam facilities. A simulation with Geant4 go first to check the impact of the Birks constant to the energy resolution and is presented in Figure 1.20. The constant term of energy resolution shows significant impact to this properties. In the following studies, this value is set to 0.01 as a typical value for scintillators. The influence is expected to be further calibrated in the future.

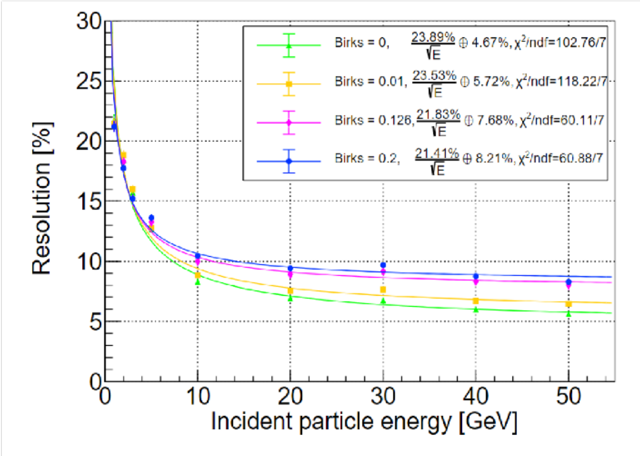

Figure 1.20: Energy resolution for different Birk's constant.

1.3.1.5 Decay time

The GS-HCAL design targets a 5D calorimeter with (x, y, z, E, t) for the future collider experiments. Among them the timing information in the calorimeter promotes extensive discussions, but is not fully studied. To different measurement precision, it can be used in different ways. With a $O(10)$ ns resolution, those noise hits from the beam induced background at different bunch crossing and from the pile up in low frequency collision environment (e.g. Higgs mode) are expected to be removed. By improving the resolution to $O(1)$ ns, the time of hits and clusters can help to identify the reconstructed calorimeter clusters, therefore help the PFA performance. Those slow components of showers can be recognized and linked to the correct showers. The pile up, e.g. the clusters from previous event in the high luminosity operation mode are possible to be tagged and then assigned to the correct event. Optimistically this leads to the next generation of particle flow, in the space time. A time resolution to $O(10)$ ps can be used to do the neutral hadron identification, which is never been done in particle physics experiment. Physically this is very helpful in the jet tagging in the future lepton collider. Quantitative relations need to be further studied with advanced simulation and reconstruction algorithms.

The decay time of glass scintillators plays a crucial role in determining the timing resolution of GS-HCAL. Specifically, the hit time must be extracted from the rising edge of the signal waveform. A faster decay time facilitates more precise identification of the timing of each hit, which is critical for accurate event reconstruction. Additionally, the decay time directly influences the readout time window of the electronic system. A shorter decay time allows the ASIC to achieve higher signal yields per unit time, enabling the design of a narrower readout time window. This, in turn, enhances the signal-to-noise ratio and reduces the required bandwidth for data acquisition systems. After comparing various scintillating materials and considering the current technological challenges associated with glass scintillators, a decay time of 600 ns has been preliminarily selected as a suitable compromise.

1.3.2 Design optimization of HCAL

1.3.2.1 Thickness of a glass cell

Both high granularity and excellent energy resolution are key factors to achieve a good BMR performance. The glass thickness in each sampling layer is the dominant factor for the sampling fraction and longitudinal granularity when the other factors listed in Table 1.1, especially the nuclear interaction length in each layer are fixed (0.125 λ_I). As demonstrated by the simulation results presented in Figure 1.21a, the hadronic energy resolution is strongly dependent on the glass thickness. A thicker glass cell is conducive to a higher sampling fraction, which can significantly improve the hadronic energy resolution. Thus, the BMR performance can also be improved by using a thicker glass cell, due to more precise energy measurements of neutral hadrons. On the other hand, a thicker glass cell leads to more GS material, which will increase the total weight of GS-HCAL and arise a much greater challenge to the mechanics. Also this leads to a thicker GS-HCAL, solenoid and yoke, increasing the cost of the detector system. As a balance, the thickness of 10 mm is selected for the GS-HCAL cell.

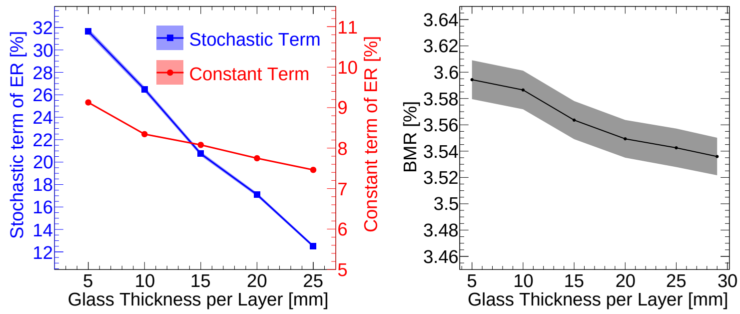

(a) **(b)**

Figure 1.21: The impact of the glass thickness on: (a) the BMR; (b) stochastic term (blue solid square) and constant term (red solid circle) of hadronic energy resolution. [18]

1.3.2.2 Transverse size

The transverse cell size in each sampling layer is the dominant factor for the transverse granularity. Based on the simulation results shown in Figure 1.22a, a significant improvement in BMR performance can be achieved by reducing the transverse cell size when the transverse cell size is larger than 10 mm. However, if the transverse cell size continues to decrease, the BMR performance will deteriorate. Although a smaller transverse cell size will improve the accuracy and efficiency in separating close-by showers, benefiting the BMR performance, an excessive number of hits may result from overly fine granularity, complicating the pattern recognition in the PFA and worsening the BMR performance. A strong dependence of the BMR on the transverse cell size has also been observed, which also demonstrates the importance of granularity in the PFA. Besides, the number of readout channels and the complexity of detector integration will also increase with a smaller cell size, as shown in Figure 1.22b. 40 mm transverse size is regarded as acceptable in BMR performance. The total readout channel is controlled within 5 million.

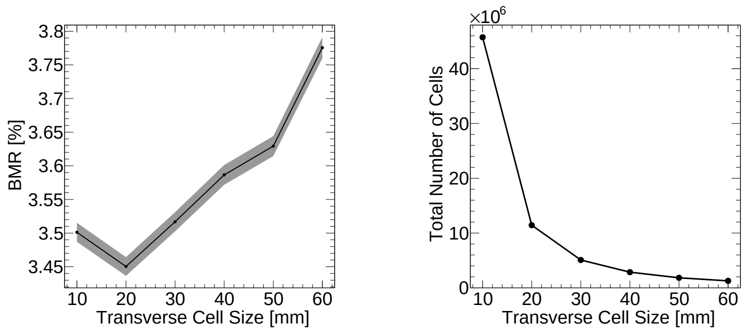

(a) **(b)**

Figure 1.22: The impact of the transverse cell size on: (a) the BMR; (b) the number of readout channels. [18]

1.3.2.3 Thickness and total interaction length

The number of layers will have an impact on the total NIL of the GS-HCAL as well as the sampling frequency, since the layout of each sampling layer was unchanged in the simulation ($0.125\,\lambda$, 10 mm GS + 13.9 mm Steel). In this setup, more sampling layers can increase the total nuclear interaction length and sampling frequency, which will suppress energy leakage, significantly improve the hadronic energy resolution and further contribute to the improvement of the BMR. This is demonstrated by the simulation results shown in Figure 1.23 and there is a strong dependence between the BMR performance, hadronic energy resolution and the total number of sampling layers. However, the volume of the CEPC detector system, especially the GS-HCAL itself and the outer solenoid and yoke, will increase with the number of layers, which also means a higher cost. A turning point can be seen in ~ 50 layers in Figure 1.23, meaning the improvement is not significant when exceed this point. Thus the total interaction length of $6\,\lambda$, corresponding to 48 layers is selected for GS-HCAL design.

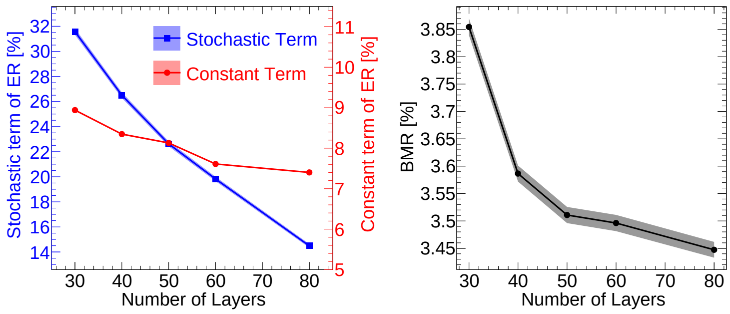

(a) (b)

Figure 1.23: The impact of the number of layers on: (a) the BMR; (b) stochastic term (blue solid square) and constant term (red solid circle) of hadronic energy resolution. [18]

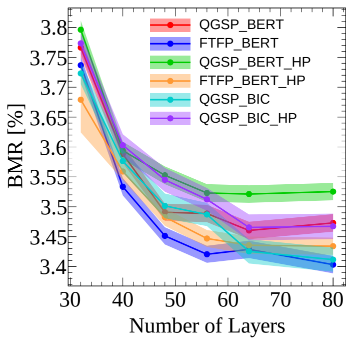

Figure 1.24: The impact of the used physics list on the BMR.

In the other aspect, the impact of the total NIL on the hadronic shower will also be influenced by the physics list used in the simulation, since the theory-driven or data-driven models that describe the hadronic cascade are different in these physics lists. As shown in Figure 1.24, six different built-in physics list in the geant4 simualtion (i.e. QGSP_BERT, FTFP_BERT, QGSP_BERT_HP, FTFP_BERT_HP, QGSP_BIC, QGSP_BIC_HP) were compared. It can be seen that the physics list used dose have a significantly impact on the BMR performance, but the general trend of BMR peformance is similar.

1.3.2.4 Dynamic range

The typical hadronic final state physical process in CEPC is the hadronic decay of Z boson, or Higgs boson like $H \to gg$. The maximum energy deposition in one cell determines the required dynamic range for HCAL. Figure 1.25

shows the energy deposited in one cell in $ee \to ZH \to \nu\nu gg$ @ $\sqrt{s}$ = 240 GeV, and $ee \to qq$ @ 360 GeV. From the distribution, a maximum of 100 MIP signal tolerance can cover more than 99.99% cases.

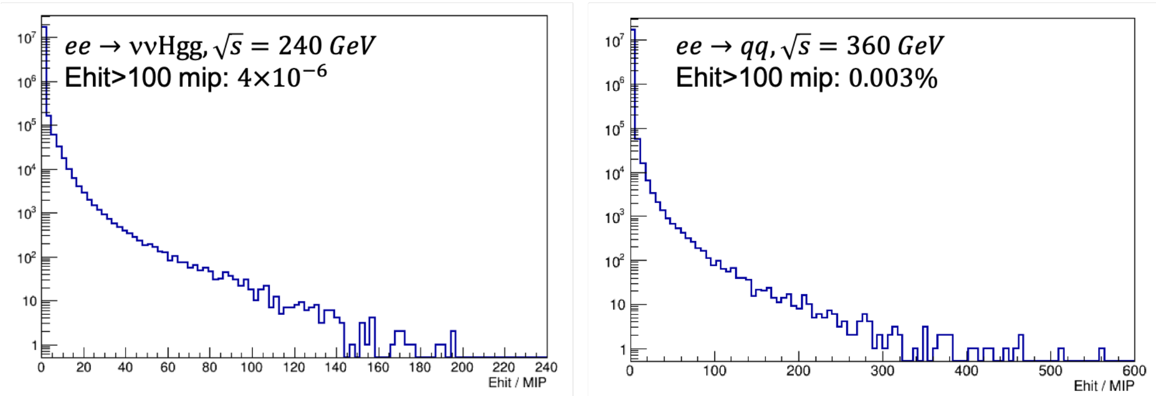

Figure 1.25: Hit energy in CEPC typical process

1.3.3 Overall design

The GS-HCAL is designed as a highly segmented calorimeter optimized for PFA. The structure consists of a barrel section and two endcaps, which together ensure full geometric coverage of the detector, as shown in Figure 1.26.

The barrel section is divided into 16 trapezoidal sectors, providing a precise and symmetric segmentation. The total thickness of the barrel is 1315 mm, corresponding to 6 nuclear interaction lengths (λ_I) from both active and passive layers to achieve sufficient energy resolution and containment for hadronic showers. The inner radius of the barrel measures 2140 mm, while the length of the barrel along the beam direction extends to 6460 mm. The longitudinal segmentation is set to 48 layers, as required by the particle flow reconstruction.

The endcap section complements the barrel to provide full geometric coverage at both ends along the beam direction. The dimension and structure match with the barrel design as 16 sectors, 450 mm inner radius and 4280 mm outer radius. The thickness also keeps consistent with barrel as 1315 mm. Each endcap weighs 360 tons, reflecting its substantial construction. The cell structure for both barrel and endcap keeps the same and is discribed below.

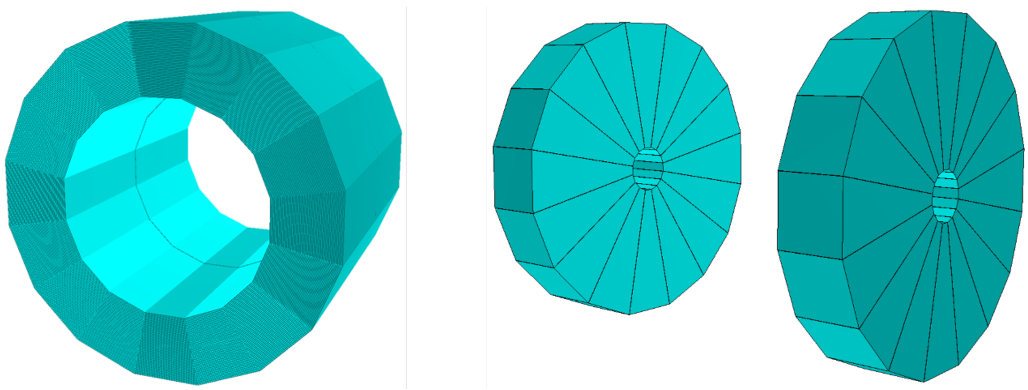

Figure 1.26: GS-HCAL geometry

A single cell design of the GS-HCAL is illustrated in Figure 1.27. The GS-HCAL employs alternating layers of glass scintillator tiles as the active detection medium and steel plates as the absorber material. This combination enhances the calorimeter's density while maintaining high segmentation for detailed shower imaging. The total thickness of an individual HCAL cell is 27.2 mm. At the top, the cell includes a 2 mm-thick upper cover, followed by a 3.2 mm layer of PCB and ASIC chips, which house the electronics responsible for signal processing and readout. Below this, the active detection layer, a 10.2 mm glass scintillator cell, is responsible for generating scintillation light when particles pass through. Beneath the scintillator cell lies a 2 mm-thick bottom cover, which provides structural support. At the bottom of the structure is the steel absorber, with a thickness of 9.8 mm, which acts as the passive material to increase the calorimeter's density and effectively stop high-energy hadrons. Silicon Photomultipliers (SiPMs), mounted on printed circuit boards (PCBs) and placed at the four corners of the glass scintillator tile, are used to improve light collection uniformity, mitigating the effects of light attenuation in the glass. The contributions of the materials are $0.0805\,\lambda_I$, $0.0425\,\lambda_I$, and $0.0024\,\lambda_I$ for the steel absorber, GS, and PCB, respectively. The sampling fraction of the calorimeter is approximately 31%. This configuration achieves a balance between material interaction length and scintillation efficiency, ensuring effective detection within a compact cell structure.

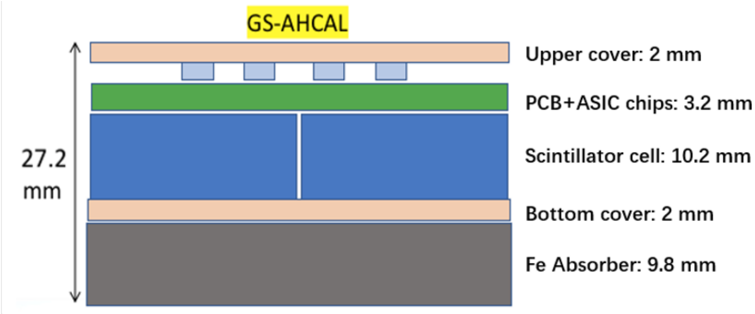

Figure 1.27: Cell structure of GS-HCAL.

The design of the GS-HCAL reflects the requirements of the PFA, which relies on fine imaging capabilities to resolve shower structures and assign them to the correct particles. The basic GS cell size is $4 \times 4cm^2$. Such high granularity of the calorimeter, with a total of 3.38 million readout channels, ensures the precision needed for particle flow reconstruction. Some abnormal shape of GS cells are designed to maximize the coverage in both barrel and endcap sections, meanwhile keep a balance of potential cost increase. For the barrel, only one type of abnormal $4 \times 5cm^2$ square cell is needed to reduce the leakage to 0.75%. The number of such abnormal cell in each layer is automatically decided by the total width. The endcap has larger variation of width in one sector along with the radius, thus more abnormal cells of 5 types of trapezoid GS tiles is needed. The leakage is estimated to be 0.55%. Figure 1.28 shows their structures. The dimension is summarized in Table 1.2.

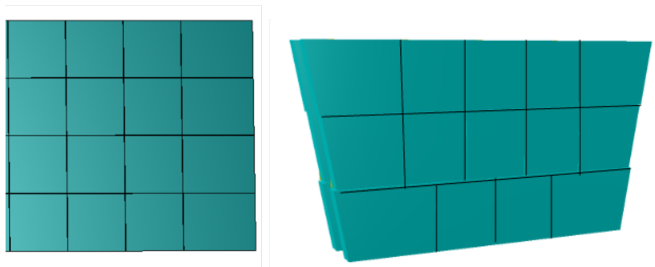

Figure 1.28: Abnormal cells in barrel (left) and endcap (right). In the barrel part only one type of $4 \times 5cm^2$ cell is placed at the corner. In the endcap several types of right-angled trapezoids are used to fulfill the gaps.

Table 1.2: Dimensions of the abnormal cells.

Barrel	$4.0 \times 5.0cm^2$ square
Endcap	4.0(upper base) $\times$ 4.8(lower base) $\times$ 4(height) right trapezoid
	4.4(upper base) $\times$ 5.2(lower base) $\times$ 4(height) right trapezoid
	4.8(upper base) $\times$ 5.6(lower base) $\times$ 4(height) right trapezoid
	5.2(upper base) $\times$ 6.0(lower base) $\times$ 4(height) right trapezoid
	5.6(upper base) $\times$ 6.4(lower base) $\times$ 4(height) right trapezoid

To evaluate the performance, this HCAL design is implemented in the software framework of *CEPCSW*. In the simulation, the glass scintillator is defined as a new material with density 6 g/cm^3 and components of Gd-Al-B-Si-Ce. The effective interaction length is 242.8 mm. Figure 1.29 shows the energy response with 10 GeV muon in the simulation. The cell structure and dimensions are constructed as described above. Apart from the sensitive cells, a simplified mechanical structure containing dominant material, as well as the cooling system and electronic integration boards are included. Figure 1.30 presents a scan of the material in unit of λ_I. With this toolkit the intrinsic hadronic energy resolution, as well as the physics performance, boson mass resolution (BMR) with full detector PFA reconstruction are studied.

Table 1.3: Parameters for GS-HCAL performance studies

Item	Value
Total number of layer	48
Total interaction length	$6\lambda_I$
Glass cell size	$4 \times 4 \times 1\ cm^3$
Glass density	$6\ g/cm^3$
Glass MIP Response	80 p.e./MIP
Glass attenuation length	2.3 cm
Threshold	0.1 MIP

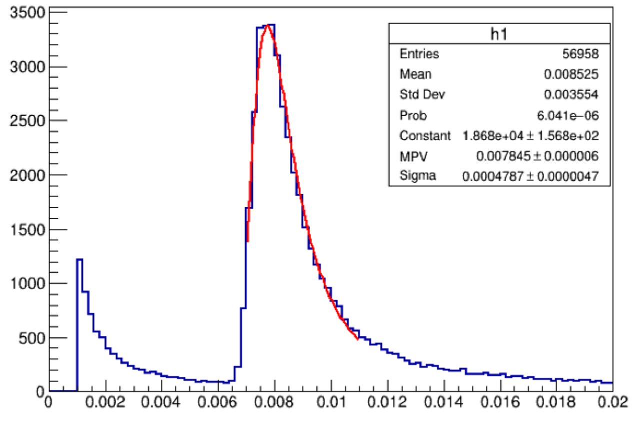

Figure 1.29: MIP energy response in simulation.

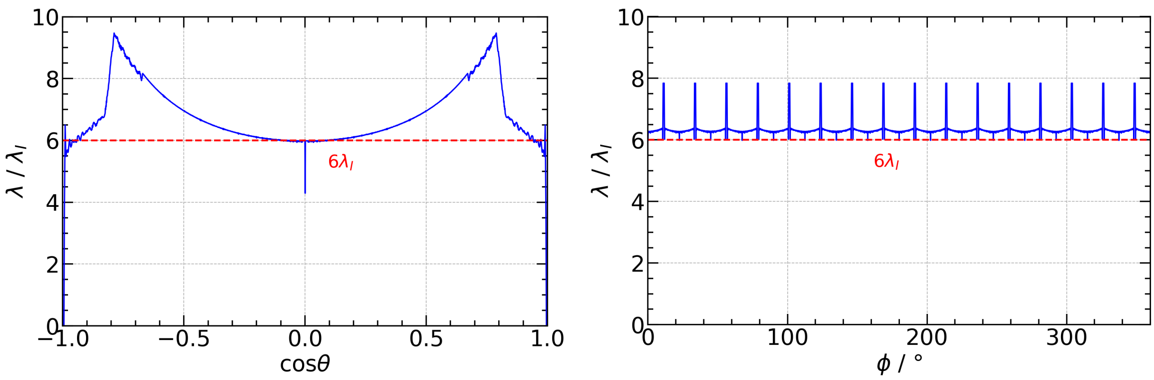

Figure 1.30: GS-HCAL material in CEPCSW simulation. The crack at $cos\theta = 0$ represents gaps between GS cells, with a width of the order of mm. The peaks in ϕ represent the seams of 16 sectors, which are filled with steel as supporting mechanics.

1.4 Glass Scintillator

1.4.1 Scintillator materials (GS)

Currently, several scintillating glass systems are being considered internationally for future calorimeter applications. The earliest developed HED and HFG:Ce glass scintillators, however, are no longer viable candidates due to their low light yield and poor radiation hardness. Since 2015, Justus-Liebig-University has been conducting research on the application of Ba-Si glass loaded with Gd (DSB) in HEP experiments. The DSB glass is a low-cost material and even at the present stage shows already attractive properties. Based on the optimal balance between glass density and scintillation performance, the best-performing DSB glass achieves a density of approximately 4.2 g/cm^3, with a light yield reaching 2500 ph/MeV and scintillation decay times of 90 ns and 400 ns [20]. The further development of the glass scintillator will be focused on the reduction of the contribution of slow decay component, and improvement of radiation hardness.

The performance of glass scintillator tiles is also crucial to the energy resolution of the GS-based GSHCAL. Since 2021, High-Density GS collaboration (in short, GS group) has been established, which focuses on the research and development (R&D) of key technologies for the high-performance GS tiles satisfying the requirements of CEPC (Table 1.4). Currently, the GS group led by the Institute of High Energy Physics (IHEP), consists of 4 Institutes from CAS, 6 Universities, 3 Companies in China (Figure 1.31). Through years of R&D, the GS group has developed a series of Ce^{3+}-doped scintillator glasses with a density of $\tilde{6}.0$ g/cm^3, light yield of $\geq$ 1000 ph/MeV, and scintillation decay time of $\tilde{3}00$ ns. The density of the scintillator glasses comes from a high content of gadolinium ($>$ 75 wt.%), and is abbreviated as GFO. The GFO glass has been patented, and glass samples with a size from 5mm $\times$ 5mm $\times$ 5mm up to 100mm $\times$ 100mm $\times$ 10mm were prepared (Figure 1.32). The GFO glasses appeared to be a feasible solution for the next-generation HCAL to be used in CEPC. All glass samples in this report are derived from the GFO glass system.

Figure 1.31: Members and Roles of the GS Group

The glass composition is pivotal for the performance. The borosilicate glass, whose base network are formed by B_2O_3 and SiO_2, is the ideal matrix composition of scintillation glass, because they exhibit the advantages of small thermal expansion coefficient, high thermal shock resistance, high surface hardness and excellent optical properties. The network modifier plays a key role in improving the performance of glass. The addition of Al_2O_3 inside the base network can greatly improve the chemical stability, increase the crystallization temperature, and reduce the crystallization tendency of the glass. The heavy rare earth elements can be added to improve the density of the glass, such as La, Lu, or Gd elements. However, the large difference between the ionic radius and the luminous center may affect its luminous performance, and

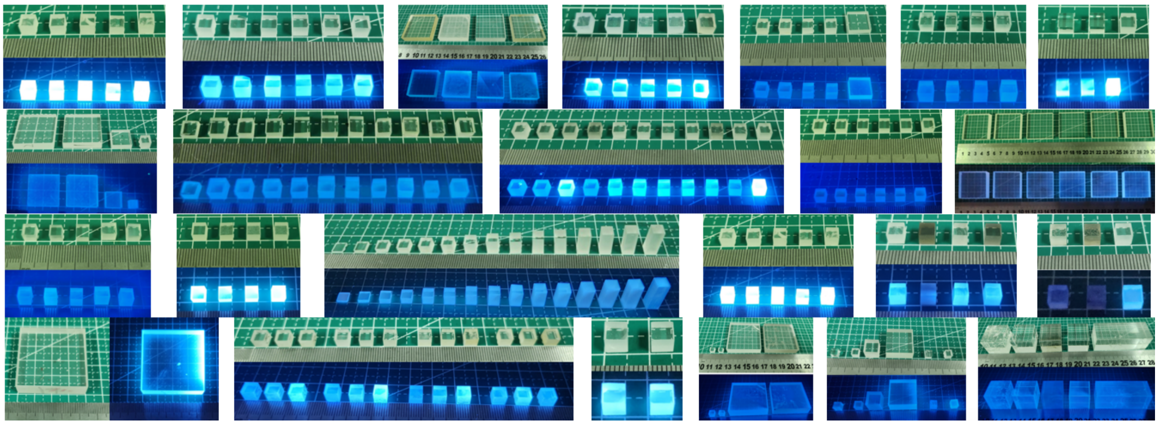

Figure 1.32: Photos of Ce^{3+}-doped Gadolinium Fluoro-Oxide (GFO) glass scintillators under the natural and UV light.

Table 1.4: R&D targets of key performance parameters for the glass scintillator (GFO), compared with the Bismuth Germanate (BGO) and DSB glass.

Key parameters	GFO glass	BGO[21]	DSB Glass [20]
Density (g/cm^3)	6.0	7.13	4.2
Melting point (°C)	1250	1050	1550
Radiation Length (cm)	1.59	1.12	2.62
Molière radius (cm)	2.49	2.23	3.33
Nuclear interaction length (cm)	24.2	22.7	31.8
Z_{eff}	56.6	71.5	49.7
dE/dX (MeV/cm)	8.0	8.99	5.9
Emission peak (nm)	400	480	430
Refractive index	1.74	2.15	
Light yield (ph/MeV)	1739	7500	2500
Energy resolution (% @662keV)	21.5	9.5	
Scintillation decay time (ns)	57.6, 506.4	60, 300	90, 400

the radioactive characteristic of the added elements must be concerned. Normally, the actinium element ^{227}Ac cannot be separated completely from La because they have similar chemical properties, which will cause α pollution to La elements. Natural Lu element is very expensive and contains radioactive ^{177}Lu isotope, which is not good for cost control and mass production. Therefore, Gd elements become the best choice for network modifiers, which have low cost, high density and low radioactive background. As for the luminescence center, Ce^{3+} is the best choice for its strong luminescence intensity, fast attenuation and wide emission. In addition, there is a $Gd^{3+} \rightarrow Ce^{3+}$ energy transfer process in the glass[22], which can further improve the scintillation performance.

At present, the GS Group has prepared more than 1000 scintillation glass samples, including stable large-size samples. The density of the glass samples is about 6 g/cm^3, and more than 50% of the samples have considerable light yield. Figure 1.33 illustrates the density and light yield of these high performance glass scintillators when compared to others. The samples from the GS group exhibit excellent performance in both density and light yield, establishing them as standout contenders on the global stage.

1.4.2 Performance of 5×5×5 mm^3 sample

Figure 1.34 shows the photograph of lab-grade GFO glasses under natural and UV light, which can already be made colorless and transparent, with almost no bubbles inside. Figure 1.35(a) shows the transmission spectrum and X-ray excited luminescence of these glass samples. The sample exhibits a cut-off edge around 360 nm with an emission peak at 400 nm. Consequently, strong self-absorption occurs within the 300-350 nm range, resulting in a poor light yield. The light yield

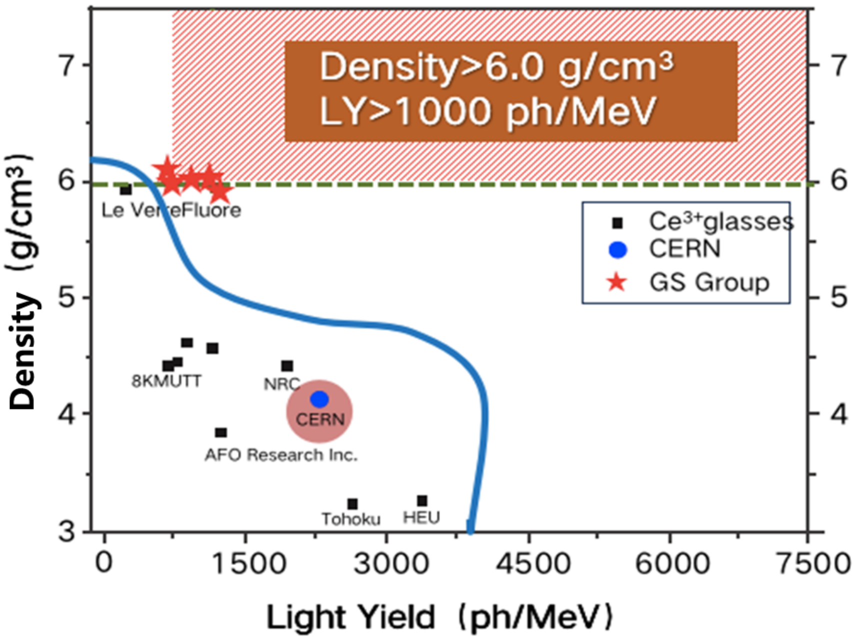

Figure 1.33: The distribution of density and light yield in international GS and GS Group samples.

of the previous GFO glass scintillator can reach up 1000 ph/MeV, which are not enough. Recently, with the continuous optimization of the manufacture process, the light yield of the glass scintillators have been greatly improved. Figure 1.35(b) shows the energy spectra of GFO glass scintillator under different processes, with BGO crystals as references. The light yield of GFO glass can reach up 1739 ph/MeV with an energy resolution of 21.5%@662 keV. Meanwhile, the scintillation decay time of GFO glass shows two components, fast and slow, which are 57.6 ns (accounting for 10.7%) and 506.4 ns respectively. It implies the GFO glass scintillators are promising potentials for future applications.

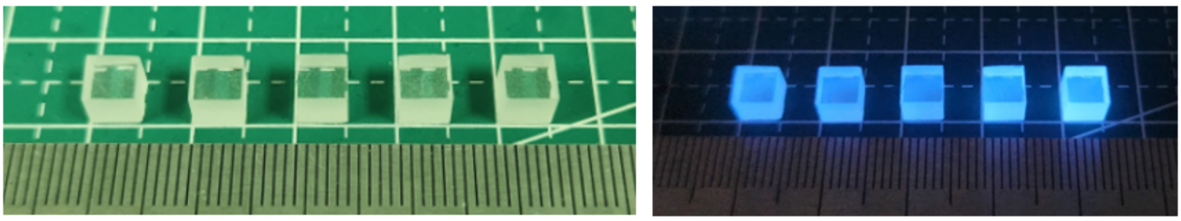

Figure 1.34: Lab-grade glasses under natural and UV light

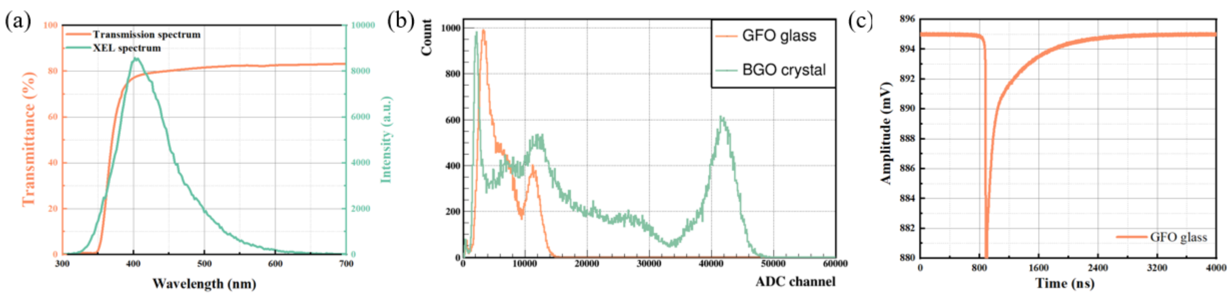

Figure 1.35: (a) Transmission and XEL spectra of GFO glass, (b) Energy spectra of GFO glass scintillators, BSO and BGO crystals. (c) Scintillation decay curves of GFO glass scintillators

1.4.3 Performance of 40mm×40mm×10mm sample

For large-scale glass scintillators in HCAL applications, stable industrial-scale production has now been achieved. Figure 1.36 shows the photograph of glasses with 40×40×10 mm^3 under natural and UV light. And the maximum dimensions can reach 100×100×10 mm^3. However, as illustrated in Figure 1.37(a), these glasses still exhibit strong self-absorption in the ultraviolet spectral region. Additionally, as the glass thickness increases, its transmittance in the visible spectrum decreases from approximately 80% to around 75%. The measurable light output of GFO glass became a critical factor for HCAL applications. Extensive γ-ray testing has demonstrated that the light yield of GFO glasses can consistently exceed 1000 ph/MeV. When measured with an XP2020 PMT, the detected photo-electron number reaches 1/3 that of BGO crystals with identical dimensions, as shown in Figure 1.37(b).

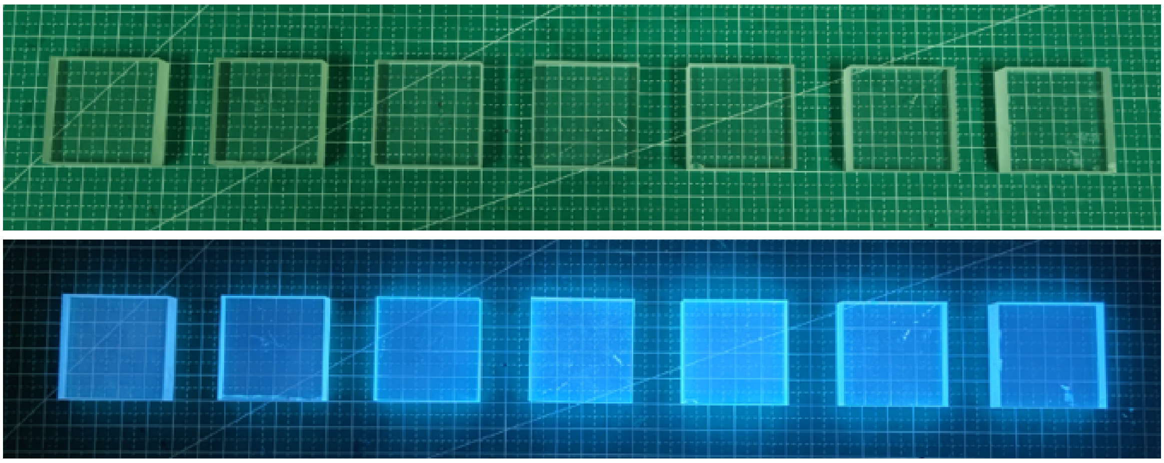

Figure 1.36: Large size glasses under natural and UV light

Figure 1.37(c) presents the scintillation decay profile of GFO glass under γ-ray excitation. While maintaining a light yield of 1000 ph/MeV, the decay time of the slow component can be controlled to below 500 ns. Although achieving faster decay time remains challenging, the large-scale GFO glass successfully maintains an optimal balance between density, light yield, and scintillation decay characteristics.

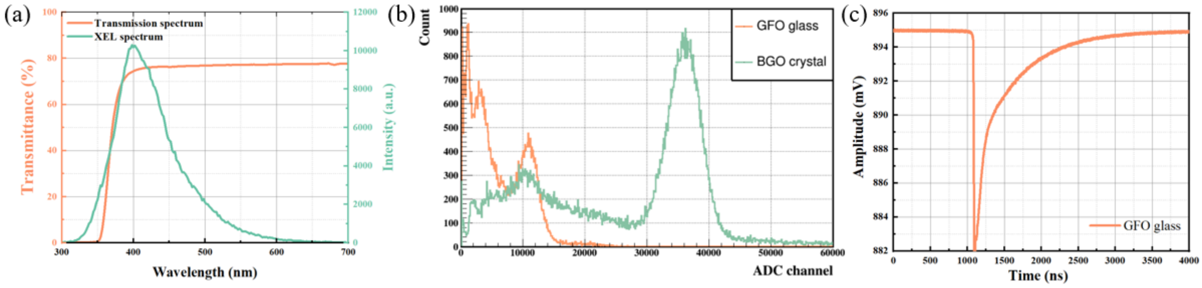

Figure 1.37: (a) Transmission and XEL spectra of large GFO glass, (b) Energy spectra of GFO glass scintillators and BGO crystal with same dimension. (c) Scintillation decay curves of GFO glass

1.4.4 Characteristic study for GFO glass scintillator

1.4.4.1 Light attenuation length

Gamma energy spectrum test The attenuation length are used to evaluate the The transmission capacity of light within the scintillator, and Several batches of GFO glass samples were prepared to measure it. The cross-section area of these samples is 5×5 mm^2, and the thickness varied within 1 to 15 mm, as shown in Figure 1.38.

According to formula:

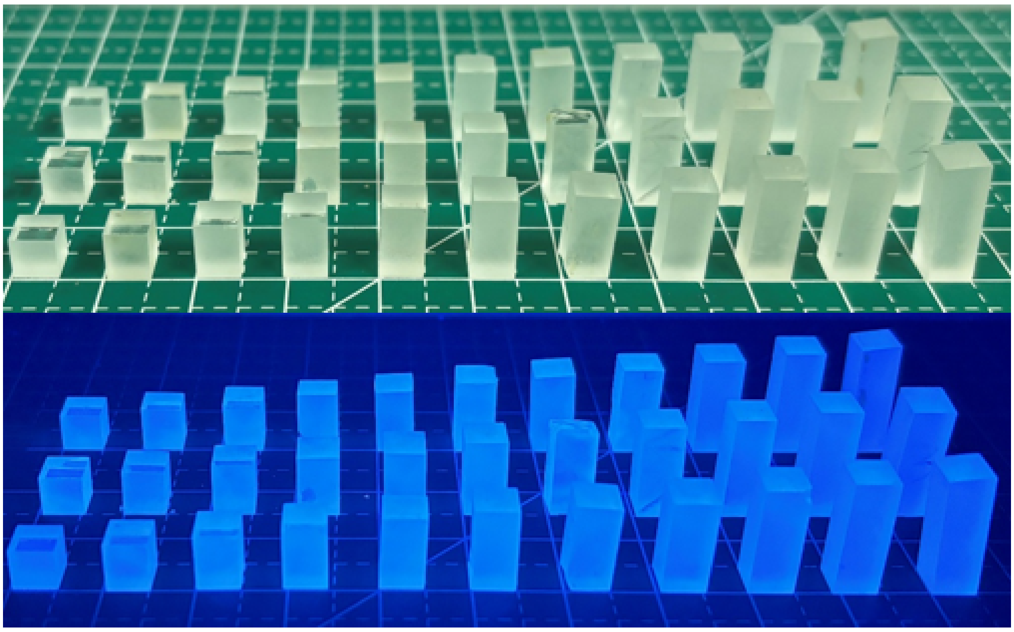

Figure 1.38: The photograph of GFO glasses under natural light and UV light.

$$LY = LY_0 \times exp(-\frac{L}{L_0}) \tag{1.7}$$

where LY_0 is the photon number at the starting position of scintillators, LY is the photon number after propagating a certain distance, L is the distance of light propagation and L_0 is the light attenuation length of scintillator. According to calculation, the actual light attenuation length of GFO glasses around their luminescence peak is 2.3±0.01 cm [23]. Compared with crystals and plastic, the glass structure and defect density as well as the self-absorption of Ce^{3+} would affect the attenuation during light transport, resulting in a small light attenuation length.

During the development of GFO glass scintillators, the light yield has been increased from 1000 ph/MeV to over 1500 ph/MeV through continuous process optimization. Therefore, the attenuation length of the glass should theoretically also show a corresponding improvement. Against this backdrop, we prepared several batches of glass samples with different thicknesses to determine the attenuation length, as shown in Figure 1.39(a). Figure 1.39(b) shows the variation curve of the light yield obtained from the γ-ray spectra of this batch of glasses. The fitting results indicate that the LAL has improved from 2.3±0.01 cm to 3.4±0.001 cm. However, since the precise deposition position of γ-ray in the glass cannot be accurately determined, the attenuation length data obtained by this method carries a certain degree of error. Therefore, it is necessary to develop a more accurate LAL measurement method.

Transmittance test In fact, calculating the light attenuation length through the variation of transmittance with the glass thickness is a simpler and more accurate method:

$$L_0 = \frac{L_2 - L_1}{ln(T_{L_1}/T_{L_2})} \tag{1.8}$$

Among them, T_L is the transmittance measured by the glass with a thickness of L. Since an external light source can penetrate the entire glass volume, it enables precise determination of the initial position in the light transmission process. Therefore, we calculated their light attenuation lengths using the aforementioned formula, with the previous samples as a comparison. As shown in Figure 1.40, the LAL of the glass system at 400 nm (around the emission peak) is 6.1728 cm. Moreover, within the visible light range, the LAL of the glass remains stable between 5.814 cm and 6.1728 cm, showing a significant improvement compared to the previous glass (with an LAL of 3.0769 at 400 nm). Additionally, the results demonstrate that the LAL data obtained through γ-ray testing tend to be underestimated. Therefore, GFO glass achieves an LAL exceeding 6 cm within the emission range, enabling efficient transmission of scintillation light internally.

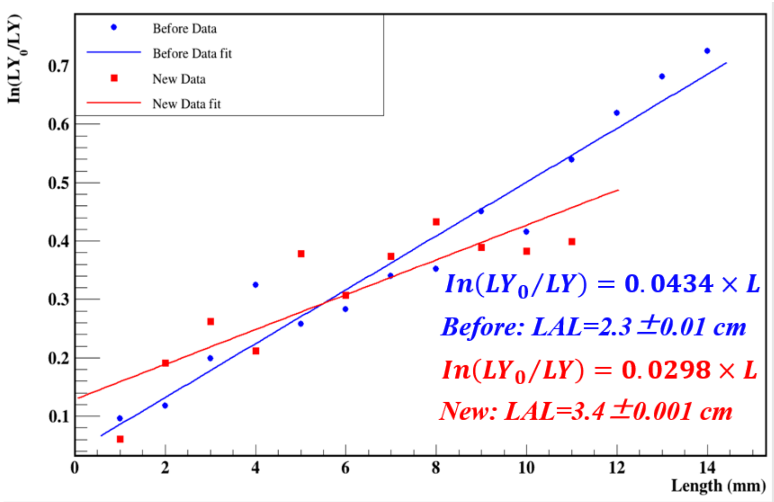

Figure 1.39: LAL measured by γ-ray spectra.

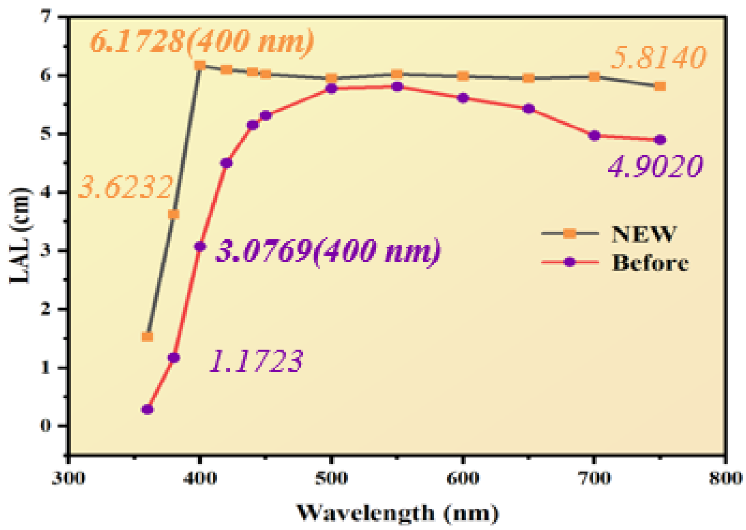

Figure 1.40: LAL measured by transmittance, compared to previous samples

1.4.4.2 Radiation Resistance

1.4.4.2.1 Proton irradiation The radiation resistance of the glass scintillator is one key factor that should be considered, because the scintillation performance of the glass scintillator will suffer from degradation after radiation. The radiation resistance of the GFO glass samples was first studied with the 80 MeV proton beam on the Associated Proton Beam Experiment Platform (APEP) [24] over a wide dose range.

In order to cover a wide enough dose range (~ 400 Gy to $\sim 4.1 \times 10^4$ Gy), a GFO glass sample of $40 \times 40 \times 10\,\mathrm{mm}^3$ was processed into 7 small glass samples with a size of $10 \times 10 \times 10\,\mathrm{mm}^3$ (denoted as #1 to #7). A Geant4-based simulation was used to calculate the deposited energy of a 80 MeV proton in a small glass sample, which is around 40.7 MeV. Then, the absorbed dose with a given flux and beam spot size can be calculated based on irradiated time, as shown in Table 1.5. The first sample was unirradiated and is used as a reference to compare the change in glass performance after irradiation. The test site in the APEP and the color change of the glass samples after irradiation are shown in Figure 1.41.

Comprehensive comparisons of their scintillation performance before and after proton irradiation were carried out, including emission spectra (X-rays excited luminescence, XEL), transmission spectra, light outputs and decay times, which are summarized in Table 1.6. The brief discussion of these results is also shown below.

- Transmission Spectra. The transmission spectra of glass samples before irradiation can reach 78% at 400 nm. The irradiated samples have experienced a significant degradation in transmittance performance. The transmittance at

Table 1.5: The irradiated time and absorbed dose of nine groups of small glass samples.

Sample index	proton flux ($p/cm^2/s$)	Irradiated time	Absorbed dose (Gy)	Beam spot size (mm^2)
#1	0	0	0	-
#2	4.86×10^9	1 m 16 s	$\sim 4.0 \times 10^2$	50×50
#3	4.86×10^9	2 m 33 s	$\sim 8.0 \times 10^2$	50×50
#4	4.86×10^9	6 m 24 s	$\sim 2.0 \times 10^3$	50×50
#5	4.86×10^9	12 m 49 s	$\sim 4.1 \times 10^3$	50×50
#6	4.86×10^9	25 m 38 s	$\sim 8.1 \times 10^3$	50×50
#7	4.86×10^9	2 h 8 m 12 s	$\sim 4.1 \times 10^4$	50×50

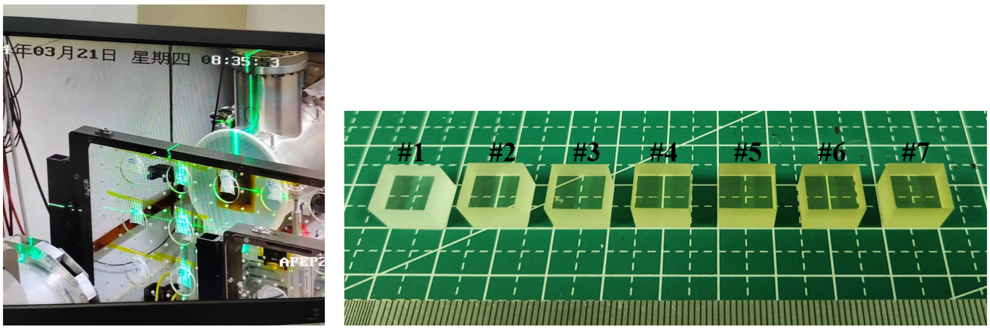

(a) (b)

Figure 1.41: The (a) experiment condition and (b) photograph of GS samples.

400 nm decreases sharply to below 10% after absorbing a dose of 8×10^3 Gy. The alteration in the transmission spectra of all glass samples is consistent with the observed color changes, indicating an increase in defects and strong self-absorption at higher doses.

- Emission Spectra. The Ce^{3+}-doped glass scintillator typically shows broadband emission due to the 5d-4f transitions of Ce^{3+} ions, within the 300-600 nm range. The emission peak of XEL spectrum from the unirradiated sample is 386 nm. In comparison, the emission peaks of these samples after irradiation ranged from 376 nm to 384 nm, which is close to that of the unirradiated sample.
- Light Output. The light output of these glass samples was measured using a ^{137}Cs source and a 2-inch PMT (PHOTONIS XP2020). The full energy peaks at 662 keV can be identified for unirradiated sample and the sample irradiated with 4×10^2 Gy. However, when the absorbed dose exceeds 4×10^2 Gy, the number of photons detectable by the PMT decreases significantly due to strong self-absorption caused by the irradiation. Consequently, the full energy peak merges with the Compton plateau, making it indistinguishable. Compared with the light output of the unirradiated sample, the light output reduced by approximately 2/3 for the glass sample irradiated with 4×10^2 Gy.
- Decay Time. A waveform digitizer (DT5751) was employed to sample the PMT signal, thereby capturing the waveform information of all γ-ray events. Subsequently, the average waveform of several hundred events was calculated. Then, a bi-exponential function was used to fit the falling edge of the average waveform, from which the decay time constants for the fast and slow components of the scintillation are extracted. As mentioned above, only the scintillation signals from the unirradiated sample and the sample irradiated with 4×10^2 Gy can be clearly

Table 1.6: The performance of glass samples after proton irradiation.

Sample index	Absorbed dose (Gy)	Transimittance (%@400 nm)	XEL peak (nm)	Light output (ph/MeV)	Decay time (ns)
#1	0	77.9	386	552	87, 985
#2	$\sim 4.0 \times 10^2$	37.4	376	187	89, 980
#3	$\sim 8.0 \times 10^2$	31.3	380	-	-
#4	$\sim 2.0 \times 10^3$	13.7	384	-	-
#5	$\sim 4.1 \times 10^3$	10.4	376	-	-
#6	$\sim 8.1 \times 10^3$	8.3	380	-	-
#7	$\sim 4.1 \times 10^4$	5.8	376	-	-

identified. Compared to the unirradiated sample, the change in decay time is insignificant at an absorption dose of 4×10^2 Gy.

1.4.4.2.2 Gamma irradiation In contrast to proton irradiation, gamma irradiation of glass samples primarily evaluates performance degradation at low dose levels ($\sim$ 10 Gy to $\sim$400 Gy). A ^{60}Co point source with an activity of 3.656×10^{11} Bq was used and the picture of the test site is shown in Figure 1.42(a). Gamma-rays with energy of 1.1732 MeV and 1.3325 MeV are emitted from ^{60}Co source. For a point source, the absorbed dose rate is inversely proportional to the square of distance between the sample and the source. The glass samples were placed along the source with difference distance to have different dose rate, and they are irradiated simultaneously for the same time. The distance between each sample and the source was pre-calculated to achieve the desired absorbed dose.

As shown in Figure 1.42(b), 6 glass samples of $5 \times 5 \times 5\,\mathrm{mm}^3$ were exposed to the ^{60}Co source for approximately 37.5 hours in total. The distance of these samples from the source varied between approximately 10 cm and 63 cm. The dose rate and total dose are summarized in Table 1.7. And Figure 1.42(c) demonstrates the color changes in the glass samples, where slight yellowing is observed after irradiation, likely due to the formation of color centers.

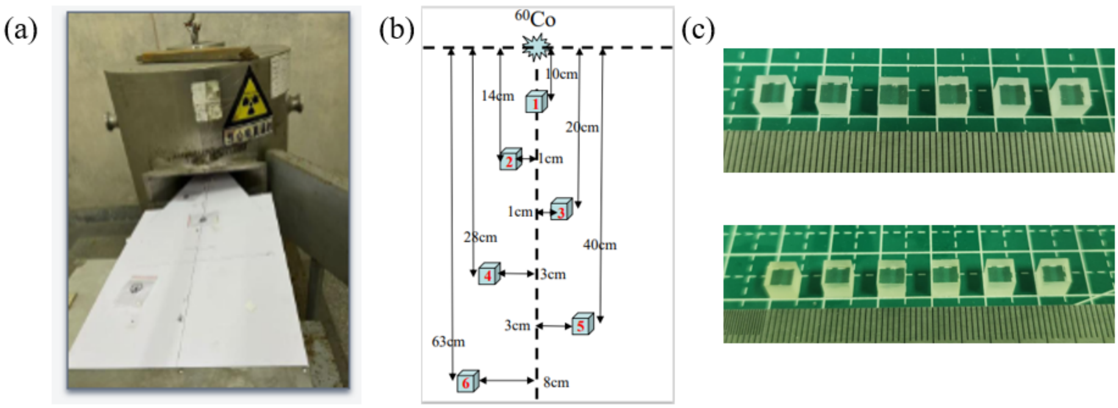

Figure 1.42: (a) The picture of used ^{60}Co radioactive source and (b) Gamma-ray irradiation test setup. (c) Changes of scintillation glass before and after irradiation.

Table 1.7: The irradiated time and absorbed dose of each glass sample.

Sample index	Distance to ^{60}Co (cm)	Dose rate (Gy/h)	Total dose (Gy@37.5 h)
#1	$\sim$10	$\sim$10	$\sim$375
#2	$\sim$ 14	$\sim$5.1	$\sim$191.3
#3	$\sim$20	$\sim$2.5	$\sim$93.8
#4	$\sim$28	$\sim$1.26	$\sim$47.3
#5	$\sim$40	$\sim$0.624	$\sim$23.4
#6	$\sim$63	$\sim$0.25	$\sim$9.4

Similar to the analysis mentioned in the proton irradiation, comprehensive comparisons of their scintillation performance before and after gamma irradiation were also carried out, which are summarized in Table 1.8. The brief discussion of these results is also shown below.

- Transmission Spectra. In general, the degradation of transmittance (i.e. the difference of transmittance before and after irradiation) in the glass sample does not exceed 14%. Compared to the results of proton irradiation ($\sim$ 400 Gy), the degradation at $\sim$ 375 Gy with gamma irradiation is less severe. The proton irradiaiton could cause more damages (including ionization and displacement types) in glass scintillator due to higher linear energy transfer or stopping power, whereas the gamma rays-induced damage generally involves ionization one.
- Emission Spectra. In general, the emission peaks of these glass samples after gamma irradiation are close to their values before irradiation, which aligns with the results observed during proton irradiation.
- Light Output. The measurement setup for light output is identical to that used in proton irradiation. After exposure

Table 1.8: The performance of glass samples after gamma irradiation, with values in parentheses representing the performances before irradiation.

Sample index	Absorbed dose (Gy)	Transimittance (%@400 nm)	XEL peak (nm)	Light output (ph/MeV)	Decay time (ns)
#1	~9.4	73.2(78.5)	384(386)	1241(1604)	72(69), 578(575)
#2	~23.4	72.5(68.2)	388(388)	1233(1709)	78(71), 589(575)
#3	~47.3	61.2(75.2)	384(396)	1159(1608)	72(67), 575(572)
#4	~93.8	61.9(70.9)	390(396)	1059(1488)	78(71), 589(582)
#5	~191.3	57.4(68.9)	392(386)	957(1647)	68(82), 578(582)
#6	~375	47.7(60.8)	386(392)	701(1882)	66(63), 579(597)

to a dose of approximately 100 Gy, the light output of the glass sample decreases to 71% of its initial level. When the absorbed dose reaches about 375 Gy, the light output further reduces to 37% of its initial level, which is essentially consistent with the proton irradiation results.

- Decay Time. In general, the decay time of these glass samples after gamma irradiation are close to their values before irradiation, which is consistent with the results observed during proton irradiation.

1.4.4.3 MIP response of the GFO

Cosmic-ray experiment is an important method to investigate the energy deposition and scintillation characteristics of glass scintillator. The MIP response of individual detector units provides the energy scale for the energy reconstruction of HCAL. Muons in cosmic rays can be used for MIP calibration. The experimental facility as shown in Figure 1.43(a) was used to measure MIP response of glass scintillator, Figure 1.43(b) shows the energy spectra of the glasses under ^{137}Cs gamma-ray source. The glasses are wrapped in Teflon foil and are coupled with silicone optical grease to a multi-pixel photon counter (SiPM Hamamatsu, S13360-6025CS). The two glass tiles at the middle were placed as coincidence. Therefore, there may be events that the middle two glasses were triggered while the upper and lower glasses are not triggered, resulting in a low count rate.

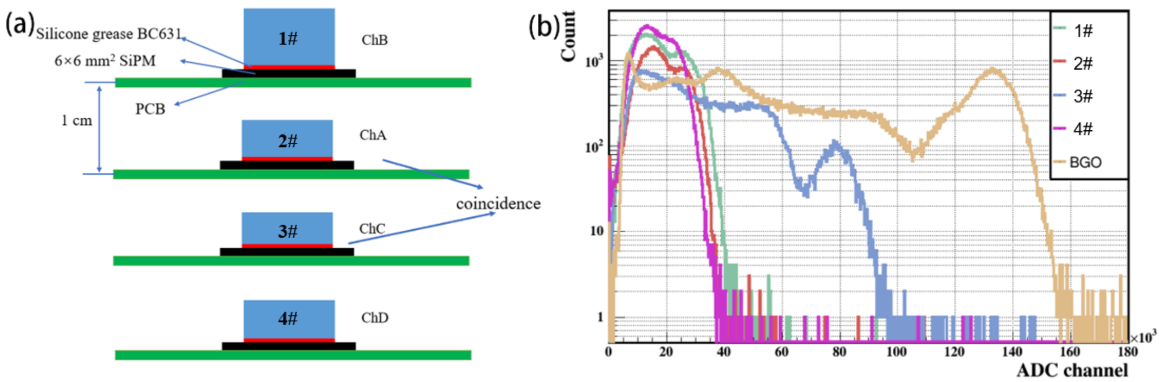

Figure 1.43: (a) Cosmic ray experiment facility, (b) The energy spectra of the glasses and BGO crystal under ^{137}Cs [25].

Figure 1.44 shows the MIP response of the glasses. The MIP response is defined as the most probable value (MPV) obtained by fitting MIP response spectrum with Landau convoluted Gaussian function, the MPV of the glasses coupling with SiPM are 326, 143, 203, 254 photo-electrons[25], respectively. Table 1.9 shows the relevant parameters of the glasses. The MIP response depends on the density and thickness of the scintillator. If F_c is defined as MIP/(Density×Thickness), then the LY should be proportional to F_c. LY/F_c were calculated to verify the accuracy of the test results, it is found that 3# and 4# glasses are similar, while 1# and 2# glasses deviate largely, possibly due to the low statistics.

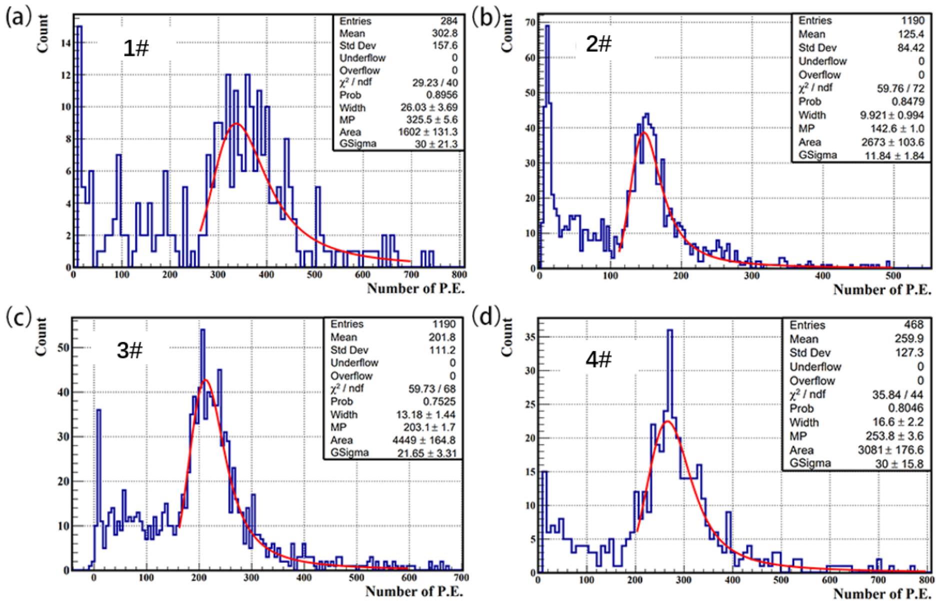

Figure 1.44: The MIP response of (a) 1#, (b) 2#, (c) 3# and (d) 4# glasses [25].

Table 1.9: The MIP, light yield and other relevant parameters of the glasses.

Label	MIP (p.e./MIP)	LY (ph/MeV)	Thickness(mm)	Density (g/cm^3)	F_c	LY/F_c
1#	326±5.6	1070±1.6	5.0	6.0	10.9	98
2#	143±1.0	1117±1.7	2.6	5.4	10.2	110
3#	203±1.7	3408±5.1	2.0	3.3	30.8	111
4#	254±3.6	1100±1.7	3.0	6.0	14.1	78

Furthermore, a dedicated test system was developed to do beamtest at the European Organization for Nuclear Research (CERN). The beamtest was carried out at CERN Proton Synchrotron (PS) T9 beamline, where muons, electrons and charged hadrons (up to 15 GeV/c) are supplied. Clear MIP signals were observed in the glass scintillator tiles. As shown in Figure 1.45(a), the MIP response of the #1 glass scintillator tile is 18 p.e./MIP [26]. And a subsequent beamtest was conducted at DESY TB22 beamline, where the facility can provide an electron beam with 1-6 GeV. The second batch of 9 glass scintillator tiles, each with standard dimensions of 40 × 40 × 10 mm^3 was tested using 5 GeV electron beam. Figure 1.45(b) shows the quasi-MIP response spectrum of #4 glass scintillator tile at DESY, and its MPV is 96 p.e./MIP. In standard dimensions, the MIP response of glass scintillator tiles is very close to reference detector GSHCAL requirement of 100 p.e./MIP.

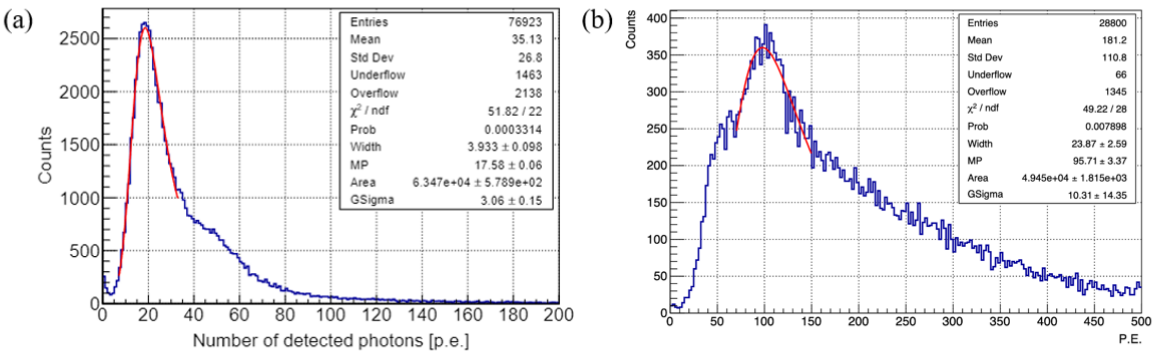

Figure 1.45: MIP response spectra of (a) #1 glass wrapped with Teflon tested by 10 GeV muon beam at CERN, (b) Quasi-MIP response spectrum for #4 glass scintillator tile tested by 5 GeV electron beam at DESY [26].

1.5 SiPMs for HCAL

1.5.1 SiPM selection

Silicon photomultipliers (SiPMs) are solid-state photodetectors capable of detecting single photons with high gain, offering a compelling alternative to traditional photomultiplier tubes (PMTs) in various applications. SiPMs are characterized by high photon detection efficiency (PDE), high gain, fast response, low operating voltage, and insensitivity to magnetic fields, making them attractive for applications requiring high granularity and fast timing, including high energy physics, medical imaging, nuclear physics, light detection and ranging (LiDAR), fluorescence spectroscopy and time-of-flight measurements. In high energy physics, SiPMs are particularly applied in calorimeter, scintillation detection, Cherenkov radiation detection and so on.

SiPMs have become increasingly popular in calorimetry applications due to their compact size, high gain, low operating voltage, good radiation hardness and insensitivity to magnetic fields. The CMS experiment at the LHC is upgrading its endcap calorimeter with the High Granularity Calorimeter (HGCAL), which uses SiPMs to read out the scintillating materials. The HGCAL is designed to handle high radiation levels and provide detailed spatial resolution for particle showers. SiPMs are ideal for this application due to their high radiation tolerance and ability to provide high granularity. The CALICE collaboration has developed a highly granular calorimeter system for future linear collider experiments. SiPMs are used to read out plastic scintillator tiles in the electromagnetic calorimeter prototypes. Their compact size and scalability make them suitable for the fine granularity required in calorimeter systems designed for particle flow algorithms (PFA). The CMS detector at the LHC has undergone upgrades to replace its hybrid photodiodes (HPDs) with SiPMs in its hadronic calorimeter. SiPMs provide better timing resolution, improved photon detection efficiency, and are more resilient to radiation damage compared to HPDs. SiPMs are also being explored for use in dual-readout calorimeters, which aim to improve the energy resolution by simultaneously measuring the scintillation light and Cherenkov light from particle showers. The fast timing and high precision of SiPMs make them help distinguish between the different components of the shower (electromagnetic and hadronic), which enhances the precision of energy measurements, particularly for hadrons.

Several companies are capable of supplying commercial SiPM products, such as Hamamatsu (HPK), Onsemi (Sensl), and several Chinese companies including CGN Capital Photonics Technology (CPT) and Joinborn (JBT, renamed Rayquant now) etc, as summarized in Table 1.10. The SiPM consists of numerous small pitches, with the pitch size, number of pixels, and active area being critical parameters that would further influence characteristics such as dark current and gain. Table 1.10 provides a parameter comparison of SiPM candidates from HPK, CPT, and JBT.

SiPM exhibits varying photon detection efficiencies (PDE) for different wavelengths, peaking typically at 420 nm. It is crucial to match the PDE with the photon emission spectrum of the scintillator to maximize the number of photons that can be detected by the SiPM. According to the emission spectrum of GFO glass scintillator (GS), its peak wavelength is at 400nm, so the PDE@400 nm are also compared. The dark count rate of the SiPM is typically in the order of 100 kHz/mm^2, which is higher for larger pixel sizes. These dark counts can introduce significant noise into the system, and require careful attention during operation.

As for GS-HCAL, the selection criteria should focus on high PDE@ 400 nm, high gain, low noise and low cost. If considered the performance only, both HPK S14160-3050 and CPT EQR20-11-3030 are good SiPM candidates currently, and can be used to do the GS cell and HCAL prototype tests already. However, semiconductor technology is advancing rapidly, the SiPM suppliers are keeping developing better performance SiPM with lower cost, including products targeting the application requirements of hadron calorimeter. So in the future, some new better SiPM candidates could be expected.

1.5.2 Dark counting rate and threshold

For SiPM, its high dark counting rate (DCR) must be considered in many cases, especially when the signal is weak. The low light yield of GS may be an issue to reach 0.1 MIP threshold for HCAL. Some methods are effective to suppress the SiPM dark noise, for example, decreasing the working temperature or increasing the electronics threshold. HCAL will operate at room temperature around 21 °, no help to reduce noise obviously. More suitable way is to cut threshold

Table 1.10: The parameters of some typical commercial SiPMs.

Supplier		HPK					NDL		JPT	
Type		S13360-3050CS	S13360-6050CS	S4160-3050HS	S4160-4050HS	S4160-6050HS	EQR20-11-3030-S	EQR20-11-6060-S	JSP-TP3050-SMT	JSP-TP6050-SMT
Pitch	μm	50	50	50	50	50	20	20	50	50
Active Area	mm^2	3.0×3.0	6.0×6.0	3.0×3.0	4.0×4.0	6.0×6.0	3.0×3.0	6.24×6.24	3.0×3.0	6.03×6.03
Number of pixels		3600	14400	3531	6331	14331	22500	97344	3364	13852
Terminal Capacitance	pF	320	1280	500	900	2000	157.5	397	170(fF)	
Breakdown Voltage (VB)	V	53±5			38		27.2±1		24.6±0.2	
Maximum operation voltage(Vm)	V	61			43		34.7±1.6		29.6	
Recommended Operation Voltage	V	VB+3	VB+3		VB+2.7		VB + 5		VB + 2	
Temperature Coefficient for VB	mV/°C	54	54		34		24.8		34.4	
Peak sensitive wavelength	nm	450	450		450		420		420	
Peak PDE @ PSW	%	40	40		50		47.8		35	
Gain		1.7×10^6			2.5×10^6		8.0×10^5		2.1×10^6	
Dark Count Rate (DCR)	kHz/mm^2	500~1500	2000~6000				150 450		120~270	140~280
Dark current	uA			0.6~1.8	1.1~3.3	2.5~7.5			0.65~1.44	3.8~5.9
PDE@400 nm	%	35			47			45		33

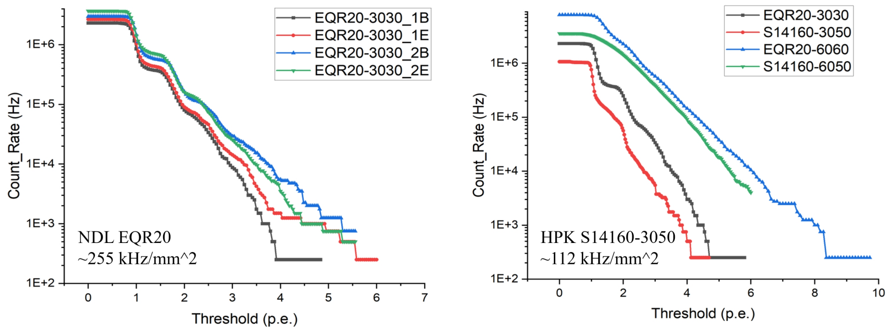

Figure 1.46: The dark counting rate versus threshold

in HCAL case. Figure 1.46 gives the SiPM DCR curve along with the threshold increasing from 0 to 10 p.e., a typical result of NDL EQR20 SiPM is about 255 kHz/mm^2 at 0 p.e. threshold, while for HPK S14160 3050 SiPM, the DCR is about 112 kHz/mm^2 at 0 p.e. threshold. As mentioned above, if GS reaches 100 p.e./MIP, then 0.1 MIP equals to 10 p.e. threshold. Figure 1.46 shows that, even at 5 p.e. threshold, the DCR has decreased to about 28 Hz/mm^2 and 12 Hz/mm^2 for NDL and HPK SiPMs respectively. So for 10 p.e. threshold, the DCR could be reduced further for 3×3 mm^2 SiPMs.

1.5.3 Study of GS-HCAL Cell

As we know, there are many scintillating materials could be chosen for hadronic calorimeter (HCAL), such as inorganic crystals (PbWO4, BGO, LYSO), noble liquids (LAr), plastic scintillators (PS) and so on, also some emerging materials, like organic crystals and scintillating glasses. The desired properties of scintillating materials for HCAL focus on: high density, short radiation length, good light yield, fast decay time, and strong radiation hardness. Surely, beyond these properties, the cost, robustness and durability, are also important. As to HCAL, a new promising option was proposed and promoted based on scintillating glass, that is called high density inorganic glass scintillator (GS), in which Cerium (Ce^{3+}) acts as the luminescent center due to its fast decay time and high light yield. Table 1.4 compares the properties of newly developed GS sample (GFO glass) and PS, BGO. As can be seen, GS sample has a high density of 6.0 g/cm^3 , a short radiation length of 24.2 cm, and an acceptable light yield of 1200 ph/MeV. The parameters that needed attention are emission peak at 400 nm and attenuation length of 4.0 cm, these affect greatly the SiPM selection and GS-HCAL cell design.

Currently, the main issues of GS1 are relatively short attenuation length and non-uniformity of luminescence, even for the default 40×40 mm^2 GS-HCAL cell size, their influence requires special attention. Some studies were complemented by both cell test and optical simulation.

1.5.3.1 Optical simulation for GS cell

Firstly, in order to conduct an in-depth study of the performance of glass scintillator (GS) and to identify future directions for improvement (such as enhancing light yield and attenuation length), we carried out several optical simulations independently of CEPC software framework (CEPCSW). Through these simulations, we analyzed the impact of GS attenuation length on the final received photons by SiPM, also quantified the specific effects of attenuation length on energy resolution and constant terms (details are in the global simulation section). This provides a scientific basis for subsequent material optimization and performance enhancement. Our goal is to lay the groundwork for the development of more efficient and stable GS materials through this research. Like other common scintillators, particles deposit energy in the scintillator, and a portion of the deposited energy is converted into visible light that propagates through the scintillator. Finally, photon detectors (SiPM) are used to detect these visible photons.

Based on Geant4, we conducted optical simulations on GS. The simulation project mainly comprised three parts. The first part is the detector geometry, and the GS geometry with SiPMs was designed through a geometric interface. Based on the baseline design of GS cell, there is one type of geometric settings of GS coupling with SiPMs: single 3×3 mm^2 SiPM at the cell center. The entire periphery of GS is wrapped in Teflon reflective film, which has a higher reflectivity than ESR film. In simulation geometry, no a small square shaped groove on GS for SiPM to be embedded, instead of embedding on the readout PCB. This will avoid making groove on GS cell itself with mold, otherwise the cost of GS production will be increased obviously. All characteristics listed in Table 1.4 are also put into simulation, especially considered the attenuation length and emission peak.

In the physical process section, a physical list and the optical processes were contained. The physical list includes ionization, bremsstrahlung, multiple scattering, pair generation, Compton scattering, and photoelectric effects. The optical processes include the generation of scintillation and Cherenkov light, Rayleigh scattering, bulk absorption, and boundary processes. In the simulation, the GS and SiPM were set as sensitive areas. The GS interacts with muons, and the SiPM with emitted photons.

A series of validations were conducted to ensure the accuracy of simulation parameters and physical processes. Figure 1.47 (a) shows the simulated photon distribution time generated by GS. The fast and slow time constants obtained by double exponential fitting can correspond to the values in the Table 1.4. Then a gamma source (Cs137) was used as the generator to simulate the response of the reflectivity of the reflective film and the receiving area of SiPM to the final light yield. The position of the gamma source is fixed at the center of the GS, and the position center of the SiPM coincides with the center of the GS. Figure 1.47 (b) shows the simulation results. The black dots represent the effective(final) light yield obtained under SiPM(assuming 40% PDE) with different receiving areas and without a reflective film on GS. The red dots is the final light yield obtained under SiPM with different receiving areas, where the GS package reflects 80% of the reflective film. The green dots represent the final light yield obtained under SiPM with different receiving areas, where the GS package reflects 95% of the reflective film. Wrapping reflective film can increase the final light yield, and the higher the reflectivity, the higher the final light yield, but the growth rate is not high. The increase in receiving area will increase the effective light yield, but it is not proportional. Most photons are still directly incident on SiPM. There are very few reflections that enter SiPM. In addition, simulation was also carried out with muons, which were uniformly placed within a 5×5 cm^2 plane and projected on GS perpendicularly. The energy of the muons was set at 5 GeV to simulate the optical response of the GS. Figure 1.47 (c) shows the deposited energy distribution of muons in the GS. The distribution is fitted using a Landau function, and the most probable deposited energy is 7.657 MeV, which is consistent with the energy deposition of minimum ionizing particles (MIPs).

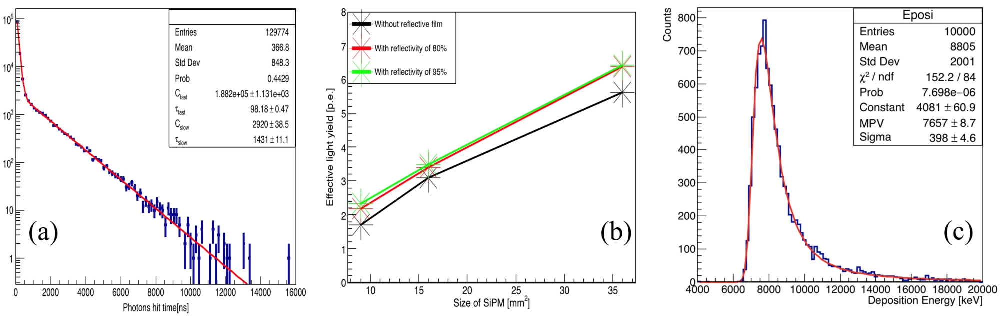

Figure 1.47: The results checked to validate the physical process in simulation, (a) Signal decay time (fast and slow components), (b) Effect of wrapping film with different reflectivity, (c) Muon deposited energy in GS cell (10mm thick).

It was found that the attenuation length and light yield non-uniformity impact the light collection efficiency significantly. Taking attenuation length as an example, Figure 1.48 compares the energy spectrum and 2-D light collection efficiency distribution for A.L. = 40, 60 and 80 mm cases. In Figure 1.48, it can be seen that the whole GS area could be ”seen” by SiPM more than 10, 23 and 42 p.e./MIP in a GS cell for A.L. = 40, 60 and 80 mm respectively. And the MPV values are 22.89 p.e., 42.01 p.e. and 59.77 p.e. respectively. That means when the GS A.L. longer than 60 mm (reached), the whole area of a GS cell could reach more than 0.1 MIP threshold, i.e. 10 p.e. @ 100 p.e./MIP.

Average effective light yield increases by nearly two times when the attenuation length is increased by 20 mm. An expected result is shown in Figure 1.48 that most of photons are collected by SiPM surfaces, due to the reflective film wrapped on GS surfaces except SiPMs. And the longer the attenuation length, the higher collection efficiency on SiPM surfaces, also the better the uniformity of collection efficiency. Based on the deposited energy, GS properties and cell

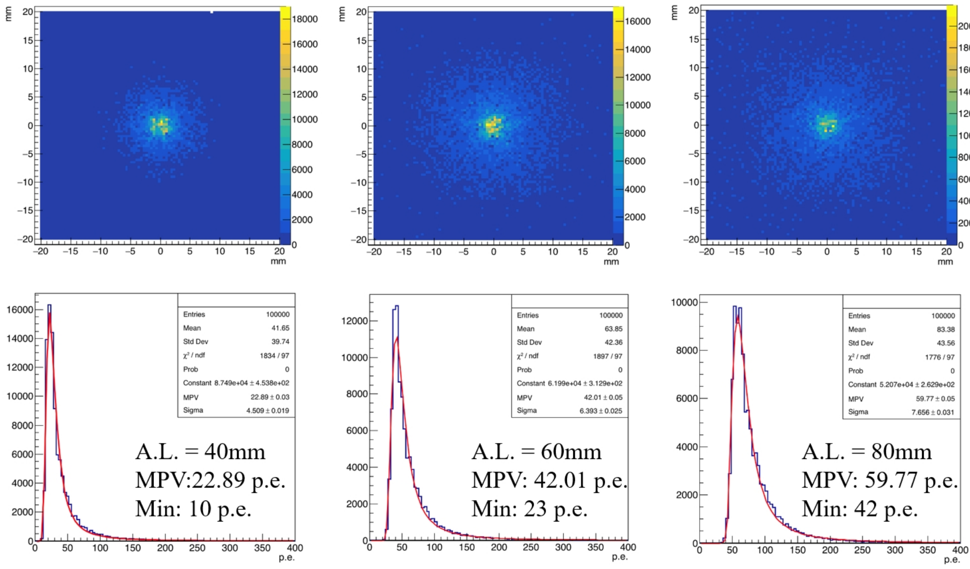

Figure 1.48: Simulation results of influence caused by attenuation length of GS. The energy spectrum (p.e.) and 2-D light collection efficiency distribution are compared for A.L. = 40 (left), 60 (middle) and 80 (right) mm respectively.

geometry, the photon collection efficiency distribution in a GS cell was obtained. The result shows that

single 3×3 mm^2 SiPM coupled with a 40×40×10 mm^3 GS block is acceptable for the GS-HCAL cell design.

The optical simulation of GS-HCAL cell is not only important for deciding the default cell setting, but also crucial to understand and improve the overall energy resolution and constant term of HCAL detector. When the more accurate optical model of GS cell is used in global HCAL simulation, the constant term could be reduced from 6.46% to 3.3% compared to a simple uniformity model (more details in global simulation section). The MIP response result of a sigle GS cell is the crucial input for HCAL detector.

1.5.3.2 Front-end electronics for SiPM test

According to the design of HCAL, there will be more than five million channels of SiPMs, so the electronics for SiPMs is crucial for signal processing and readout. It typically includes the following components:

a) Bias Voltage Supply: Provides the necessary operating voltage for the SiPM. Stable and low-noise voltage supplies are essential for optimal performance.
b) Pre-Amplifier: Amplifies the small current pulses produced by the SiPM to a level suitable for further processing. Charge sensitive pre-amplifiers (CSP) are commonly used.
c) Shaper: Shapes the amplified pulses to improve signal-to-noise ratio and optimize timing resolution. Shaping can be implemented using analog or digital techniques.
d) Discriminator: Generates a digital pulse when the shaped signal exceeds a predefined threshold. This allows for photon counting and timing measurements.
e) Time-to-Digital Converter (TDC): Measures the time difference between the SiPM signal and a reference signal, enabling precise timing measurements.
f) Analog-to-Digital Converter (ADC): Digitizes the amplitude of the shaped signal, allowing for energy measurement.
g) Data Acquisition System (DAQ): Collects and processes the digitized data from multiple SiPM channels.

CEPC has an overall electronics design for all detectors, however this electronics is not available for performance or prototype tests currently. In order to study and test SiPMs and GS cells, a customized front-end electronics (FEE) solution is very important and urgently-needed. The customized FEE aims to adapt most of the commercial SiPMs and provide design reference for HCAL electronics. The design of HCAL electronics will be considered as a part of CEPC electronics and will be realized in a few years. The key part is the front-end electronics, which must consider the specific requirements of the application, such as dynamic range, charge and timing resolution, event rate, power consumption and so on.

The HCAL electronics will cover all above requirements and integrate into the whole CEPC electronics, however, it will be ready in several years, therefore a current and fast electronics solution is needed for SiPM study and HCAL prototype. Commercial products are direct option, but lack of universality and flexibility, especially for the FEE. For example, each SiPM manufacturer provides a pre-amplifier for their own SiPM products, but it is not suitable for other manufacturers' SiPMs. And these pre-amplifiers are most single channel. For HCAL, it is very possible that four SiPMs will be coupled with one glass scintillator, due to the short attenuation length and non-uniformity of luminescence of GS. And many SiPM candidates also need to be tested. So the more reasonable and flexible solution is to design a commonly used FEE for SiPMs.

Table 1.11: Requirements of HCAL SiPM for electronics.

Item	Requirement
Charge dynamic range	0.8∼800 pC (10∼10000 p.e., 0.1∼100 MIPs) @100 p.e./MIP
Timing measured range	TBD from electronics
Charge resolution	0.8 pC (10% of 1.0 MIP, i.e. 10 p.e.)
SiPM capacity	$\leq$ 100 pF
SiPM gain	$\geq 5\times10^5$
Average event rate/channel	Berral mean 0.24 kHz, Endcap mean 1.45 kHz
Max event rate/channel	Berral max 6.2 kHz, Endcap max 46.3 kHz
Rising edge	2∼3 ns
Typical signal	2∼3 mV/p.e.
Other requirements	FEE gain adjustable in 2/3 levels, Signal saturation protection HV independent, adjustable by layer, Random trigger (for test) Calibration function

The FEE for SiPMs is critical for maximizing the SiPM performance in terms of gain, noise reduction, and timing resolution. Careful impedance matching between the SiPM and the pre-amplifier is crucial for minimizing signal reflections and maximizing signal transfer. Temperature compensation circuits are often employed to stabilize the SiPM gain and reduce the temperature dependence of DCR, or a cooling system is applied to control the whole running temperature of HCAL. SiPMs generate fast pulses with rise times on the order of nanoseconds, which must be accurately captured and processed. The dynamic range of the signal, which depends on the number of photons detected, can vary significantly between events. Therefore, the FEE needs to handle both small and large signals without distortion. According to the results of CEPC global simulation and glass scintillator performance study, HCAL needs to cover 0.1 to 100 MIPs, with one MIP being equivalent to about 100 p.e. Table 1.11 lists the requirements of HCAL SiPM for electronics, which are considered to match the performance of current domestic SiPMs and those in the future.

Design considerations for front-end electronics include:

a) Pre-Amplification: SiPM signals are weak (on the order of microvolts to millivolts), so pre-amplifiers are required to boost the signal strength. Low-noise amplifiers (LNAs) are often used to preserve the signal's integrity while reducing noise.
b) Noise Filtering: SiPMs are subject to noise from various sources, including thermal noise (dark counts) and afterpulsing. Front-end electronics must include filtering stages to suppress noise and improve the signal-to-noise ratio (SNR).
c) Shaping Circuits: Pulse-shaping circuits may be implemented to optimize the signal for digitization and to match the timing characteristics of subsequent processing stages.
d) Temperature Compensation: SiPM performance is temperature-dependent, with dark noise increasing significantly at higher temperatures. Front-end electronics can include compensation circuits to adjust for these variations. For HCAL, if the cooling system applied to control the temperature, then temperature compensation can be cancelled.

A compact, high speed, four-channel SiPM pre-amplifier has been designed and implemented for HCAL SiPM study, as shown in Figure **??**. The pre-amplifier matches the GS cell perfectly and provides four independent channel readouts. One high voltage supplies four SiPMs and suitable for HPK, NDL and many other brand of SiPMs. This pre-amplifier consists of pole zero cancellation (PZC) circuit to reduce the long falling time, and LMH6629 amplifier chip to reach a large bandwidth and low-noise level. The test results show that the performance of this pre-amplifier is impressive:

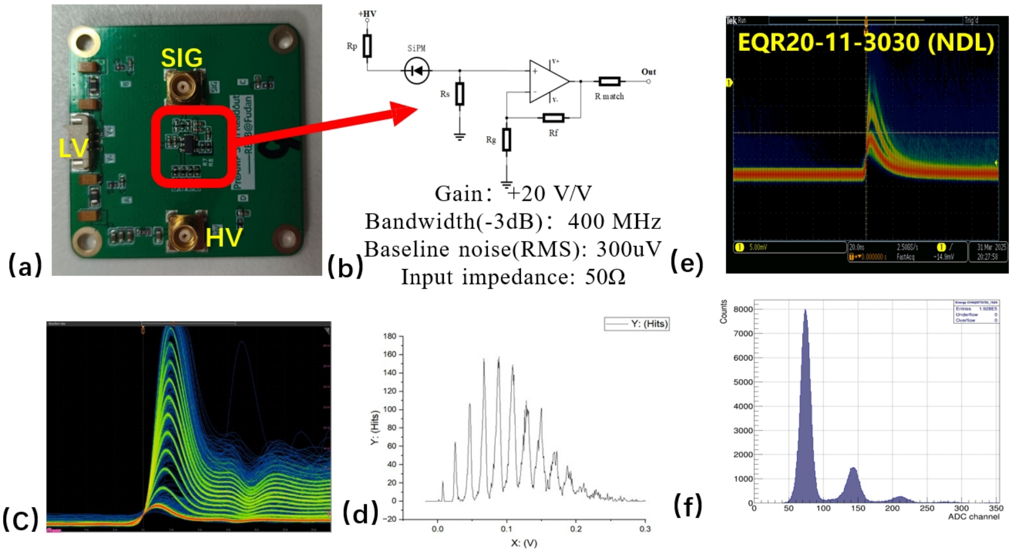

Figure 1.49: The pre-amplifier for HCAL SiPM study. (a) one pre-amplifier channel PCB coupling to GS cell. (b) the schematic diagram of the pre-amplifier. (c) and (d) the performance of the pre-amplifier. (e) Signal of one 3×3 mm^2 SiPM (EQR20 11-3030D-S) coupling with a readout PCB. (f) ADC distribution of dark noise of a 3×3 mm^2 NDL SiPM.

a) Bandwidth: >400 MHz,
b) Baseline noise level: 0.6 mV, total noise levels <1 mV
c) Large dynamic range: input signal up to 170 mV,
d) A very fast rising time, reduce the pile-up when using a large SiPM or array.
e) Time resolution <50 ps, 25 ps for large signal.

1.5.3.3 GS cell test

The simulation results indicate the GS cell design direction, so a real GS cell sample was made to check the effective light yield of different cell settings. In Section 1.5.1, some typical commercial SiPMs were compared, it must be pointed out that the HPK S14160 series SiPMs have the higher PDE at 400 nm. Therefore, in our case of GS cell, Currently HPK S1330-3050HS SiPM was chosen and mounted on a readout board with pre-amplifier.

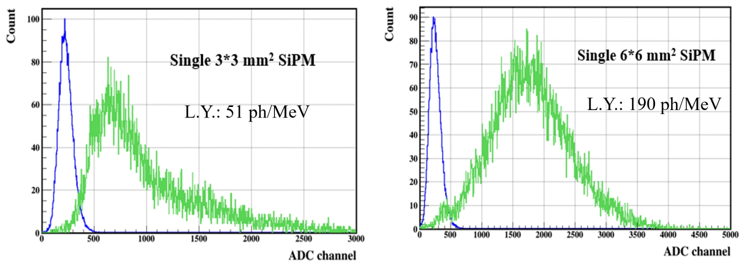

Figure 1.50: A real GS+SiPMs cell test results. Effective light yield with a 3×3 mm^2 SiPM (left) and a 6×6 mm^2 SiPM (right).

Both ESR and Teflon reflective films were tested, and Teflon film was used for further tests due to its higher reflectivity in UV range. The GS cell sample test results are shown in Figure 1.50, in which the effective light yield measured by both 3×3 mm^2 and 6×6 mm^2 SiPMs are 51 ph/MeV and 190 ph/MeV respectively, the L.Y. ratio equals to the sensitive area ration (9/36). According the spectrum, the background noise (pedestal) can be separated at a reasonable threshold. The cosmic ray test is onging to check the MIP response and threshold. According to the simulation and DCR results above, it is hopefully that the 0.1 MIP threshold can be reached.

1.6 Electronics & DAQ

The main purpose of Hadron calorimeter readout electronics is the charge measurement to determine the energy deposited in the glass scintillator.

The parameters of the Hadron calorimeter readout electronics system are as following,

- Dynamic range of charge measurement: 0.1MIPs (800fC) – 100MIPs (800 pC);
- Charge resolution: 10% at 1 MIP;
- Integral non-linearity (INL): $< 1\%$
- SiPM Terminal Capacitance : $<$100pF;
- Single channel average event rate : 1.5kHz/ch at Higgs;
- Single channel maximum event rate : 42.3kHz at Higgs.

The electronic readout of a hadron calorimeter is structurally similar to that of an electromagnetic calorimeter, mainly consisting of three parts, as shown in Figure 1.51. The front-end measurement section, based on fully self-developed ASICs, is responsible for accurately measuring the charge output from the SiPM and converting this charge into digital information to be sent to the data aggregation and transmission section. The data aggregation and transmission section is responsible for collecting data from front-end ASIC and converting this data into high-speed optical signals, which are sent via optical fiber to the back-end electronics data processing section located in the electronics room. The third part of the hadron calorimeter electronics is the power distribution and management section, which is responsible for converting the power supply for the detector into the operating voltages needed by each chip. The data aggregation and transmission section, data processing section, and power distribution and management section of the hadron calorimeter electronics form the overall common framework of CEPC electronics, with specific details available in the ”Electronics” chapter.

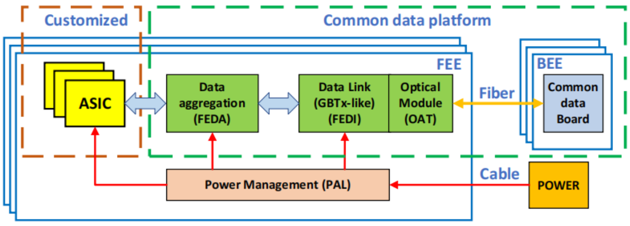

Figure 1.51: Block diagram of the Hadron calorimeter electronics.

1.6.1 Electronics for SiPM

The self-developed ASIC is the core chip of the front-end measurement section, and its performance determines the measurement accuracy of the readout electronics. The requirements for a hadron calorimeter are similar to those of an electromagnetic calorimeter, with a dynamic range that is smaller than that of the electromagnetic calorimeter. The readout electronics for the hadron calorimeter use the same ASIC chips as those used in the readout electronics for the electromagnetic calorimeter. The SiPM readout ASIC (SIPAC) is to be developed in a CMOS technology, and it includes multi channels. As shown in Figure 1.52, each channel has a current buffer, a discriminator, and a time-to-digital (TDC) for the Time-Of-Arrival (TOA) measurement. And for Q measurement, a slow shaper is used, followed by a Switch-Capacitor-Array block. A Wilkinson ADC or Pipeline SAR-ADC is used for sampling. To enable single-photon calibration, a dedicated path for single-photon input is required. Since single-photon signals are extremely small, the frontend employs a low-noise charge-sensitive-amplifier (CSA) for charge signal integration and amplification. The detailed design of the SiPM ASIC (SIPAC) can be found in the ”Electronics” chapter.

1.6.2 Readout Electronics

The barrel part of the hadron calorimeter is divided into 16 sections along the phi direction, with a length of 6460 mm in the z direction. Each section is further divided into 10 equal parts along the z direction, with each part measuring

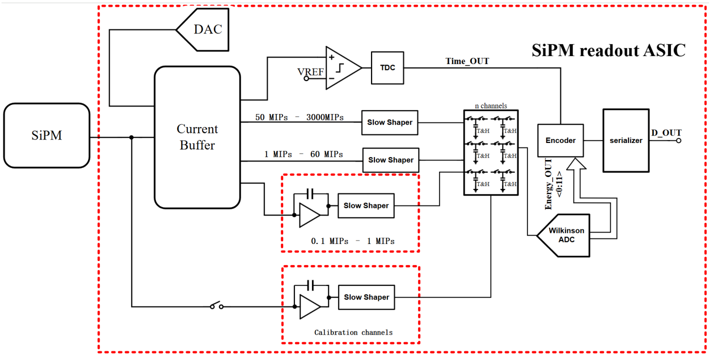

Figure 1.52: Block diagram of the SiPM ASIC (SIPAC) design.

646 mm in length, making each part a basic module of the hadron calorimeter electronics. Since the hadron calorimeter has a total of 48 layers, this results in each module having different dimensions in the phi direction across the layers. Depending on the specific dimensions of each layer, 3 to 4 front-end electronic boards are used to measure the signals from the corresponding SiPMs. The electronic layout for one layer is shown in Figure 1.53. Due to the large number of layers in the hadron calorimeter, and in order to reduce its volume and weight, the design aims for compactness. The height of the space occupied by the electronics is 3.2 mm, with a PCB thickness of 1.2 mm and an ASIC chip height of 2 mm.

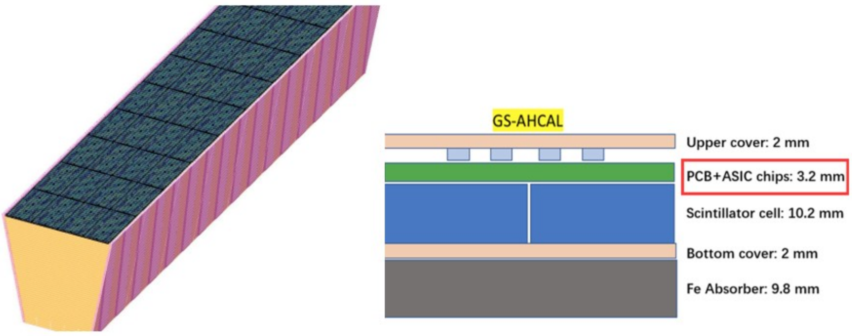

Figure 1.53: Schematic diagram of the electronic unit module.

The digital information outputted by the ASIC on each FEE board is sent to the data aggregation and transmission board located at the edge of the barrel section through a data aggregation chip (FEDA). The barrel section is divided into 10 modules along the z direction. Data from 5 modules at one end is sent to the corresponding data aggregation and transmission board at the edge of that end of the barrel. Similarly, data from the other 5 modules is sent to the data aggregation and transmission board at the opposite end. Each data aggregation and transmission board converts the aggregated data into optical signals with ASICs (FEDI and OAT), which are then transmitted via optical fibers to the back-end electronics board located outside the detector. Each data aggregation and transmission board is also responsible for converting the external supply voltage into the operational voltage required by the ASIC, and for delivering this operational voltage to each front-end electronics board. The layout of the electronics is illustrated in the Figure 1.54.

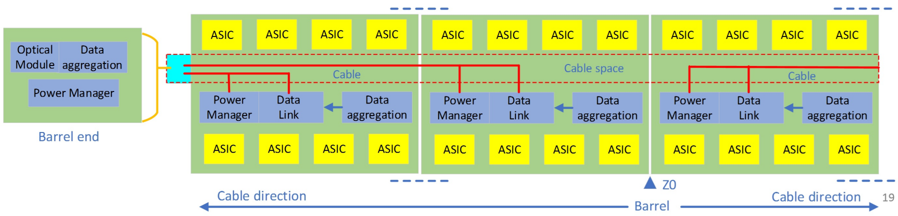

Figure 1.54: The layout of the electronics.

The end cap of the hadron calorimeter also adopts a modular design. Although the size and shape of the end cap modules differ from those of the barrel modules, the arrangement of the front-end is the same as that in the barrel section.

The detailed design of the ASIC (SIPAC, FEDA, FEDI, OAT,) can be found in the ”Electronics” chapter.

1.7 Mechanics

1.7.1 Barrel part

1.7.1.1 Overview and requirements of barrel HCAL

Barrel HCAL is located between magnet and barrel ECAL, which has been shown in Figure 1.55 with purple color and a red box. The gap between barrel HCAL and end-cap HCAL is 30mm. Barrel HCAL will be held by two auxiliary rings on both ends. And the auxiliary rings will be fixed with barrel Yoke.

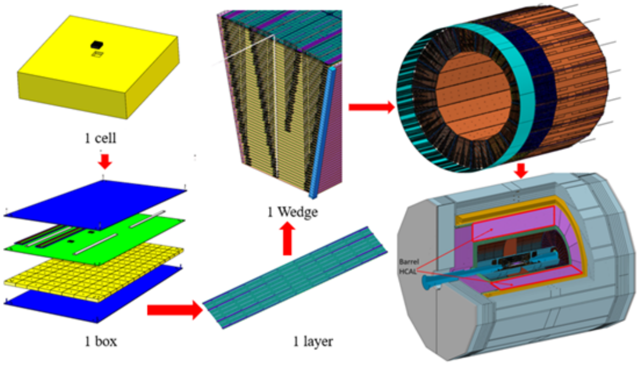

Figure 1.55: Components and location of barrel HCAL.

The contour dimension of barrel HCAL has been shown in Figure 1.56. The total length is 6460 mm except the edge sealings which located in the gap between barrel HCAL and end-cap HCAL. The cross section of barrel HCAL is a regular hendecagon which means barrel HCAL is composed by 16 wedges. The outer hendecagon inscribed circle diameter is 6910 mm and the inner hendecagon inscribed circle diameter is 4280 mm.

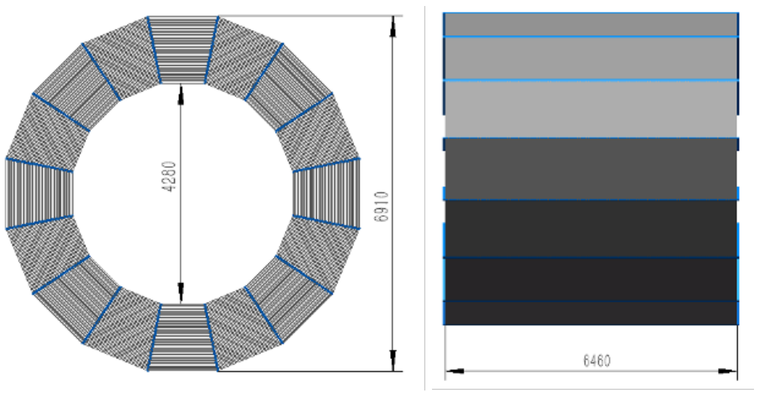

Figure 1.56: Contour dimension of barrel HCAL

The requirements for structure are listed here:

1. The support structure zone is as low as possible.
2. The maximum stress of different materials need to be lower than their allowable stress level.
3. The deformation of different materials need to be controlled so that there will be no broken parts under different conditions.
4. Outer contour dimension tolerance need to be 0 mm to -5 mm and inner contour dimension tolerance need to be 0 mm to +5 mm.

1.7.1.2 Structure design

1.7.1.2.1 General structure Barrel HCAL consists of 16 wedges, the dimension of each wedge is shown in Figure 1.57. Each wedge consists of 48 layers of detect module. The cross-section structure of each layer of detect module is shown in Figure 1.58.

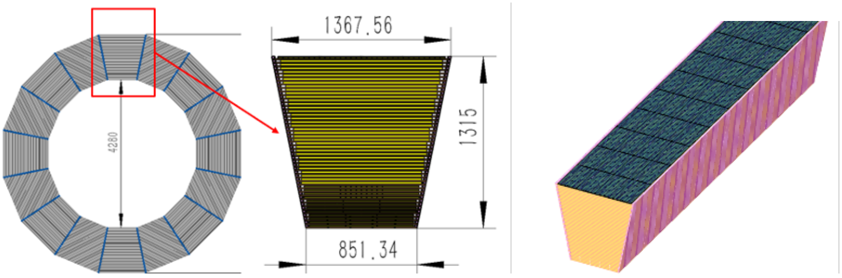

Figure 1.57: Structure of each wedge

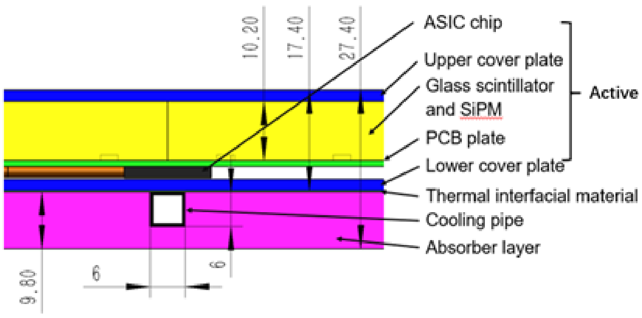

Figure 1.58: Cross section structure of each layer of detect module

For each layer of detector module, generally it is composed of one absorber layer and one active layer. But the active layer actually is composed of several active boxes. There are three kinds of the boxes, the difference between them is their width. The boxes dimension and more details can be seen in Figure 1.59.

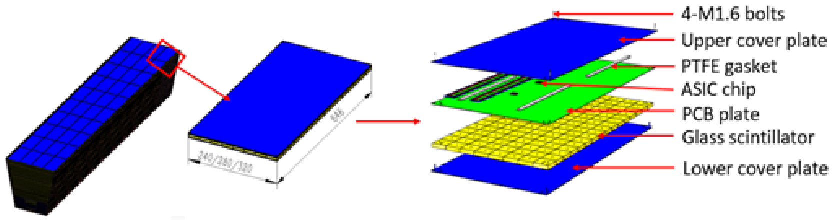

Figure 1.59: Boxes dimension and more structure details

Each boxes contains about 128/112/96 cells, cell structure is shown in Figure 1.60. It consists of one 40mm$\times$40mm$\times$10mm glass scintillator and one 3mm*3mm SiPM.

For barrel HCAL, there are totally 200800 cells for each wedge, so the amount of the cell for barrel HCAL is 3212800. The boxes amount for each wedge is 1740, for the whole barrel HCAL, the amount is 27840. Table 1.12 lists the weight data. The total weight is about 955 tons.

1.7.1.2.2 Connection structure For each box, the SiPM, ASIC chip and PCB can be regarded as one part. Then a lot of glass scintillators are glued with PCB plate. At 4 corners of the upper cover plate, there are 4 counterbores. At 4 corners of lower cover plate, there are 4 inside thread pipe. For the 4 corner glass scintillators, there is one corresponding drilled hole for each one. Cover plate and other components will be fixed together by 4 M1.6 bolts. The box connection structure is shown in Figure 1.61.

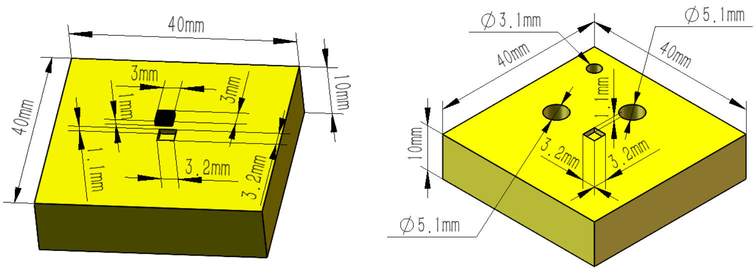

Figure 1.60: Structure of one cell (left is normal cell, right is corner cell)

Table 1.12: Weight data of different components of barrel HCAL.

Items	Weight/wedge (kg)	Weight/barrel (T)
Cover plate	10287	164.6
PCB plate	390	6.2
GS scintillator	19277	308.4
Absorber layer	27515	440.2
Support structure	1883	30.1
Auxiliaries	350	5.6
Total	59702	955.2

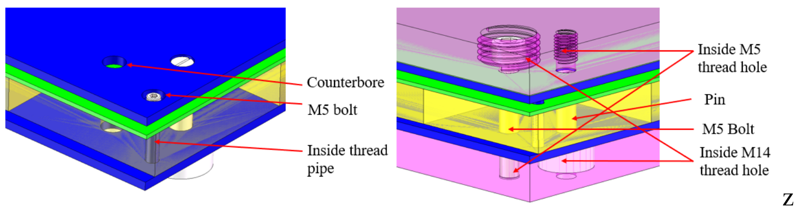

Figure 1.61: Boxes connection structure and boxes connects with absorber structure

Each box also needs to be fixed with absorber layer during assembling process. From the right picture of Figure 1.61, it can be found there is a M5 bolt which can connect the upper absorber layer, the active layer and the lower absorber layer.

The PTFE gasket in Figure 1.59 and thermal interfacial material in Figure 1.58. can be played as buffer layer during assembling procedure.

Between upper and lower absorber layers, there are two support trapezoidal beams. The detailed structure can be seen in Figure 1.62.

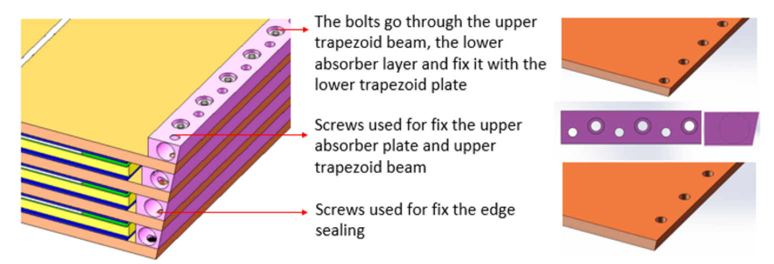

Figure 1.62: Connection between two absorber layers

After assembling layer by layer, one wedge will be finished. For the connection between two wedges, the detailed structure can be seen in Figure 1.63. They are called edge sealings. There are a lot of counterbores use to connect with trapezoidal beams by M8 bolts and M5 bolts are used for connecting edge sealings with absorber layer.

1.7.1.2.3 Interface structure Barrel HCAL will connect with barrel Yoke by two auxiliary rings. The connection structure can be seen in Figure 1.64. The rings will be fixed with barrel HCAL by edge sealings. Barrel HCAL will

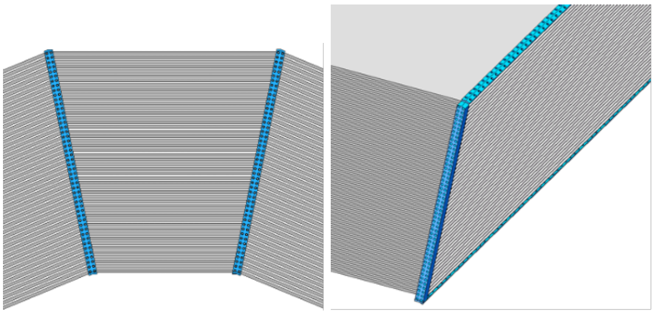

Figure 1.63: Connection structure between wedges

connect with barrel ECAL by edge sealings too. Figure 1.65 shows the connection structure between barrel HCAL and barrel ECAL.

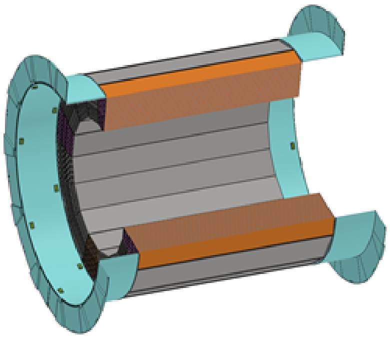

Figure 1.64: Connection structure between barrel HCAL and barrel Yoke

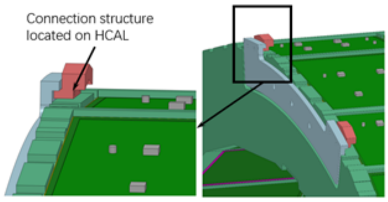

Figure 1.65: Connection structure between barrel HCAL and barrel ECAL

1.7.1.3 Finite element analysis result

Here we mainly concern about several assembling processes and final running condition.

1.7.1.3.1 One wedge assembling condition FEA result

If all the details are input as a model, the mesh quantities will be very huge. So in order to meet the analysis ability of computer, a simplified model has been used. This model just concerns the absorber and support structure. The active layers are just regarded as weight load which is loaded by absorber. Absorber layers are surface element, connection bolts are beam element, others are solid element. During one wedge assembling condition. We assume this process occurred on a platform. So a fix boundary condition is applied on the lowest absorber layer. Figure 1.66 shows the deformation and stress distribution. The maximum deformation is about 0.33mm, the maximum stress is 24.7MPa.

1.7.1.3.2 16 wedges assembling condition FEA result

16 wedges assembling process is shown in Figure 1.67 Two end support ring with support tooling are placed on platform firstly. Then 16 wedges of barrel HCAL are placed and fixed one by one.

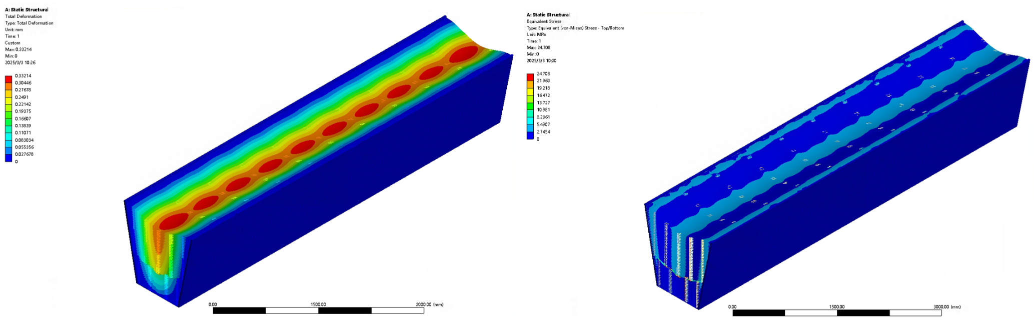

Figure 1.66: Deformation and stress distribution of one wedge

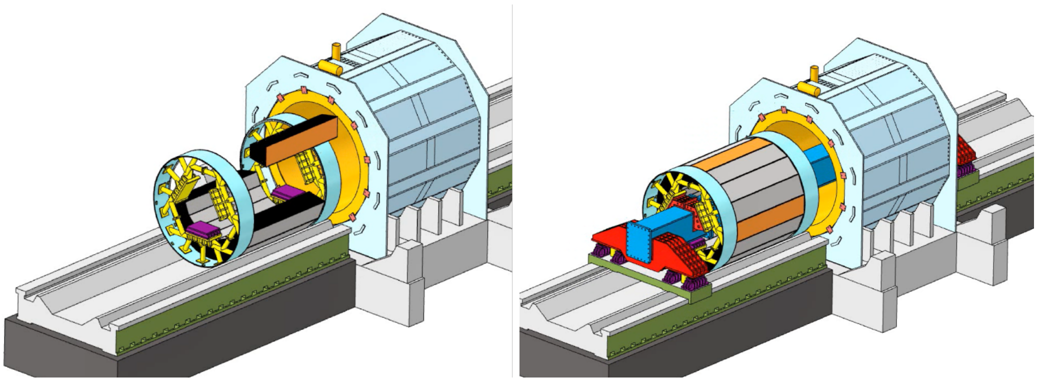

Figure 1.67: 16 wedges assembling process

The FEA model concerns the absorber layers, trapezoid beam support structure and two support rings. The active layers are just regarded as weight load which is loaded by absorber, so one mass point is established to replace all active layers. Absorber layers are surface element, connection bolts are beam element, others are solid element. During 16 wedges assembling condition it is assumed that the inner surfaces of two end support rings are undeformed, so a fix boundary was applied on these two surfaces. Figure 1.68 shows the deformation and stress distribution. The maximum deformation is about 0.66mm, and the maximum stress is 190MPa. The maximum stress is higher than the allowable stress of stainless steel but lower than its yield strength. Because it is just a very small region it can also meet the requirement.

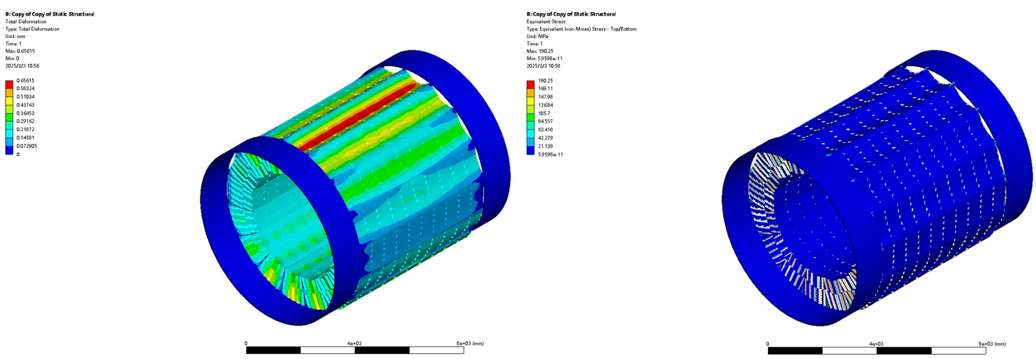

Figure 1.68: Deformation and stress distribution of berral HCAL

1.7.1.3.3 Barrel ECAL connection condition FEA result

Barrel ECAL will be supported by barrel HCAL, so the final running condition need to concern about the load of barrel ECAL on barrel HCAL. Figure 1.69 is the final situation which means barrel HCAL has connected with barrel ECAL.

The FEA model concerns the absorber layers, trapezoidal beam support structure and two supporting rings. The active layers are just regarded as weight load which is loaded by absorber, so another mass point is established to replace

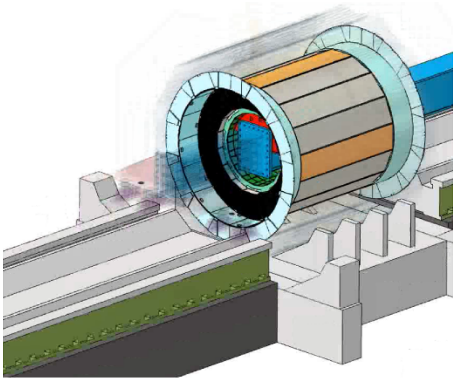

Figure 1.69: Barrel HCAL connects with barrel ECAL

all active layers. The barrel ECAL is also regarded as weight load, so the second mass point is established to replace 135 tons weight of barrel ECAL. This weight will load on a small region of edge sealing. Absorber layers are surface element, connection bolts are beam element, others are solid element. The outermost surfaces of two end support rings are assumed undeformed, so a fixed boundary was applied on these two surfaces.

Figure 1.70 shows the boundary condition and deformation distribution. The maximum deformation is about 1.26mm. Figure 1.71 shows the stress distribution under this condition. The maximum stress is 371.1MPa occurred at the connection between barrel HCAL and end support ring. As for the high stress region, we will replace several trapezoid beams made of stainless steel with titanium alloy (TC4 whose yield stress is higher than 825MPa).

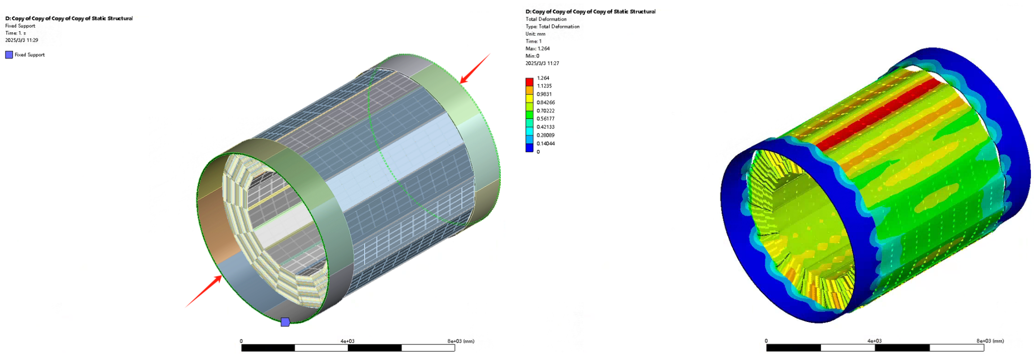

Figure 1.70: Boundary condition and deformation of HCAL with ECAL

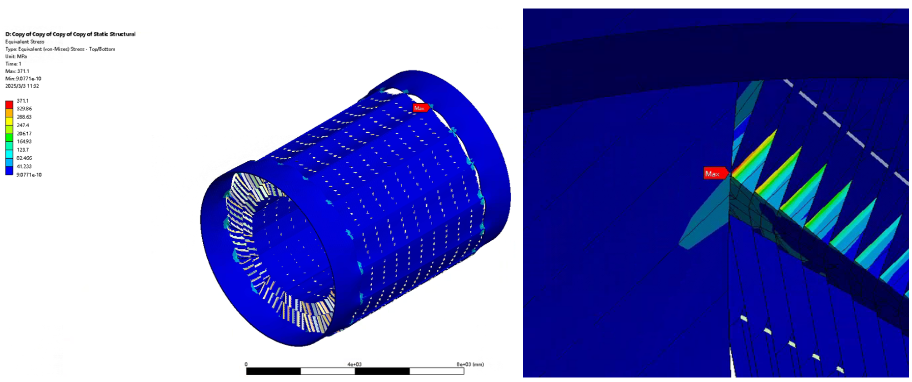

Figure 1.71: Stress distribution and maximum stress position

The gap dimension will change when it bears the gravity. It is necessary to know how much the gap dimension changes and whether it will have some influence on active layer. Figure 1.72 shows the deformation of all 48 layers at the same X. It can be concluded that the deformation difference between 48 layer is lower than 0.2mm. Which means if the buffer layer (gasket and thermal interfacial material) can absorb deformation of 0.2mm , our structure will be safe. The total thickness of gasket and thermal interfacial material is 2.4mm. So it is feasible for them to deform by about 8.3% (0.2/2.4)

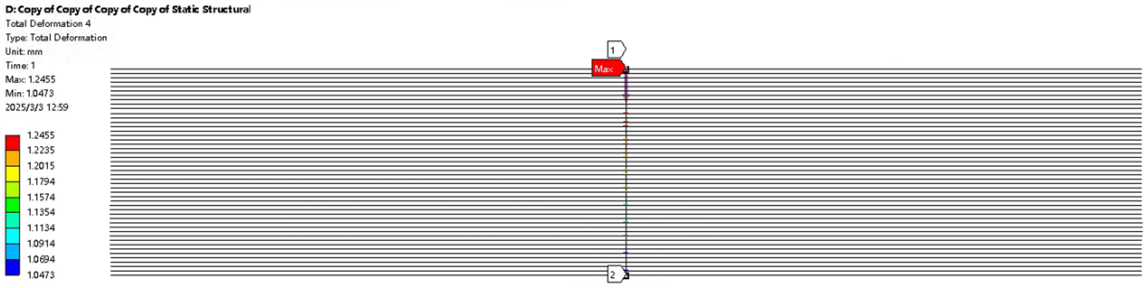

Figure 1.72: The deformation of all 48 layers at the same X

The deformation within one layer can be seen in Figure 1.73. The result shows deformation difference within 1 layer is lower than 0.5mm. Based on this we need to know when the box is bended and the difference between the lowest point and highest point is 0.5mm, whether the glass scintillator will be broken.

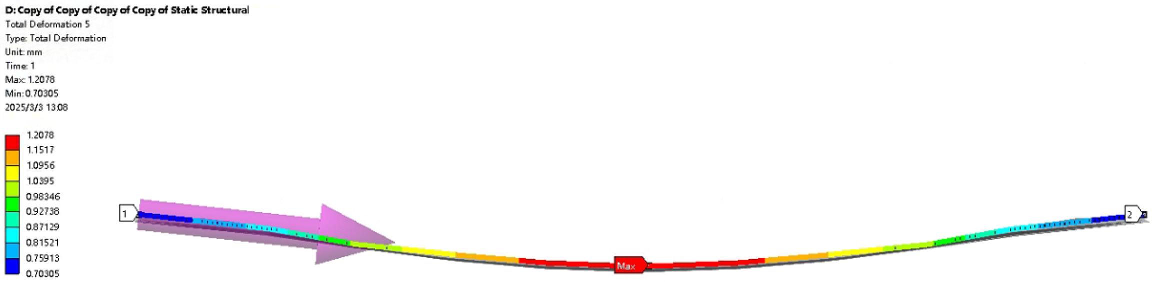

Figure 1.73: Deformation within one layer

From the above results, we can conclude that it can meet the requirements for structure.

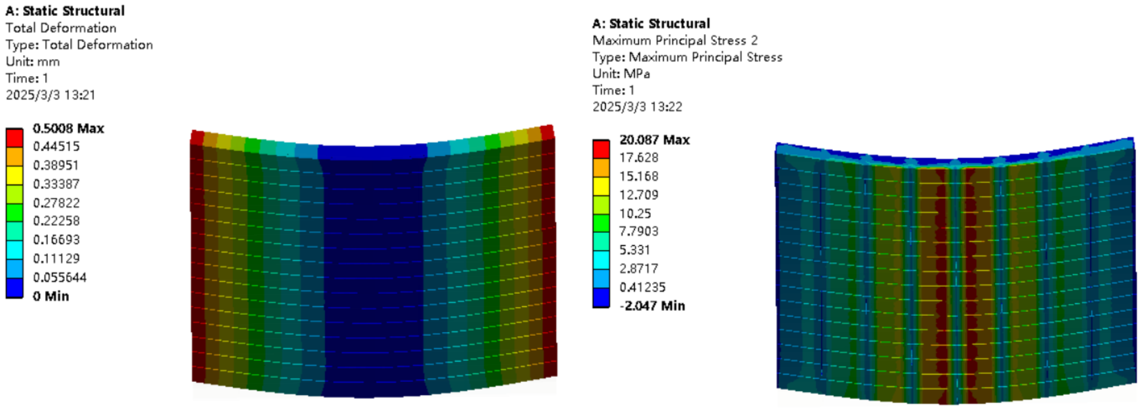

Figure 1.74: When the difference between the lowest point and highest point is 0.5mm (left), the stress distribution (right)

1.7.1.3.4 Box FEA result Figure 1.74. shows the stress to answer the question that when the box is bended and the difference between the lowest point and highest point is 0.5mm whether the glass scintillator will be broken. It can be seen the maximum principal stress is about 20MPa which is lower than its allowable stress 60MPa. So the absorber deformation is acceptable.

Moving condition by manpower also has been studied. Figure 1.75. shows the result. Both of the deformation and stress can meet our requirement.

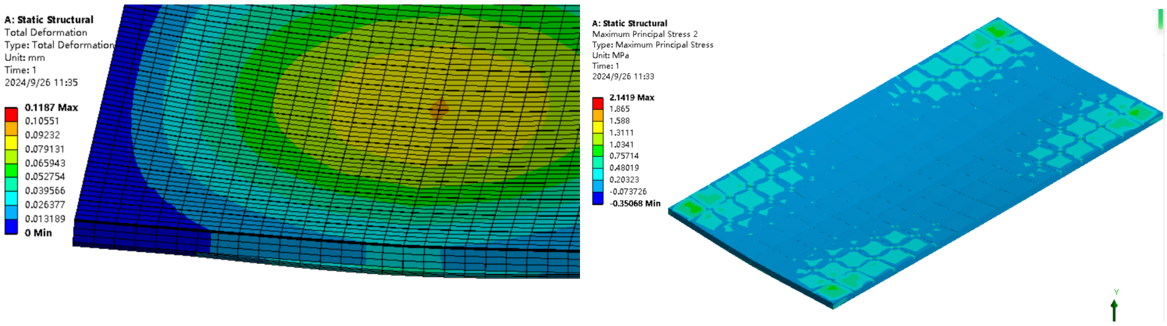

Figure 1.75: Moving condition result

1.7.1.4 Cables routing scheme

Cables are collected in the box, which are located between upper cover plate and PCB plate and the structure can be seen in Figure 1.59. Each box contains 5 cables, and the diameter of each cable is 2 mm. The length of the cables in one box is the same, but the lengths of the cables vary for different boxes. There are five different lengths, 0.40 m, 1.05 m, 1.70 m, 2.35 m, 2.90 m.

The boxes installation sequence is shown in Figure 1.76. There are 4 regions and we can install and route out cables in parallel for these 4 regions. For each region the box installation sequence is from 1-1 to 1-10. Figure 1.77 shows how to install the first box and the second box within one layer. First, positioning the 1st box, then opening the upper cover plate, then making the cables straight, then postioning the 2nd box and repeat the steps. The box will be installed one by one with the same procedure.

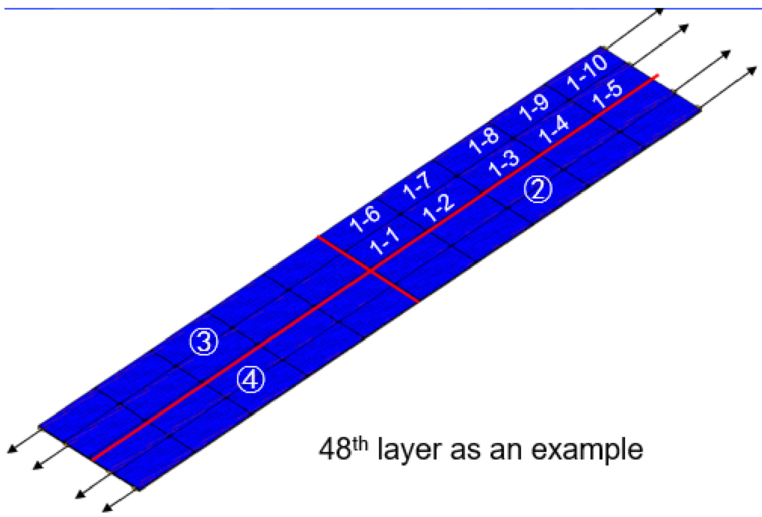

Figure 1.76: Installation sequence of boxes in one layer.

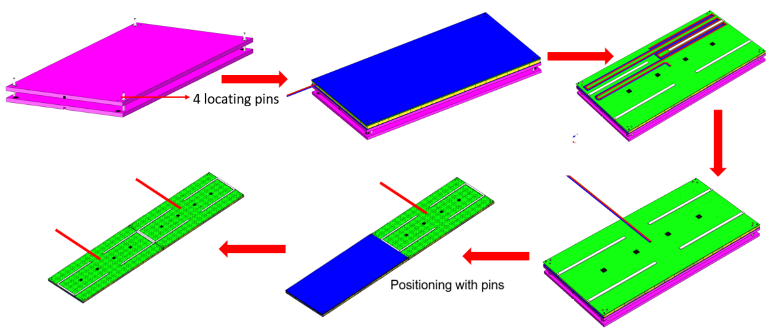

Figure 1.77: Installation procedure from 1st box to 2nd box.

After all the boxes within one layer being installed, the cables need to be bent and routed to the end administration board and the final structure can be seen in Figure 1.78. There are 2*4 or 2*3 administration boards for each layer, each boards is 20mm*60mm. The input of one board is 25 cables and output of one board is 2 cables and one fiber.

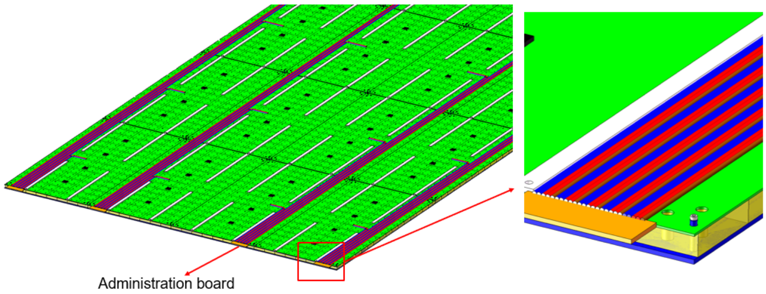

Figure 1.78: Final structure of all boxes within one layer.

Table 1.13 shows the quantities and area of the cables. For each boxes there are 4 cables. And the diameter of each cable is 2 mm. The cables of different boxes are separated and they will not be connected to the neighbouring boxes. The front and back cable routing scheme is shown in Figure 1.79.

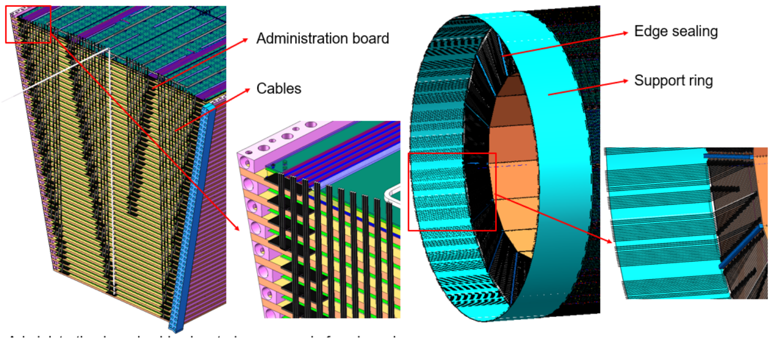

Figure 1.79: The front and back cable routing scheme.

Table 1.13: The quantities and area of the cables for each wedge.

	Element quantities/wedge	**cable quantities at each end/ wedge**	**cable area/ mm^2**
1st - 18th layer	30/layer	60/layer	188.4/layer
19th - 48th layer	40/layer	60/layer	251.2/layer
Total	1740	3480	10927.2

1.7.2 Mechanics of the endcaps

To meet the requirements for the next-generation high-energy circular electron-positron collider experiment in the precise measurement of hadron jets, this project focuses on developing imaging hadron calorimeter technology using glass scintillators coupled with SiPMs as sensitive units and verifying the technology through prototype construction. The performance is expected to meet the requirements for precise particle flow reconstruction.

The imaging hadron calorimeter based on glass scintillators coupled with SiPMs belongs to the analog readout type. Compared to digital readout hadron calorimeters, it offers advantages such as a wide dynamic range, excellent linear response, ease of calibration, low operational costs, and high reliability. With the continuous advancement of SiPM technology, the technical advantages of this calorimeter design have become increasingly pronounced.

The calorimeter employs glass scintillators as the scintillation material, which has a higher density than the scintillators used in similar international detectors. Consequently, the calorimeter unit requires a high-performance active layer design to achieve robust structural and mechanical performance for the detector units within limited space and metal thickness constraints. Fig. 1.80 shows overall dimensions of the endcap HCAL. The endcap HCAL is designed for the readout calorimeter at the detector's endcap and is a critical component of the overall calorimeter system.

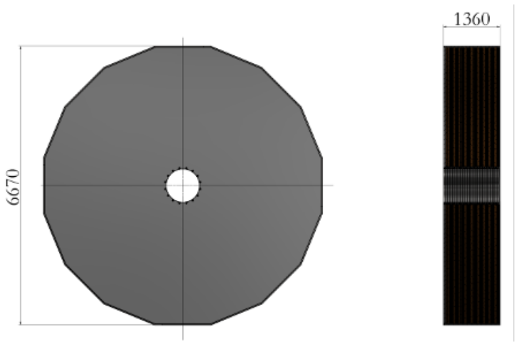

Figure 1.80: Overall dimensions of the endcap HCAL

1.7.2.1 Overall structure

The endcap HCAL adopts a structural rigid frame composed of stainless steel absorbers. The active layers of the detection elements are alternately installed within the absorbers, with a total of 48 acitive layers on one side. The alternately stacked endcap HCAL forms the entire detector. The total weight is approximately 362 tons, with the active layers weighing around 199 tons and the absorbers weighing about 158 tons. Fig. 1.81 shows the formation of the endcap HCAL model. The absorber frame supports the weight of all the detector components.

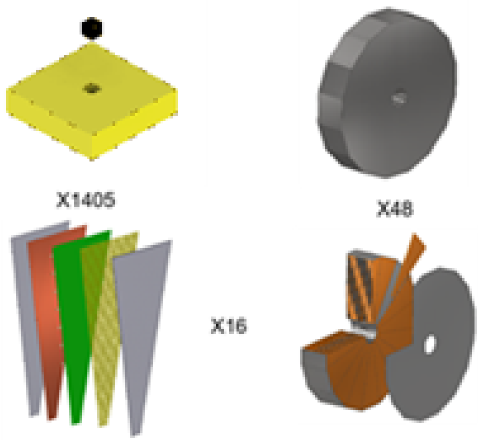

Figure 1.81: Formation of the endcap HCAL model

Assembly process of the endcap HCAL: The endcap HCAL adopts a horizontal installation scheme. First, the outermost structural plate with a thickness of 50 mm is installed. This structural plate does not serve as an absorber but is added to enhance the overall structural rigidity. Using this base plate as the installation reference, 48 active layers and 48 absorber layers are installed. After horizontal installation of the absorbers, specialized tools are used to transition the horizontally placed components into a vertical position. During this process, it is crucial to ensure that the crystals are not subjected to excessive pressure to guarantee their safety.

1.7.2.2 Active layer structure

The HCAL active layer consists of a glass scintillator layer, PCB circuit board, and upper and lower cover plates. Fig. 1.82 shows the horizontal installation scheme and gapless glass tile arrangement. The glass scintillator used in the acitive layer is relatively fragile, so care must be taken to prevent the glass scintillator from being compressed during the implementation of the sensitive layer. By optimizing the rib structure and dimensional design of the cover plates, minimal

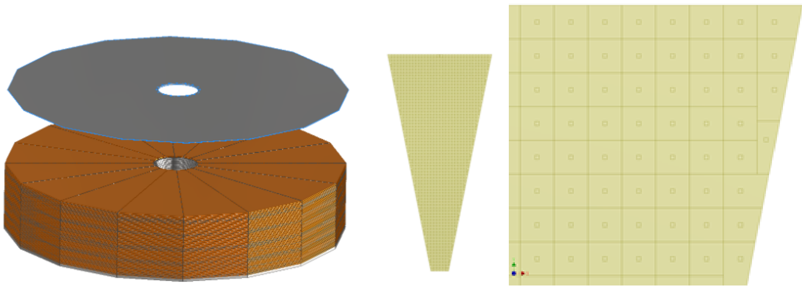

Figure 1.82: Horizontal installation scheme and gapless glass tile arrangement.

deformation was achieved during the packaging of the active layer. The deformation is controlled to be less than the gap of the cover plates, ensuring the safety of the glass scintillator.

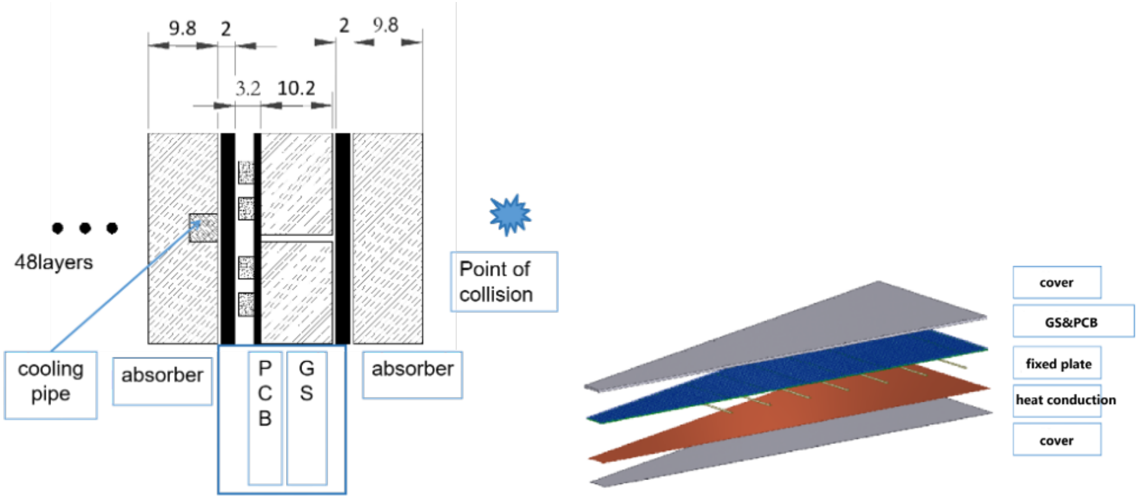

Figure 1.83: Principle diagram of the active layer, for one cell (left) and one sector (right).

The basic dimensions of the glass scintillator are 40×40 mm, with each glass piece having one SiPM. At the edges, there are four types of irregular structures. Every five rows of glass scintillators form a cycle, with four identical irregular structures. Fig. 1.83 shows the principle diagram of the active layer, for one cell (left) and one sector (right). The crystal arrangement adopts a gapless layout, and trapezoidal structures are used for the glass at the edges to achieve this.

The structural module was simulated using ANSYS to calculate the overall mechanical strength and stiffness of the GS detection layer. The simulation considered the most critical conditions during the module installation process, specifically when the module is placed horizontally and supported at both ends during transportation. Under these conditions, the module experiences maximum gravitational force, and the stress on the glass scintillator determines the safety of the entire module. The Fig. 1.84 show that the maximum stress on the glass scintillator is 37 MPa, while the maximum allowable stress for the glass scintillator is 60 MPa. Therefore, the detector module is deemed safe.

1.7.3 Cooling system

1.7.3.1 Cooling scheme

Currently, the mainstream solutions for heat dissipation in electronic devices primarily include natural convection, air cooling, and liquid cooling. Natural convection utilizes the flow caused by the uneven temperature field of the fluid involved in heat exchange to remove the heat generated by the device. However, current device structures are compact, with only millimeter-level gaps between layers. Equation (1) is the calculation formula of the natural convection heat transfer coefficient in confined spaces. Based on the structural parameters of the model and the established boundary conditions, natural convection heat transfer within the interlayer is negligible due to the Grashof number (Gr) being less than 10^4. Consequently, heat dissipation primarily relies on thermal conduction through the interlayer gaps.

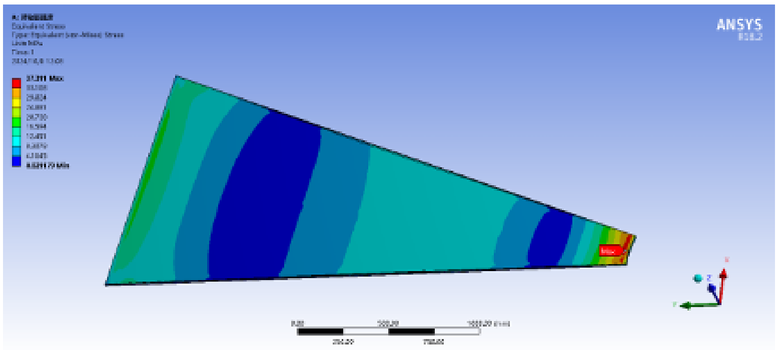

Figure 1.84: Simulation of Mechanical Stiffness and Safety of the Module Electronic cable structure

$$Gr = \frac{g\beta(t_{w1} - t_{w2})\delta^3}{v^2}$$

Among them, g represents the gravitational acceleration, β represents the volumetric thermal expansion coefficient, t_w corresponds to the wall temperature, δ signifies the thickness of the sandwich layer, v stands for the kinematic viscosity. Furthermore, air cooling predominantly utilizes flowing air as the thermal transfer medium to dissipate heat. However, the narrow inter layer gaps result in significant airflow resistance and poor heat dissipation performance. To validate the above analysis, a comprehensive finite element analysis was conducted to simulate both natural convection and forced air-cooling performance. Figure 1.85 shows the thermal performance of natural convection. The maximum temperature of the chip is approximately 40°C, thereby demonstrating relatively poor heat dissipation performance. In addition, the temperature uniformity is also unsatisfied, with a temperature variation of 3.5°Cwithin a single module.

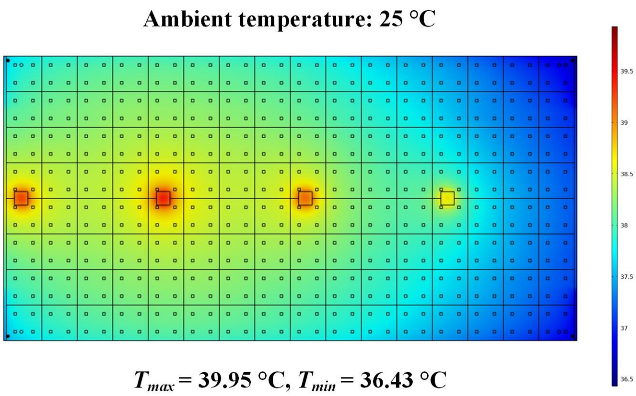

Figure 1.85: Thermal performance of natural convection.

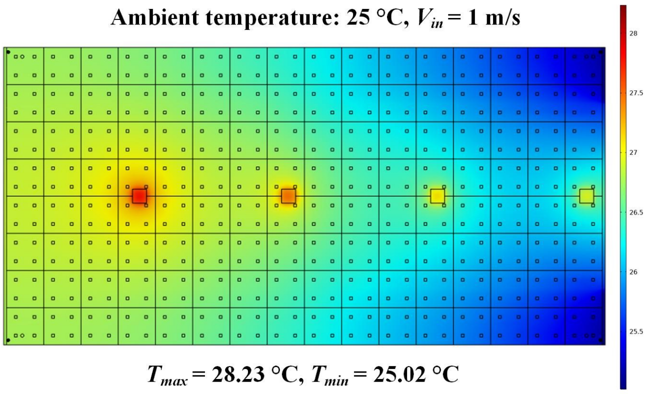

Figure 1.86: Thermal performance of air-cooling.

Figure 1.86 illustrates the temperature distribution under air-cooling conditions. Comparative analysis reveals that air cooling significantly reduces the chip's operating temperature compared to natural convection cooling. Theoretically, the chip temperature shows a continuous decrease trend with increasing inlet air velocity. However, simulation results did not reveal significant variation trend, which is attributed to the substantial air resistance in confined spaces, resulting in limited cooling performance. The simulation results demonstrate that the temperature difference within a single module is approximately 2℃when using air cooling.

Table 1.14: Chip temperature variation with inlet velocity.

Inlet velocity (m/s)	T_{max} (℃)	T_{min} (℃)
1	28.23	25.02
2	27.36	25.00
3	27.07	25.00
4	26.91	25.00
5	26.82	25.00

In summary, the excessively narrow interlayer gaps significantly reduce the efficiency of natural convection and air cooling, thereby failing to address the thermal management demands. As a result, it is imperative to adopt liquid cooling technology to ensure efficient heat dissipation and temperature uniformity.

1.7.3.2 FEA simulation

1.7.3.2.1 Thermal simulation Figure 1.88 shows the temperature distribution of the HCAL through liquid cooling Based on the analysis, liquid cooling technology has been adopted in this study to achieve efficient thermal management of HCAL. Figure 1.87 shows the schematic diagram of the proposed cooling structure, the inlet temperature is 15℃with a flow rate of 0.005 kg/s (corresponding to an inlet velocity of 0.1 m/s). As depicted in Figure 1.88, the implementation of liquid cooling technology has significantly improved the thermal management performance of the chips, effectively maintaining the temperature rise below 0.6 ℃. Furthermore, the system exhibits outstanding thermal uniformity, with the maximum temperature variations of chips under the same modules were under 0.1℃. Therefore, the liquid cooling technology can effectively meet the thermal dissipation requirements of HCAL.

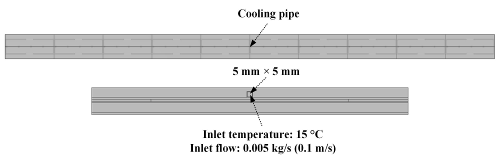

Figure 1.87: Schematic diagram of the proposed cooling structure

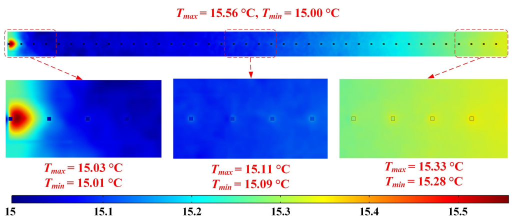

Figure 1.88: Temperature distribution of the HCAL through liquid cooling.

1.7.3.2.2 Flow simulation Due to the complexity of the system structure and the significant flow resistance caused by the multi-layer configuration, liquid cooling technology still faces substantial challenges in terms of flow characteristics.

Therefore, it is crucial to undertake a comprehensive analysis of the system's flow properties. To reduce system complexity, a multi-layer design with a shared inlet and outlet was employed, as shown in Figure 1.89, where the inlet flow rate is set at 0.435 kg/s, corresponding to a flow velocity of 0.1 m/s in each chip's pipeline. Figure 1.90 illustrates the flow velocity distribution across different layers, revealing noticeable disparities in flow rates between layers. Specifically, the inter-layer flow is substantial in the initial layers but drops sharply after the 5th layer, with almost no fluid passing through beyond the 10th layer. This phenomenon is primarily attributed to the complexity of the pipeline structure, which results in excessive flow resistance, making it difficult for fluid to effectively reach the lower layers. Consequently, it is imperative to optimize the pipeline design to ensure the cooling performance.

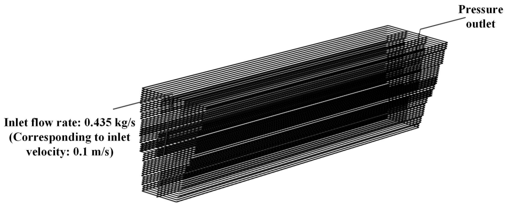

Figure 1.89: Multi-layer design of flow pipe with a shared inlet and outlet.

To reduce the flow resistance in the pipeline, we implemented both four-in-one and eight-in-one pipeline structural designs and analyzed their flow characteristics, as illustrated in Figure 1.91 and Figure 1.92. The results demonstrate that both designs achieve a uniform flow velocity distribution across different layers, effectively meeting the flow rate requirements for heat dissipation.

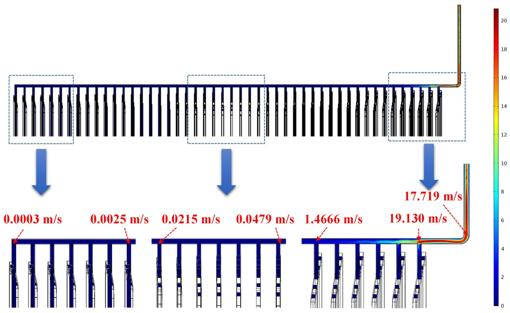

Figure 1.90: Flow velocity distribution across different layers.

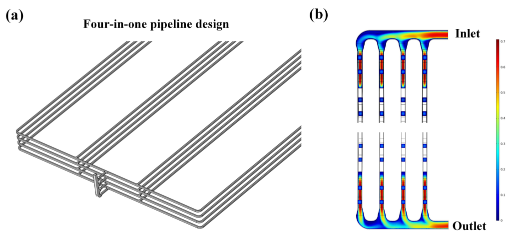

Figure 1.91: (a) Four-in-one design of flow pipe, (b) Flow velocity distribution across different layers.

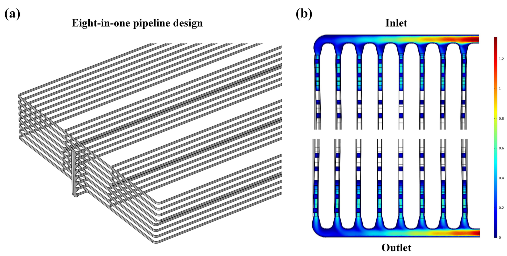

Figure 1.92: (a) Four-in-one design of flow pipe, (b) Flow velocity distribution across different layers.

In summary, liquid cooling technology is utilized for the thermal management of the HCAL system, and an eight-in-one pipeline structure has been designed to meet the flow requirements for barrel HCAL. For end HCAL, the scheme is five-in-one pipeline structure which is less than barrel HCAL. For each layer, the total length is less than barrel HCAL, either. So it can be forecast that if the end HCAL use the same cooling system, it can also meet our requirement. The results demonstrate that the temperature rise and uniformity of the chips can be maintained within 1.0℃with a flow velocity of 0.1 m/s in each chip's pipeline, effectively satisfying the cooling requirements.

1.7.3.3 Cooling structure of Barrel

For cooling, water cooling structure is chosen. It can be seen from Figure 1.58 that cooling pipe is located within absorber layer. Figure 1.93 shows the cooling routing schematic diagram for each wedge. More cooling structure for barrel HCAL can be seen in Figure 1.94.

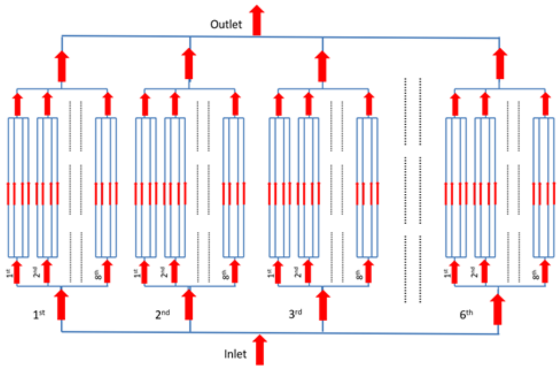

Figure 1.93: Cooling routing for each wedge

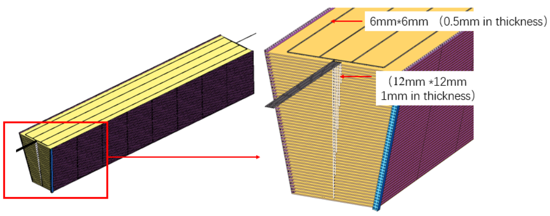

Figure 1.94: Cooling pipe structure for each wedge

1.7.3.4 Cooling structure of endcap

For the water-cooling structure of the end HCAL, as shown in the Figure 1.95, each detector layer is divided into 16 detector regions, with each region having one cooling water channel, resulting in 16 directional water-cooling channels. After the 48 detector layers are assembled together, the water channels in the same direction are connected in parallel to form a single water channel. The water pipes in the detector are arranged in a 4×4 square configuration, with a total of 48 water pipes, each with an inner diameter of 12 mm.

1.8 Calibration

1.8.1 Calibration using physics processes

Isolated hadrons. There are fruitful physics processes that can provide isolated hadrons, e.g. hadronic τ decay in $Z \to \tau^+\tau^-$ or an isolated hadron in a jet. Taking the advantage of the particle flow reconstruction, the energy of these hadrons can be determined by the tracker with high precision. By vetoing the objects have interaction in ECAL, we can

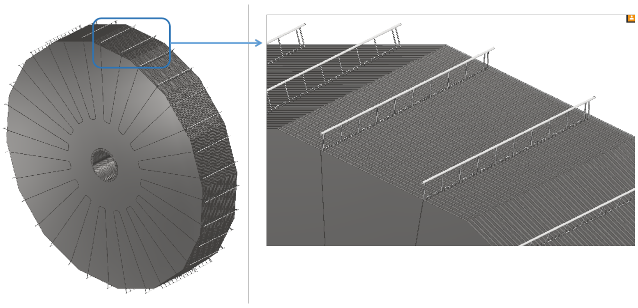

Figure 1.95: Cooling pipe structure for end HCAL

select a pure hadronic shower in HCAL and then fit the E/p to do the calibration. This is suitable for the time-dependent monitoring of HCAL but not the absolute calibration for channels.

Di-muon events $e^+e^- \rightarrow \mu^+\mu^-$. The on-detector calibration of global GS-HCAL can be achieved by the MIP signal generated by prompt muons from collision after the installation, since they loose their energy predominantly by ionization, and their response scales almost linearly with the path length through the cell. These events can be identified with inner trackers and muon chamber, and the momenta of the muons are well measured by tracker. The typical physics process with such highly momentum isolated muons is the $e^+e^- \rightarrow \mu^+\mu^-$. Figure 1.96 shows the kinematic distributions of the muons with $\sqrt{s} = 91$ GeV.

Considering the Z operation mode, the rate of such event is 584 Hz from the cross section and instant luminosity. At minimum we can collect 47 events per hour in a $\Delta\phi \times \Delta cos\theta = 0.018 \times 0.018$ window, corresponding to one $4 \times 4cm^2$ GS cell at the surface of central barrel HCAL. This rate increase rapidly with the $cos\theta$. Taking the advantage of flexible switch of the operating mode between Higgs and Z, we can suppose regular two-week calibration runs in Z mode to collect 4.71×10^8 di-muon events (suppose 16 hours run per day) for HCAL calibration. The precision from statistics is expected to be controlled within 1%.

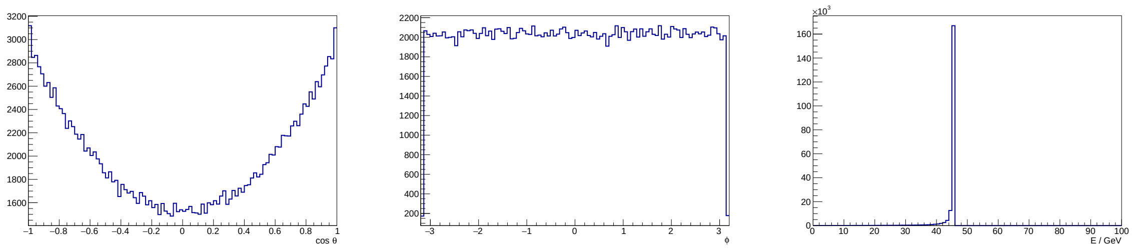

Figure 1.96: Distributions of $cos\theta$ (left), ϕ (middle) and energy (right) for the muon in $e^+e^- \rightarrow \mu^+\mu^-$ process, $\sqrt{s} = 91$ GeV.

Resonant jets $e^+e^- \rightarrow Z \rightarrow q\bar{q}$. The production rate of $e^+e^- \rightarrow Z \rightarrow q\bar{q}$ process is the dominant in Z operation mode. The resonant jets from Z boson can be used to perform a combined calibration for ECAL and HCAL. The total energy $E_{tot} = a \times E_{Ecal} + b \times E_{Hcal}$ should match with the energy of Z boson. This is a good check to monitor the full coverage of the detector by selecting the objects in differential phase spaces.

1.8.2 Hardware calibration

1.8.2.1 System design

HCAL need to run for a long time, and the performance of GS system (glass scintillator and SiPM) might decrease due to long term radiation or aging, which might further decrease the overall precision of HCAL performance. Therefore, a calibration system is required to monitor and test the performance of the GS system, such as pedestal, gain, linearity etc.

The calibration system is mainly based on a LED system, the 2D and 3D schematic diagrams are shown in Figure 1.97. The main concept of the system is as follows: (1) the LED and four SiPMs are placed on the same PCB board, with the LED positioned at the center of the PCB. Five holes to contain the SiPMs and LED are constructed on the back end of the glass scintillator, to render the glass tightly mounted to the PCB board. (2) The LED are powered by a pulsed power, where the voltage and width of the power can be adjusted by the electronics, which is used to control the emitted light intensity of the LED. The photons emitted by the LED will transport through the glass scintillator and can be detected by the SiPMs. (3) By measuring the signals generated by the SiPMs, the system enables the calibration of the glass scintillator light transmittance, and light attenuation coefficient, as well as the linearity and gain of the SiPMs.

The design of arranging the LED in the center of the four SiPMs effectively addresses the issue of reduced readout light caused by the short attenuation length of the glass scintillator. Additionally, it enables the simultaneous calibration and stability testing of multiple SiPMs. And by combining the measurement results from the four SiPMs, the calibration of the glass scintillator's performance becomes more accurate and reliable.

Since the density of the GS is very high, and the manufacture would be very difficult. Therefore, the other GS cell layout is proposed, as shown in Figure 1.97(right), where the SiPM is not placed inside the GS hole, but inside the PCB hole. In this way, GS are kept flat, while holes are opened on the PCB. SiPM are first soldered on a SiPM_PCB, and the SiPM_PCB is connected to the original PCB. For this setup, the calibration scheme will also be modified, with the LED and SiPM being soldered onto the same SiPM_PCB, and the rest are similar.

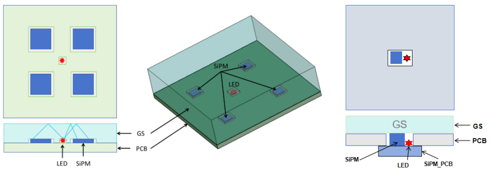

Figure 1.97: Calibration system 2D (left) and 3D (right) schematic diagrams. The blue line in the left figure represents the light emitted by the LED.

1.8.2.2 Electronics and control

This calibration system is distributed into two parts, the front end SiPM board and the bias power control board, as illustrated in Figure 1.98. The LED and SiPMs are mounted on the front end PCB board, where photons can be generated and be detected by the SiPM. The bias power of the LED is supplied by the bias power supply board, which is put on the readout electronics board. During calibration process, repeated calibration pulses are generated with variable voltage and width, which is used to power the LED and generate pulsed photons to calibrate the system. These pulses are also used as trigger of the DAQ system to acquire the signals detected by the SiPM. The calibration procedure is controlled by the DAQ system, to control the generation of bias power with various voltage and width, the signal readout of the SiPM, and the online/offline analysis of these data to calculate the calibration parameters.

Due to fact that the photons will transport and reflect inside the glass scintillator multiple times before they are captured by the SiPM, the system is capable of calibrate the performance of the glass scintillator as well as the SiPM, including the light transmittance and attenuation coefficient of the GS, as well as the PDE and gain of the SiPM. Therefore, the calibration system needs to be further studied to better understand the performance variation of the GS cell after long term operation.

1.9 Performance

1.9.1 GS-AHCAL layout and performance goals

The mechanical structure of the GS-HCAL consists of alternating absorber and scintillator layers arranged in a barrel and endcap configuration, ensuring coverage over the full solid angle. Each active layer is segmented into readout cells to

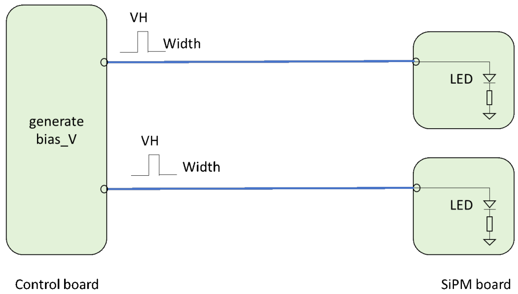

Figure 1.98: Electronics diagram of the GS calibration system, the control board can generate bias pulses with variable voltage and width, which are used to power the LED to generate photons with variable intensity.

achieve fine granularity in hadronic shower reconstruction. Scintillator tiles coupled to silicon photomultipliers (SiPMs) are used as the active medium, offering high photon detection efficiency and a compact readout scheme. This sampling layout is designed to balance material budget, energy measurement accuracy, and the ability to resolve overlapping showers in complex final states.

The principal objective in this chapter is to demonstrate that this calorimeter design meets the core performance requirements of the CEPC physics program. These requirements include achieving the necessary energy resolution for a wide range of hadronic showers, ensuring a linear response over the relevant energy spectrum, and minimizing the impact of beam-induced background on signal reconstruction. Although no prototype data or beam test results are currently available, extensive simulation studies serve to validate that the GS-HCAL design can fulfill these objectives.

In the sections that follow, we first discuss the global performance of the GS-HCAL, presenting energy linearity, resolution, and a detailed treatment of the constant term that appears in the resolution parameterization. We also summarize the results obtained from BMR (Beam Momentum Resolution) studies, highlighting how the detector responds to a variety of incident momenta. Following these global performance considerations, we analyze the simulation of beam-induced backgrounds to show how they affect the calorimeter and to outline the strategies designed to mitigate their influence. Through this simulation-based investigation, we confirm that the GS-HCAL layout and readout scheme can reliably meet the stringent demands of the CEPC environment and physics goals.

1.9.2 Global performance

1.9.2.1 Energy linearity and resolution

The energy linearity and resolution are estimated with Geant4 simulation in CEPCSW. In order to study the intrinsic energy response in GS-HCAL, all inner sub-detectors are removed. A digitization model is constructed considering the following items:

- Birks constant. Currently a preliminary estimation of $C_{Birks} = 0.01$ is applied, considering the BGO has $C_{Birks} = 0.0086$. A measurement with heavy ion beam is being planned.
- Light yield. With the measurement from glass scintillator samples, the intrinsic MIP light yield can reach to $\tilde{2}000$ ph/MeV, thus the detected light yield is expected to be at least 100 p.e./MIP. This satisfies the requirement from noise and 0.1 MIP threshold.
- Attenuation length. 2.3 cm attenuation length is expected, based on current measurements. While more detailed studies of the glass scintillation properties need to be studied.
- Threshold. With the scanned impact on energy resolution, a 0.1 MIP threshold is expected.
- SiPM response.
- Electronic system.
- Other items are considered as negligible after the calibration.

This model gives an estimation of the energy resolution $\sigma_E/E = 29.8\%/\sqrt{E} \oplus 6.5\%$ and linearity within 2% before calibration in Figure 1.99 The physics list '*QGSP-BERT*' is used as default one. Other physics lists are also tested. The large constant term is contributed with the longitudinal leakage from this 6 λ_I design, which is limited by the total detector volume and cost. This result is better than the traditional HCAL with typical energy resolution of $\sigma_E/E = 60\%/\sqrt{E} \oplus 3\%$. In CEPC collision environment more than 95% hadronic objects in the final state would remain in less than 80 GeV as in Figure 1.100. This makes the GS-HCAL has the optimal energy resolution in CEPC interested physics phase space.

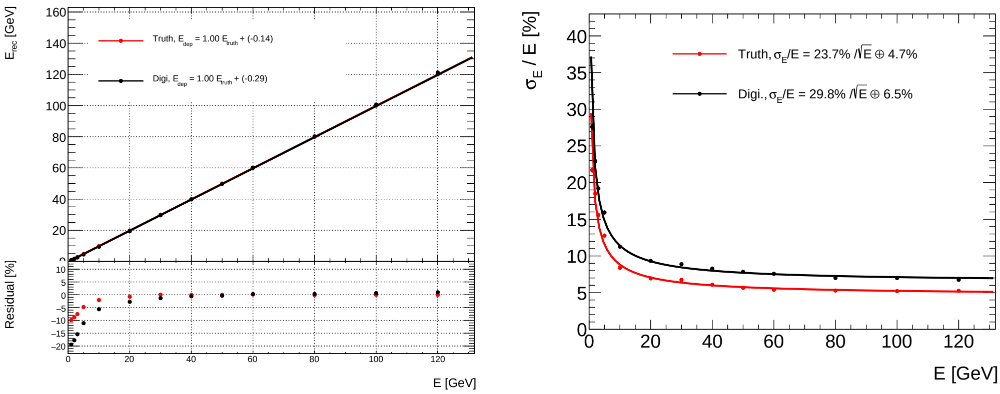

Figure 1.99: Energy linearity and resolution of GS-HCAL with the digitization model.

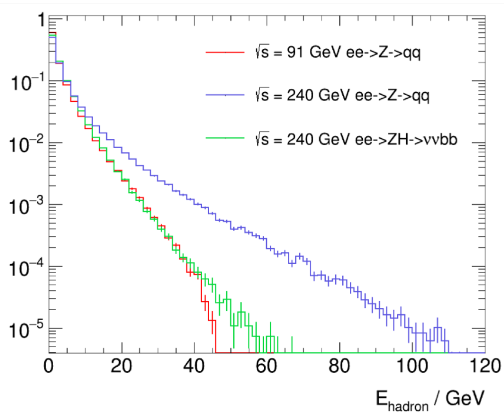

Figure 1.100: Hadronic objects energy distribution in the most energetic processes in e^+e^- collision.

While the current digitization model yields a conservative estimate of 6.5% for the constant term in the energy resolution, it's important to note that several contributing factors can be mitigated through calibration and reconstruction improvements. The preliminary simulation includes unoptimized parameters such as the short light attenuation length and longitudinal leakage effects, which are expected to be partially compensated by future calibration procedures. As the CEPC HCAL R&D progresses, several strategies can be employed to reduce the constant term below 3%. These include developing more sophisticated energy weighting algorithms to account for longitudinal shower development, implementing position-dependent light collection efficiency corrections, and optimizing the calibration with test beam data. Additionally, machine learning techniques could be applied to improve energy reconstruction by correlating shower shapes with true energy deposition. The longitudinal leakage contribution could be further reduced by incorporating information from the tail catcher or using neural networks to estimate missing energy. With these improvements and proper calibration, the constant term is expected to reach the target performance of less than 3% in the final detector implementation.

In the context of hadronic calorimetry, the energy resolution is often characterized by

$$\frac{\sigma_E}{E} = \frac{a}{\sqrt{E}} \oplus b \oplus \frac{c}{E},$$

where a is the stochastic term, b is the constant term, and c is a noise term. A sampling hadronic calorimeter known as GS-HCAL appeared to exhibit a surprisingly large value for b when compared to a similar detector called PS-HCAL. Initially, the difference was viewed with concern, as a large constant term could suggest fundamental issues such as non-uniformities or calibration flaws. However, further investigations pointed toward an alternative explanation: the calorimeter depth in the GS-HCAL simulations was sometimes insufficient to contain hadronic showers, leading to energy leakage that artificially inflated the constant term. This document recounts how that conclusion was reached, illustrating the key findings with relevant figures.

Figure 1.101 shows a comparison between PS-HCAL data and the GS-HCAL simulation. PS-HCAL displayed a constant term of around 3%, which is considered typical for a stable hadronic calorimeter system. In contrast, the GS-HCAL result suggested a substantially higher constant term, measured to be about 4.7% at the "truth" stage of simulation and approaching 6.5% after digitization. Because these two calorimeters share broadly similar cell-level geometries, a discrepancy of this magnitude raised immediate suspicions. Rather than implicating a defective design, the data hinted that certain subsets of hadronic showers were not being fully captured.

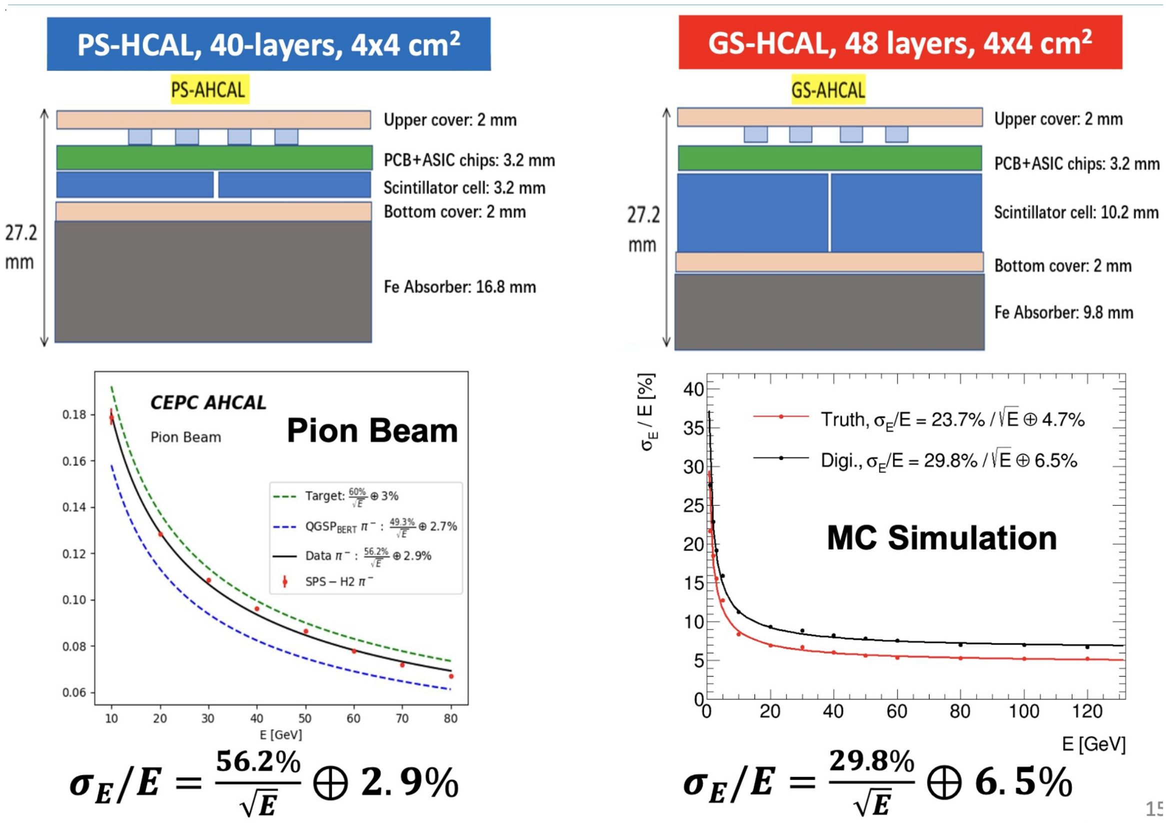

Figure 1.101: A comparison between PS-HCAL data (showing a constant term near 3%) and GS-HCAL simulation (indicating a notably higher constant term).

As soon as we recognized that the GS-HCAL geometry under consideration might not extend sufficiently far in depth, an alternative explanation emerged. In particular, for hadronic showers that start late or develop especially deeply, the shallower calorimeter configuration may allow substantial fractions of energy to escape, resulting in a tail of under-measured events.

To validate the hypothesis that longitudinal leakage was driving the discrepancy, the depth of the GS-HCAL was increased from 48 layers (around six interaction lengths) to 80 layers (roughly ten interaction lengths). Figure 1.102 presents the result of this adjustment. With 48 layers, the calorimeter produced a strong tail in the energy distribution at higher beam energies, leading to an extracted constant term of about 4.7%. When the calorimeter was extended to 80 layers, the tail significantly decreased, and the constant term dropped to about 2.9%. This improved value aligned well with the range typically seen in similar calorimeter systems.

The significant improvement observed with additional depth supported the idea that shower leakage, rather than any intrinsic design flaw, was responsible for the inflated constant term. By containing the showers more effectively, the depth-adjusted calorimeter demonstrated a performance characteristic of a well-functioning hadronic detector.

Although a deeper geometry provided a direct solution, it was also crucial to show that deliberately filtering out or restricting events likely to leak could restore a more typical constant term without physically changing the detector. Figure 1.103 illustrates two such selections applied to the shallower 48-layer configuration. One selection used only lower-energy

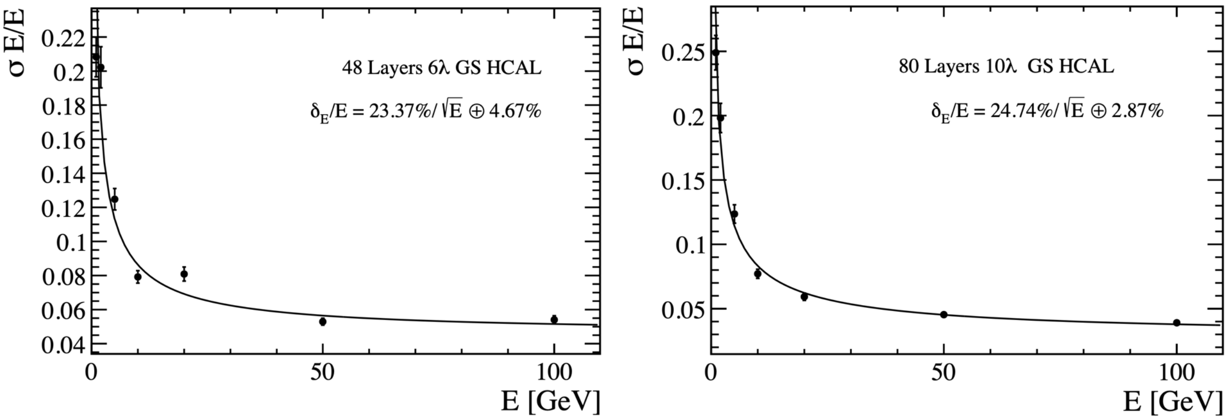

Figure 1.102: Comparison of two GS-HCAL configurations with different depths. A shallower setup (left) yields a pronounced high tail in the energy resolution and a large constant term. A deeper setup (right) effectively contains the showers, reducing the tail and lowering the constant term to a more typical value.

pions, which are less likely to penetrate the full depth and escape, and the other required that the hadronic shower initiate in the first few layers of the detector. Both methods led to a reduction in the fitted constant term, with values settling between roughly 2.9% and 3.4%. These numbers closely matched the performance expected for a detector of this design and ruled out the need to invoke more complex explanations. Once events that suffered from leakage were removed or minimized, the apparent large constant term essentially disappeared.

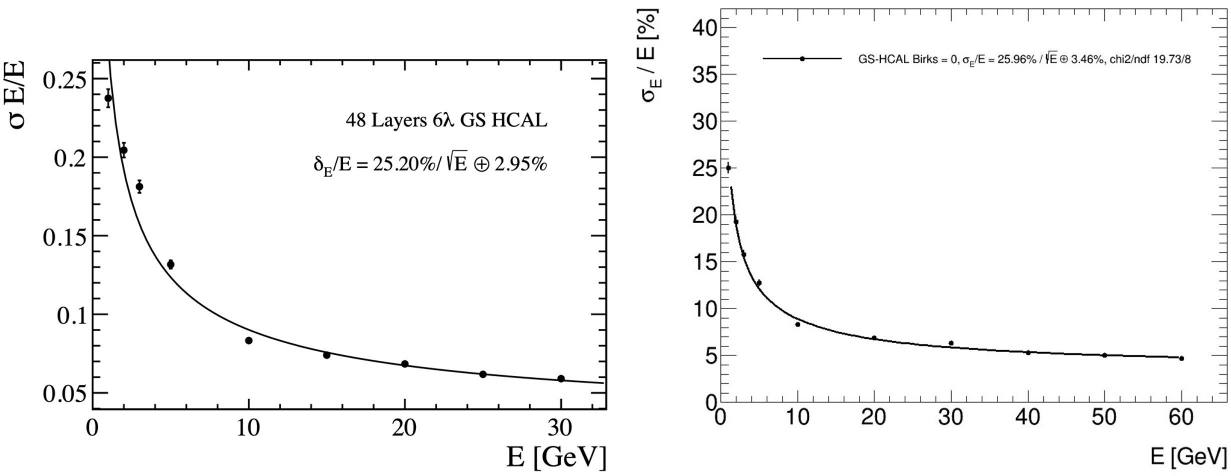

Figure 1.103: Reduction of the constant term in the shallower configuration through selective event removal. Focusing on lower beam energies (left) or ensuring the shower starts in the first few layers (right) mitigates leakage, lowering the constant term.

All evidence converged on the conclusion that a seemingly large constant term in GS-HCAL simulations was not the result of a flawed design or inconsistent calibration. Instead, an insufficient depth in certain configurations caused showers to leak out of the calorimeter, thereby creating a distortion in the energy distribution at high energies. The observation that deeper geometries or selective event removal yielded more reasonable values solidified the understanding that leakage was the source of the apparent discrepancy. By highlighting how sensitive hadronic calorimeters can be to depth and containment, this study underscores the importance of carefully matching the detector's longitudinal extent to the energy range of interest. Ultimately, once the issue of leakage was addressed, the GS-HCAL proved to have a constant term in line with standard calorimeter performance expectations, affirming its viability for high-energy physics applications.

1.9.2.2 BMR result of HCAL

The performance of physical events is evaluated with the PFA reconstruction together with the other sub-detector systems. The benchmark channel $H \to gg$ is used. Events are generated with Whizard and the detector responses are simulated with Geant 4 in the CEPCSW. These raw hits in the detector are reconstructed as tracks in the tracker and clusters in the calorimeter. Details about the offline software reconstruction are described in Chapter Software. By summing over all reconstructed objects, a Higgs boson mass resolution of 3.88% is achieved as in Figure 1.104. More specific performance studies, e.g. jet energy resolution with dependence on energy and angle are presented in Chapter Performance.

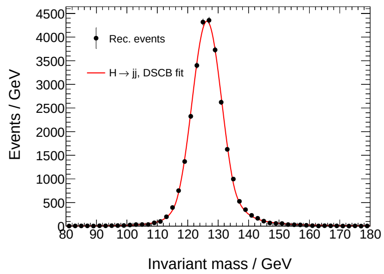

Figure 1.104: Reconstructed dijet invariant mass in $H \to gg$ process. The fitted Higgs mass is 126.32 ± 0.04 GeV, $\sigma(m_{jj}) = 4.90 \pm 0.04$ GeV.

1.9.3 Beam background simulation

The definition of the counting rate is the number of times a single glass cell fires within a certain period of time, while the occupancy is defined as the ratio of fired glass cells to the total number of glass cells within a specific time interval. During this time, each collision will generate pair production as well as background noise resulting from the loss of beam particles.

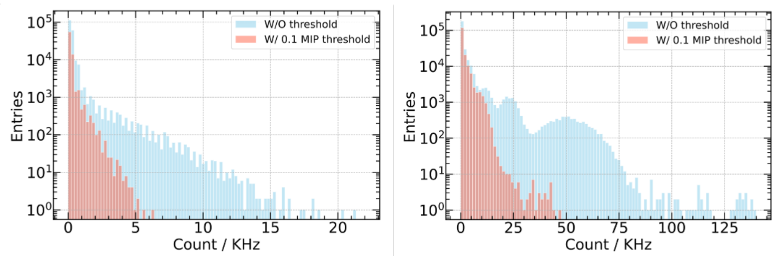

Figure 1.105: Count rate of HCAL within beam-induced background in Higgs mode. Left is barrel and right is endcap.

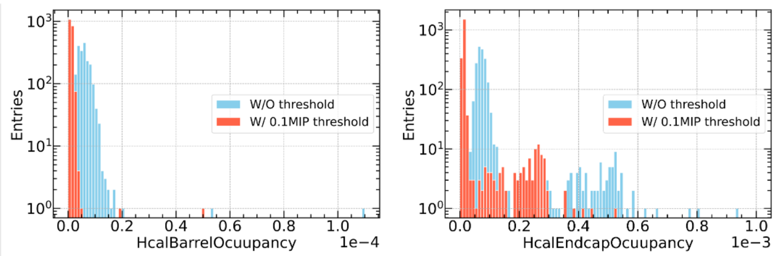

Figure 1.106: Occupancy of HCAL within beam-induced background in Higgs mode. Left is barrel and right is endcap.

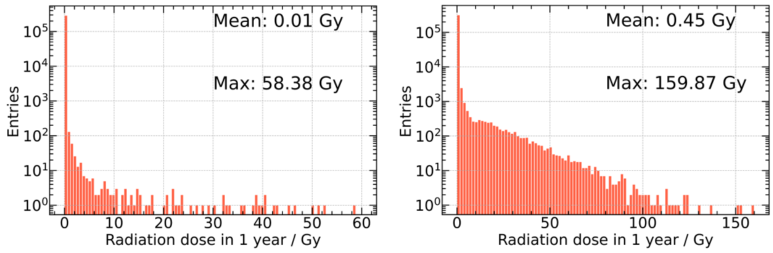

Figure 1.107: Total ionizing dose(TID) of HCAL within beam-induced background in Higgs mode. Left is barrel and right is endcap.

The definition of the Total ionizing dose(TID) is accumulated energy divided by mass for each cell. (assuming 3600 hours in one year) TID will cause radiation damage in glass cells and light output degradation.

(The current simulation results need to be updated, and results under the z mode need to be included.)

1.10 Cost

According to the scheme and structure of HCAL shown in Figure 1.108, the HCAL cost is consist of following parts:

a) Glass scintillator, 5.30 millon cells.
b) SiPMs, aiming to 1 pcs SiPM per GS cell, also 5.3 millon pieces.
c) Electronics(FEE), ASIC chips based front-end, 1 ch/cell, 5.3 millon channels.
d) Mechanics, one Barrel and two Endcaps, including absorbers, active layers, supports, toolings, and cooliing pipes.
e) Assembly and installation.

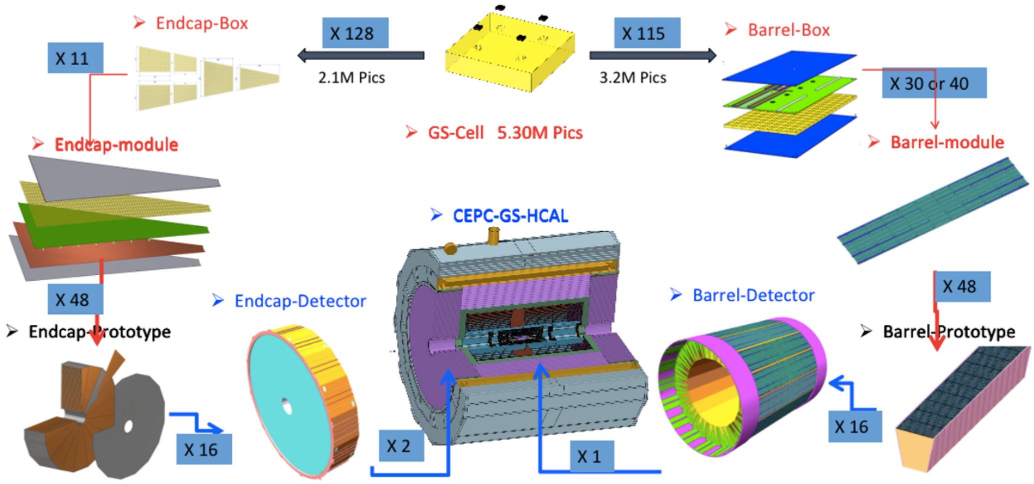

Figure 1.108: HCAL design

The core of HCAL is the GS Cell coupled with one SiPM (final goal). More than one hundred cells make up a Box and about 30 boxes form a layered Module, 48 layers in total. These 48-layer Modules then form a sector structure (Prototype) of the endcap or barrel. The whole barrel detector is built with 16 prototypes, so is one endcap detector. Finally, one barrel and two endcaps compose the whole hadron calorimeter. Therefore, the cost estimate of HCAL mainly depends on the total cost of 5.3 million Cell units. The quantity quoted is mainly divided into 100 slices for laboratory testing, 10,000 slices for model testing, and 5.3 million slices for hadron calorimeter. The core components, whether glass or SiPM, are not mature low-cost domestic products, so we need to research and develop together with domestic partners to achieve high-performance, low-cost alternative products.

Currently, each part of cost is estimated based on quotes offered by at lease three different suppliers. The total cost of HCAL is 68267 kCHF, some details listed in Table 1.15. It is full of confidence to achieve better performance glass scintillator, SiPM, at the same time, low price in the future.

Table 1.15: HCAL cost breakdown

System	Cost(kCHF)
Hadron calorimeter	68267
Gass scintillator	39750
SiPMs	6625
Electronics(FEE)	13515
Mechanics	6389
Assembly and installation(3%)	1988
Extra cost for back-end electronics	8550

1.11 Outlook

1.11.1 Glass Scintillator

1.11.1.1 Light yield and intrinsic light yield

Light yield/Light output The efficiency of converting particle deposition energy into photons; photons/MeV, requires the device to be able to distinguish a single photoelectron signal. The results are obtained by comparing a single photoelectron signal with a test sample to the full-energy peak.

Intrinsic light yield The light yield without any light loss inside the scintillator.

1.11.1.2 Birks constant

The energy loss of ions in scintillator can be transferred to scintillator molecules to produce luminescence, in addition, it may cause atomic displacement, charge transfer, and so on. There is a nonlinear relationship between energy loss and luminescence. The difference between different ions is large, especially at low energy. Thus, the relationship between excitation molecular density and non-radiative relaxation in scintillation materials is quantified by the Birks constant:

$$Q_{Birks}(\epsilon) \quad = \frac{1}{1+kB\times\epsilon} \tag{1.9}$$

where ϵ is the energy deposition of particles per unit length in the material, reflecting the energy loss. And Table 1.16 shows the Birks factor of different scintillators.

We will conduct experiments on glass scintillator and BGO crystal arrays in Lanzhou heavy ion accelerator, as shown in Figure 1.109. The data set is obtained by measuring the average light yield under different incident kinetic energy. According to the luminescence per unit distance, the quenching factor Q with energy loss curve will be calculated. Different quenching functions will be selected to fit Q curves, the reliability of the model will be calculated, and finally the Birks constant will be obtained.

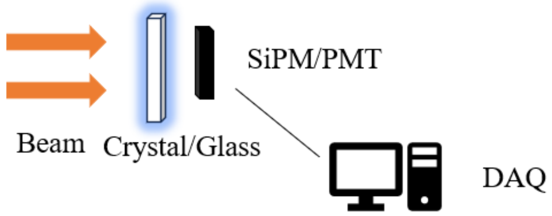

Figure 1.109: Test scheme of Birks constant.

Table 1.16: Birks constant of scintillator

Scintillator	Density (g/ml, g/cm^3)	kB ($\times 10^{-3}$gMeV^{-1}cm^{-2})
Polystyrene (C_8H_8)	1.06	9
PXE($C_{16}H_{16}$) Liquid scintillator	0.7734	6.8
Pseudoxylene (C_9H_{12})	0.857	9.4, 42 (Proton)
$CdWO_4$	7.9	5.3, 5.1 (For F ions)
CaF_2(Eu)	3.18	10.5
$ZnWO_4$	7.41	9.0
$CaWO_4$	6.062	6.2, 8 (For O ions), 9.8 (SP for electron-only parts)
CsI(TI)	4.53	3.2 (Cs and I ions), 2.3 (α particle)
CsI(Na)	4.51	5.5
NaI(TI)	3.67	3.8 (Initial value), 6.5 (Low energy), 1.25 (α particle)
CeF_3	6.16	11.1
BGO	7.13	8 (CEPC simulation)

1.11.1.3 Scintillation performance changes under magnetic field

When the light source is placed in a sufficiently strong magnetic field, most of the monochromatic light emitted by the source will split into several polarized spectral lines, and the number of splits varies with the type of energy level. And paramagnetic metal ions are subjected to external magnetic field, the transition radiation of energy level E1-E2 generates Zeeman splitting, which leads to energy level splitting, thus splitting the emission spectrum and changing the intensity. There is a magnetic field with a certain magnetic induction intensity during CEPC operation (3T), which will generate a a large stress on the glass, so it is necessary to study the performance changes of glass under the magnetic field.

As shown in Figure 1.110, we tested the changes in the scintillation performance of the glass scintillation by placing it in different directions in a magnetic field under ^{137}Cs γ-ray, with BGO, LYSO and GAGG crystals as a reference. Meanwhile, we will test the Zeeman effect of the glasses under the magnetic field to analyze the change of its scintillation performance.

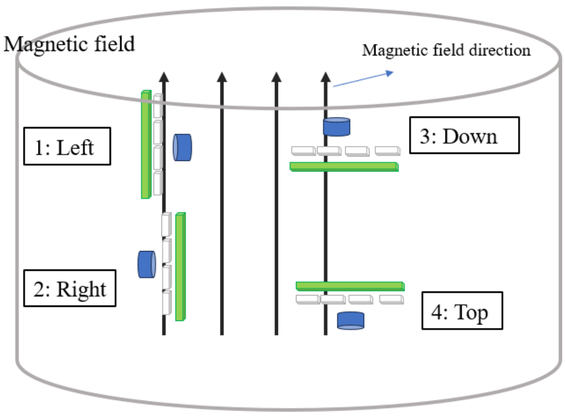

Figure 1.110: Test scheme of scintillation performance under magnetic field.

1.11.1.4 MIP response of GFO glass scintillator

The MIP response of the glass scintillator needs to be re-calibrated due to the improvement in light yield. Therefore, we selected a piece of glass with a light yield of 1807 ph/MeV to test its MIP response, with a plastic scintillator placed on the upper and lower ends as a trigger. Figure 1.111(a) displays the energy spectrum of the glass under cosmic ray, the

MIP response is 397.5 P.E./MIP after subtracting the pedestal. To verify the accuracy of the test results, Gamma energy spectrum was measured with the same experimental setup, as shown in Figure 1.111(b). Under ^{137}Cs, the light output of the glass is 64.4 P.E./MeV. According to previous simulation result, 1 MIP is about 7 MeV/cm, and the measured value of MIP response is relatively small. Compared to previous results, the poor MIP response may be due to the low light yield, low photon collection efficiency and poor light attenuation length.

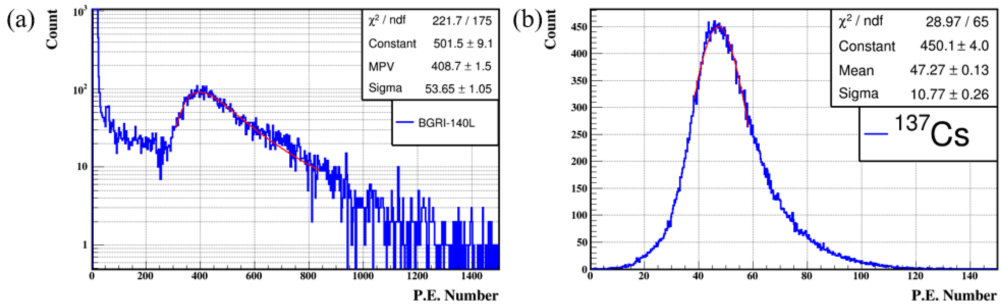

Figure 1.111: Energy spectrum of the glass under (a) cosmic ray and (b) Gamma ray.

1.11.2 Prototype

We present herein a description of the simulation, design and test plan of the 0.6 m^3 glass scintillator analog hadron calorimeter (GS-AHCAL) prototype that consists of a steel scintillator sandwich structure. The scintillator planes are segmented into square tiles that are individually read out by SiPMs. The steel plates are 52 cm $\times$ 52 cm wide and on average 9.8 mm thick. We use standard S304 steel that is a composite of iron, carbon, manganese, nickel, phosphorus and sulphur.The main technical goal is to test the performance and reliability of glass scintillators on a large scale, since this detector uses thousands of glass scintillator tiles (8112) in a test beam. Our physics goals are the study of hadron shower shapes, reproduction of observed shower shapes in simulations, and studies of particle flow algorithms(PFA) . We have two main goals for the glass scintillator HCAL technical prototype. First, we want to test the novel glass scintillator on a large scale, identify critical operational issues, develop quality control procedures and establish reliable calibration concepts that include test bench data. Second, we want to accumulate large data samples of hadronic showers of GS-AHCAL in test beams. These samples are needed to investigate hadronic shower shapes and to test simulation models, since it is not possible to extract this information from existing calorimeter data. The test beam data samples are also very useful for studying and tuning particle flow algorithms (PFA) with real events.

1.11.2.1 Simulation of GS-HCAL prototype

The standalone simulations of GS-AHCAL prototype have been done. The simulation was performed to check the energy coverage of 80 GeV proton module size: 3.24 × 3.24 m^2 (81×81 tiles), 80 layers pion shower profile. The simulation result shows that the most energy deposition is mainly along the center of the proton beam. Even with 48 sampling layers, an 80 GeV pion beam will still experience energy leakage in the longitudinal direction.

Figure 1.112 presents the comparison of energy coverage versus total cell number.After a cross-section of 13 x 13 cells, the difference in leakage energy is not significant, however, the number of detector cells increases rapidly, and a 95% energy coverage is an acceptable rate. Considering both price and performance, the size with 13 cells × 13 cells × 48 layers was chosen as the prototype size. Figure1.112 shows deposited energy of 80 GeV proton versus prototype size. The deposition energy of the 13×13×48 prototype size is already close to the level of full energy deposition.

Due to the relatively small size of the prototype, energy leakage is unavoidable, leading to a reduction in energy resolution compared to the full-sized AHCAL. Figure 1.113 illustrates the energy resolution curve and linearity of the prototype with proton beam.

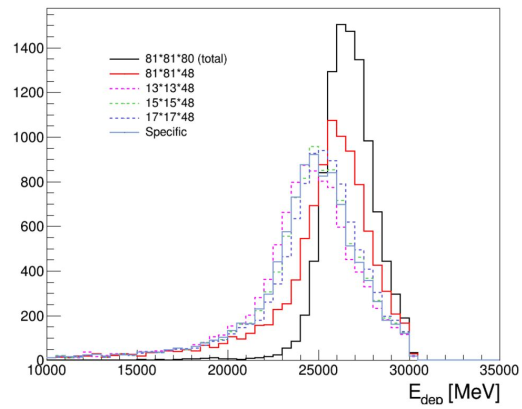

Figure 1.112: Deposited energy of 80 GeV pion VS prototype size

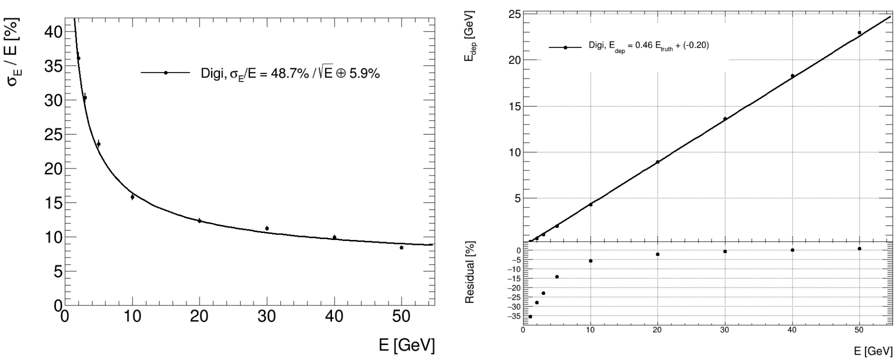

Figure 1.113: Energy resolution and linear simulation result of GS AHCAL prototype

1.11.2.2 Design and construction plan of GS-HCAL-Prototype

A AHCAL prototype based on glass scintillator cells will be established, with a total of 13 × 13 × 48 = 8112 cells. The glass scintillator cell size is 4 cm × 4 cm × 1 cm, it will be readout by four SiPMs (3 × 3 mm^2). The cross-sectional size is 52 × 52 cm^2, with 48 layers, and the overall thickness is approximately 130.6cm. Figure 1.114 shows the coupling between glass scintillator and SiPM. One glass scintillator couple with 1 SiPM for readout. Figure 1.115 shows one layer of glass scintillator AHCAL prototype with 169 cells. And glass scintillator will be adhered to the PCB board, one SiPMs and one LED will also be soldered onto a small PCB board, then this small PCB board will be soldered with one layer PCB board. The PCB and glass scintillator will be enclosed by upper and lower cover stainless steel plates, ultimately forming a cassette that facilitates installation and protects the electronic chip and the glass scintillator. Figure 1.115 shows the preliminary mechanical design of the prototype with 13 × 13 cells and 48 layers, the total cells number is 8112.This prototype is composed of 48 sensitive layers and 48 stainless steel absorber layers, alternating between each other.The entire prototype will be secured onto a stainless steel outer frame, which is equipped with slots. Both the active layer and the absorber will be fixed to the frame through these slots. This design makes the adjustment of the detector extremely flexible. When improvements are needed for the active layer, it can be easily removed with simplicity and convenience. The gap width between plates is adjustable. The width of the gap between the plates is adjustable. For a vertical beam direction, there is a 2-millimeter tolerance to account for the unevenness of the steel plates and to allow for smooth insertion of the cassette assembly. The light from the glass scintillator tiles will be read by SiPM photodetectors. These photodetectors, used in several systems including GECAM and JUNO-TAO, provide a very high gain (greater than 1E5) and an excellent photodetection efficiency (higher than 30%).32448 NDL-SiPMs will be used in this Prototype for its good cost performance.

1.11.2.2.1 GS AHCAL prototype calibration A set of blue light LED will be used to calibrate SiPM and electronics. At the SiPM working point, several SiPM characteristics will be measured. With low-light intensities of the LED, pulse

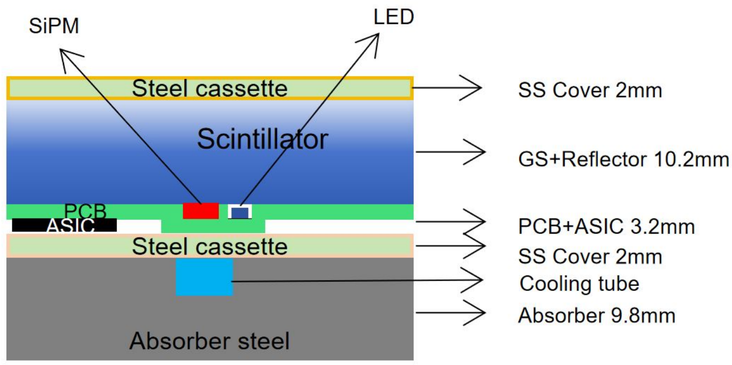

Figure 1.114: The coupling between glass scintillator and SiPMs, the layer structure of GS-AHCAL prototype

height spectra that are used for the gain calibration will be recorded. The excellent resolution is extremely important for calorimetric applications, since it provides self-calibration and monitoring of each channel. the response function of each SiPM over the entire dynamic range (zero to saturation) will be recorded.

1.11.2.2.2 GS AHCAL prototype ASIC For the ASIC chips, a new version of ASIC chips will be developed by CEPC electronics group for both ECAL and HCAL.The prototype will use this type ASIC, it is named ChoMin. The 36 channel ASIC chip will develped and the power is 15 mW/channel. This low power consuming can reduce the cooling requirements of GS-AHCAL prototype.

1.11.2.2.3 Reflective film of glass scintillator We conducted comparative evaluations of ESR films, titanium oxide coatings, and Teflon films as reflective coatings for glass scintillator, with experimental results indicating that both titanium oxide coatings and Teflon films demonstrated superior reflectivity performance on the glass scintillator. The reflection performance of ESR reflective films for glass scintillator is relatively inferior.

1.11.2.2.4 GS AHCAL prototype cooling To validate the final cooling solution for the GS-AHCAL, we will utilize cooling water to cool the detector in the prototype, thereby mastering the technical aspects of the full GS-AHCAL cooling system. We will equip the prototype with a compact industrial water chiller connected to the prototype's cooling water pipes, achieving cooling of the prototype detector through precise regulation of the cooling water's flow rate and temperature.The black pipes shown in Figure 1.115 constitute the cooling water piping system of the prototype.

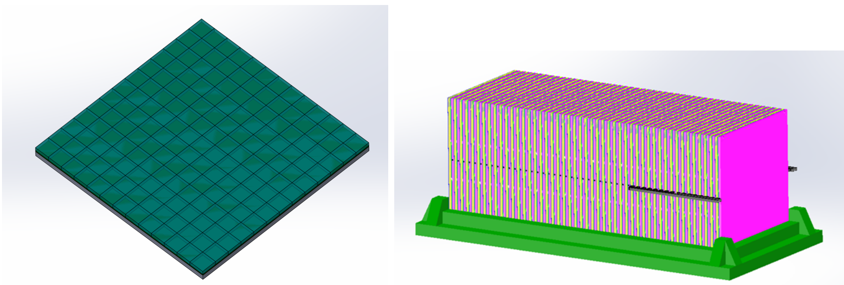

Figure 1.115: one layer and whole size of GS-AHCAL prototype

1.11.3 Beam Test consideration

A mini-prototype with 3 cells × 3 cells × 7 layers will be completed in 2025. The beam test of this mini-prototype is scheduled to take place at CERN in October 2025. From the plan, the big prototype will be completed at the end of 2026, and it is planned to conduct cosmic ray test and beam test in 2027. The cosmic ray experiment will be conducted at IHEP in China. CERN will be the optimal location for beam test, as it can provide muon beams, pion beams, and electron beams with energies ranging from 2 GeV to 180 GeV. If the beam at CERN stops operating in 2027, we have a few other options. One is China's CSNS, which can provide a 1.6 GeV proton beam, or we could consider the proton beam at the University of Tokyo in Japan.

We will construct a platform for beam testing that can move ±25 cm in both vertical and horizontal directions with a precision better than 1 mm, rotate ±30 degrees, and has a load-bearing capacity exceeding 5 tons. It will also be equipped with a remote controller. During the beam testing, the prototype will be placed on this platform, making it extremely convenient to change the hit position of the beam on the prototype.

References

[1] J.-C. Brient. "Improving the jet reconstruction with the particle flow method: An introduction". In: Calorimetry in particle physics. Proceedings, 11th International Conference, CALOR 2004, Perugia, Italy. 2004.

[2] M.A. Thomson. "Particle flow calorimetry and the PandoraPFA algorithm". In: *NIMA* 611 (2009), pp. 25–40. DOI: 10.1066/j.nima.2009.09.009.

[3] Manqi Ruan and Henri Videau. "Arbor, a new approach of the Particle Flow Algorithm". In: *International Conference on Calorimetry for the High Energy Frontier*. 2013, pp. 316–324. arXiv: 1403.4784 [physics.ins-det].

[4] CALICE Wikipage. URL: https://twiki.cern.ch/twiki/bin/view/CALICE/.

[5] G. Baulieu et al. "Construction and commissioning of a technological prototype of a high-granularity semi-digital hadronic calorimeter". In: *JINST* 10.10 (2015), P10039. DOI: 10.1088/1748-0221/10/10/P10039. arXiv: 1506.05316 [physics.ins-det].

[6] D. Boumediene et al. "Energy reconstruction of hadronic showers at the CERN PS and SPS using the Semi-Digital Hadronic Calorimeter". In: *JINST* 17.07 (2022), P07017. DOI: 10.1088/1748-0221/17/07/P07017. arXiv: 2202.09684 [physics.ins-det].

[7] Yukun Shi et al. "Design and optimization of the CEPC scintillator hadronic calorimeter". In: *Journal of Instrumentation* 17.11 (2022), P11034. DOI: 10.1088/1748-0221/17/11/P11034. URL: https://dx.doi.org/10.1088/1748-0221/17/11/P11034.

[8] Manqi Ruan. *Performance requirement from the hadronic event/jet*. https://agenda.linearcollider.org/event/8217/contributions/44771/attachments/34967/54047/Jet_Requirement-LCWS.pdf. 2019.

[9] Mingyi Dong et al. "CEPC Conceptual Design Report: Volume 2 - Physics & Detector". In: (Nov. 2018). Ed. by João Barreiro Guimarães da Costa et al. arXiv: 1811.10545 [hep-ex].

[10] Manqi Ruan. *Arbor, a new approach of the Particle Flow Algorithm*. 2014. arXiv: 1403.4784 [physics.ins-det]. URL: https://arxiv.org/abs/1403.4784.

[11] Frederic Dulucq et al. "HARDROC: Readout chip for CALICE/EUDET Digital Hadronic Calorimeter". In: *IEEE Nuclear Science Symposium & Medical Imaging Conference*. 2010, pp. 1678–1683. DOI: 10.1109/NSSMIC.2010.5874060.

[12] The CALICE collaboration. "First results of the CALICE SDHCAL technological prototype". In: *Journal of Instrumentation* 11.04 (2016), P04001. DOI: 10.1088/1748-0221/11/04/P04001. URL: https://dx.doi.org/10.1088/1748-0221/11/04/P04001.

[13] The CALICE collaboration. "First results of the CALICE SDHCAL technological prototype". In: *Journal of Instrumentation* 11.04 (2016), P04001. DOI: 10.1088/1748-0221/11/04/P04001.

[14] Jianbei Liu et al. "CALICE scintillator-SiPM calorimeter prototypes: R&D highlights and beamtests". In: *Nucl. Instrum. Methods Phys. Res. A* 1072 (2025), p. 170191. ISSN: 0168-9002. DOI: https://doi.org/10.1016/j.nima.2024.170191.

[15] U. Buchner et al. "PERFORMANCE OF A SCINTILLATING GLASS CALORIMETER FOR ELECTROMAGNETIC SHOWERS". In: *Nucl. Instrum. Methods Phys. Res. A* 272 (1988), pp. 695–706.

[16] E. Auffray et al. "Cerium doped heavy metal fluoride glasses, a possible alternative for electromagnetic calorimetry". In: *Nucl. Instrum. Methods Phys. Res. A* 380 (1996), pp. 524–536.

[17] S. Navas et al. "Review of particle physics". In: *Phys. Rev. D* 110.3 (2024), p. 030001. DOI: 10.1103/PhysRevD.110.030001.

[18] P. Hu et al. "Preliminary optimization study on the PFA-based GSHCAL for the CEPC". In: *Journal of Instrumentation* 19.06 (2024), T06008. DOI: 10.1088/1748-0221/19/06/T06008.

[19] J. B. Birks. "Scintillations from Organic Crystals: Specific Fluorescence and Relative Response to Different Radiations". In: *Proc. Phys. Soc. A* 64 (1951), pp. 874–877. DOI: 10.1088/0370-1298/64/10/303.

[20] V. Dormenev et al. "Multipurpose Ce-doped Ba-Gd silica glass scintillator for radiation measurements". In: *Nucl. Instrum. Methods Phys. Res. A* 1015 (2021), p. 165762.

[21] A. Phunpueok et al. "Comparison of Scintillation Light Yield of CWO and BGO Single Crystals for Gamma Ray Detection". In: *Applied Mechanics and Materials* 901 (2019), pp. 89–94.

[22] X.Y. Sun et al. "Tunable valence state and scintillation performance of dense Ce^{3+}-doped borosilicate glasses prepared in ambient atmosphere". In: *J. Mater. Chem. C* 12 (2024), p. 11149.

[23] Z.H. Hua et al. "Light attenuation and loss in Ce^{3+}-doped dense glass scintillator". In: *Nucl. Instrum. Methods Phys. Res. A* 1072 (2025), p. 170182.

[24] Yingyi Liu et al. "Physical design of the APEP beam line at CSNS". In: *Nuclear Instruments and Methods in Physics Research Section A: Accelerators, Spectrometers, Detectors and Associated Equipment* 1042 (2022), p. 167431. ISSN: 0168-9002. DOI: https://doi.org/10.1016/j.nima.2022.167431.

[25] Z.H. Hua et al. "An evaluation method for nuclear radiation detection performance of glass scintillator". In: *Radiat Detect Technol Methods* 8 (2024), pp. 1107–1119.

[26] D.J. Du et al. "Muon beamtest results of high-density glass scintillator tiles". In: *JINST* 19 (2024), P05039.